Imperial College London
Department of Materials

Biosensing with Microwave Debye Relaxation Analysis

Toby H. Basey-Fisher

2013

Submitted in part fulfilment of the requirements for the degree of
Doctor of Philosophy in Materials of Imperial College

Declaration of originality

I hereby declare that the material presented in this thesis is entirely the result of my own independent research except where otherwise acknowledged. All published or unpublished material used in this thesis has been given full acknowledgement.

The copyright of this thesis rests with the author and is made available under a Creative Commons Attribution Non-Commercial No Derivatives licence. Researchers are free to copy, distribute or transmit the thesis on the condition that they attribute it, that they do not use it for commercial purposes and that they do not alter, transform or build upon it. For any reuse or redistribution, researchers must make clear to others the licence terms of this work.

T. H. Basey-Fisher

April 2013

Acknowledgements

I would like to begin by thanking my supervisors Prof. Norbert Klein and Prof. Stefan Maier for the opportunity and freedom they have given me to conduct my research and believing in my ability to direct my own work. I would especially like to thank Norbert for imparting so much of his vast knowledge not only concerning microwave devices but on all scientific matters and for maintaining an open-minded approach to the interdisciplinary research undertaken.

My gratitude goes out to Dr. Stephen Hanham who has endured endless discussions on almost every conceivable topic concerning microwaves. Also for his assistance in developing a number of codes to conduct and analyse measurements and for proof-reading all of my written work.

Many thanks go to Dr. Nadia Guerra and Dr. Chiara Triulzi for the time, patience and effort they have put into the collaborative project reported in Chapters 5 and 6 and for supplying important biological media without which none of my experiments would have materialised.

I would like to acknowledge Prof. Molly Stevens for her valuable appraisal of ideas and research as well as for the laboratory space that was necessary for

much of the research conducted.

Prof. Neil Alford has also provided continuous and objective views on the research reported within this thesis in addition to pushing for the application of this research beyond the scope of this thesis.

My thanks also go to Dr. Olena Shaforost for sharing her wealth of knowledge on performing resonant measurements, Konrad Domanski for his tireless work in the laboratory and whose contributions are apparent in Chapter 4 and to my other students Ji, Shoujie and Sonja who have contributed in many other ways.

Thank you to my colleagues and friends who have been able to make work that little bit more enjoyable most notably Stefan, Olly and Matt.

A special thanks to my parents Ann and Stephen, brothers Alex and Oliver and sister Alice who have not only offered continual support but who have also served as an inspiration. I would also like to thank my grandmother Joan for giving me creative control of her house throughout my childhood that helped to instil my love of drawing, design and invention.

Lastly my thoughts are with Laura for her unending support of my work, for giving me the passion and motivation to create and for never letting life get boring.

Abstract

The microwave dielectric response of biological solutions and electrolytes has been investigated for a number of decades though applications that utilise the response are few and far between. The dielectric features of many biological fluids are unique across the microwave spectrum and offer a wealth of possibilities for analysis techniques. This thesis documents the development of broadband and resonant microwave techniques that are suitable for applications in biological fluid analysis.

Theoretical models concerning the dielectric properties and electromagnetic interaction with polar liquids such as water are examined. The means to conduct experimental observations of the dielectric spectrum of liquids are reviewed and the ability to conduct measurement on small sample volumes discussed.

Broadband spectroscopy from 0.2 to 20 GHz has been performed on the simplest constituent of a biological fluid, water, and compared to literature and theoretical models. Other polar liquids such as ethanol, propanol and methanol were also examined.

The impact of ions in solution on the high frequency permittivity was studied,

in particular the response of alkali metal chlorides, copper sulphate and zinc sulphide. The temperature dependence of the metal chlorides was found to be highly dependent on the effective hydration radius and subsequently a means of calculating the temperature-dependent hydration radius of lithium and sodium was developed. The respective radii at room temperature were found to be 340±39 pm and 215±21 pm. Relaxation processes from ion-association were examined and confirmed to be present in ions with high charge density.

Comparative studies between various biological solutes in aqueous environments demonstrated that many proteins possess unique microwave dielectric spectral features based on bound water and protein-water exchange mechanisms. Two techniques for the differentiation of protein solutions are outlined based on the microwave dielectric spectrum and the relaxation processes associated with protein water.

Broadband measurements were conducted from 0.5 to 40 GHz to analyse the dielectric response of whole blood and serum from human and murine donors. Based on the dielectric comparison of serum and whole blood a method for the determination of haemoglobin concentration is presented. A 9.4 GHz dielectric resonator was developed with an integrated microfluidic chip for the determination of haemoglobin concentration in samples as small as 2 microlitres. This was subsequently utilised to monitor the progression of haemoglobin levels in $APC^{min/+}$ mice with colon cancer. The results demonstrate the first microwave device with proven haematological diagnostic value with an accuracy that is equivalent to or better than existing commercial techniques (comparative standard deviation 0.85 g/dL to Sysmex system - commercial comparison >1.5 g/dL) and is non-destructive.

List of Publications

Journal Publications from this Thesis

[1] T. H. Basey-Fisher, S. M. Hanham, H. Andresen, S. A. Maier, M. M. Stevens, N. M. Alford, N. Klein, Microwave Debye relaxation analysis of dissolved proteins: Towards free-solution biosensing. Applied physics letters 99, 233703 (2011).

[2] T. H. Basey-Fisher, S. M. Hanham, S. B. Merelli, S. A. Maier, N. Klein, Aqueous protein solution differentiation with high frequency microwave Debye relaxation analysis. IEEE Biowireless, 2013

[3] T. H. Basey-Fisher, K. Domanski, N. Klein Microwave conductivity temperature dependence of alkali metal chlorides. Submitted to Journal of Chemical Physics, 2013

[4] T. H. Basey-Fisher, N. Guerra, C. Triulzi, A. Gregory, S. M. Hanham, M. M. Stevens, S. A. Maier, N. Klein, Microwaving blood as a non-destructive technique for haemoglobin measurements on microlitre blood. Submitted to Adv. Heathcare Mat., 2013

[5] J. Gilchrist, T. H. Basey-Fisher, S. Heutz, D. W. McComb, Analysis of Donor-acceptor Interfaces within Organic Solar Cells Using Transmission Electron Microscopy. To be submitted

[6] A. Axelsson, M. Terginkangas, T. H. Basey-Fisher, H. Jahntunen, N. Alford, High

frequency dielectric properties of ceramic-polymer composites. Submitted to Applied Polymer Science

Conference Presentations from this Thesis

[1] T. H. Basey-Fisher, S. Gu, S. Hanham, N. Klein, A Debye Relaxation Analysis of Biomolecular Solutions by Microwave Spectroscopy, Dielectrics, Canterbury 2011 (poster)

[2] T. H. Basey-Fisher, Biosensing: A Microwave Debye Relaxation Approach, Prague 2012 (oral)

[3] T. H. Basey-Fisher, Microwave biosensing through Debye relaxation analysis, Biosensors and bioelectronics 2012, Cancun 2012 (oral)

[4] T. H. Basey-Fisher, Microwave biosensing with Debye relaxation analysis, EMMA, Paris 2012 (oral)

[5] T. H. Basey-Fisher, Microwave to Terahertz properties of proteins and cells, THz centre inaugural conference, London 2012 (oral)

[6] J. Gilchrist, T. H. Basey-Fisher, Analysis of Donor-acceptor Interfaces within Organic Solar Cells Using Transmission Electron Microscopy, MRS, San Francisco (oral)

List of abbreviations

EM	Electromagnetic
VNA	Vector network analyser
TDS	Time-domain spectrometer
CW	Continuous wave
TE	Transverse electric wave (electric field perpendicular to direction of propagation)
TM	Transverse magnetic wave (magnetic field perpendicular to direction of propagation)
EH	Hybrid with dominating electric field
TEM	Transverse electromagnetic (electric and magnetic field perpendicular to direction of propagation)
Q	Quality factor of a resonance
$\Delta(1/Q)$	The change in the inverse quality factor of a resonance
Δf	The change in the resonant frequency of a resonance
BSA	Bovine serum albumin
Hgb	Haemoglobin
RBC	Red blood cell
HCT	Haematocrit (red blood cell count)
APC	Adenomatous polyposis coli
$\text{APC}^{min/+}$	Mutated adenomatous polyposis coli gene
RF	Radio frequency
POC	Point of care

List of variables and constants

ϵ_0	8.854×10^{-12}	Fm^{-1}	Permittivity of free space
ϵ	-	Fm^{-1}	Permittivity
ϵ_r	-	-	Relative permittivity
ϵ'	-	-	Real permittivity (relative)
ϵ''	-	-	Imaginary permittivity (relative)
μ_0	1.2566×10^{-6}	Hm^{-1}	Permeability of free space
μ	-	Hm^{-1}	Relative permeability
σ	-	Sm^{-1}	Conductivity
i	-	-	Complex operator
f	-	s^{-1}	Frequency
ω	-	s^{-1}	Angular frequency
λ	-	m	Wavelength
k	-	m^{-1}	Wavevector
δ	-	s or m	Phase difference
c	2.998×10^{8}	ms^{-1}	The speed of light in a vacuum
$\mathbf{F}$	-	N	Force
$\mathbf{E}$	-	NC^{-1}	Electric field
$\mathbf{D}$	-	Cm^{-2}	Electric displacement field
$\mathbf{B}$	-	T	Magnetic flux density
$\mathbf{H}$	-	$\mathrm{A\ m}^{-1}$	Magnetic field strength
$\mathbf{P}$	-	Cm^{-2}	Polarisation
$\mathbf{p}$	-	Cm	Electric dipole moment
q	-	C	Electric charge
ρ	-	Cm^{-1} / Cm^{-2} / Cm^{-3}	Charge density
$\mathbf{J}$	-	Am^{-2}	Current vector
Z	-	S^{-1}	Impedance
k_B	1.3806×10^{-23}	JK^{-1}	Boltzmann constant
Q	-	-	Quality factor

Contents

Acknowledgements **iii**

Abstract **iv**

List of Publications **vii**

Journal Publications vii

Conference Presentations viii

List of Abbreviations **ix**

List of Variables and Constants **x**

1 Introduction **1**

1.0.1 Motivation 3

1.0.2 Thesis outline 3

2 Electromagnetic theory of liquids 6

2.1 Polarisation 6

2.1.1 Induced dipoles and the Clausius-Mossotti equation . . 9

2.1.2 Reorientational polarisation 12

2.2 Propagating electromagnetic waves in dielectrics 18

2.2.1 Maxwell's equations 18

2.2.2 Wave equations 19

2.2.3 Phase 22

2.2.4 Losses 23

2.2.5 Conductivity 24

2.2.6 The Debye model 24

2.3 Extended relaxation models 28

2.3.1 Cole-Cole diagrams 30

2.3.2 Permittivity and relaxation temperature dependence . 31

2.3.3 Electrolyte conductivity 32

2.4 Summary 34

3 Microwave dielectric measurement techniques 35

3.1 Waves at interfaces 35

3.2 Vector Network Analyser 37

3.3 Coaxial measurements 40

3.3.1 Modelling, calibration, errors and permittivity calculations 42

3.4 Resonators 47

3.4.1 Dielectric resonators 50

3.4.2 Manufacture 51

3.4.3 Resonant modes 52

3.4.4 Quality factor 56

3.4.5 Evanescent fields 57

3.4.6 Dielectric measurement and perturbation theory 58

3.4.7 Coupling 61

3.4.8 Loaded Q 63

3.5 Time domain spectrometers 64

3.6 Summary 65

4 Dielectric properties of polar solutions and electrolytes 66

4.1 Polar liquids 66

4.1.1 Data fitting 70

4.1.2 Analysis of polar liquids 71

4.2 Electrolytes 75

4.2.1 Conductivity 76

4.2.2 Ion-association 83

4.3 Summary 87

5 Dielectric properties of biological solution 89

5.1 Biological solutions 89

5.1.1 Mixed media 90

5.1.2 Proteins and bound water 91

5.1.3 Protein solution differentiation by microwave Debye relaxation analysis 99

5.2 Dielectric response of cell solutions 112

5.2.1 Looyenga polarisation 112

5.2.2 High frequency dielectric response of blood 115

5.3 Summary 120

6 Blood analysis with a microwave dielectric resonator 121

6.1 Haemoglobin 121

6.1.1 Anaemia 123

6.2 Microwave dielectric resonator 125

6.2.1 Microfluidic integration 128

6.2.2 Serum separation 129

6.3 Haemoglobin, serum protein and electrolyte measurements . . 132

6.4 APC murine measurements 137

6.4.1 Apc mice 139

6.5 Summary 142

7 Conclusion **143**

7.1 Thesis review 143

7.2 Main findings 144

7.2.1 Electrolyte differentiation and hydration shells 144

7.2.2 Protein solution analysis 145

7.2.3 Hgb measurements 146

7.3 Outlook 147

Bibliography **148**

Chapter 1

Introduction

Electromagnetic interaction with matter is a crucial and dominating feature of our everyday lives. Our knowledge of phenomena between the two is well documented, from the fundamental macroscopic interactions defined by Maxwell's equations [1] to the microscopic details of quantum electrodynamics. Such understanding presents the opportunity to conduct detailed analysis on materials such as composition and atomic structuring [2]. Acquisition of this data has had a large impact on many avenues of science from natural photonics [3] to pharmaceuticals [4].

Electromagnetic sensing techniques have evolved rapidly over the past century and have produced various applications across a broad frequency regime, such as low-frequency radar detection and terahertz body scanning [5] up to X-ray diffraction in defining crystalline structure [6]. Many electromagnetic interactions with matter such as surface plasmons and molecular magnetic resonances have provided the means for biological analysis on a macroscopic (magnetic resonant imaging of the body) to microscopic (surface plasmon protein detection) range for medical purposes. This rapidly growing interdisciplinary research, driven by the desire for cheap, rapid and accurate diagnostic abilities has become a prominent scientific field labelled biosensing [7, 8]. Electromagnetic techniques have primarily focused on optical and infrared analysis with radio frequency (RF), microwave and terahertz frequencies remaining somewhat under-explored (Fig. 1.1).

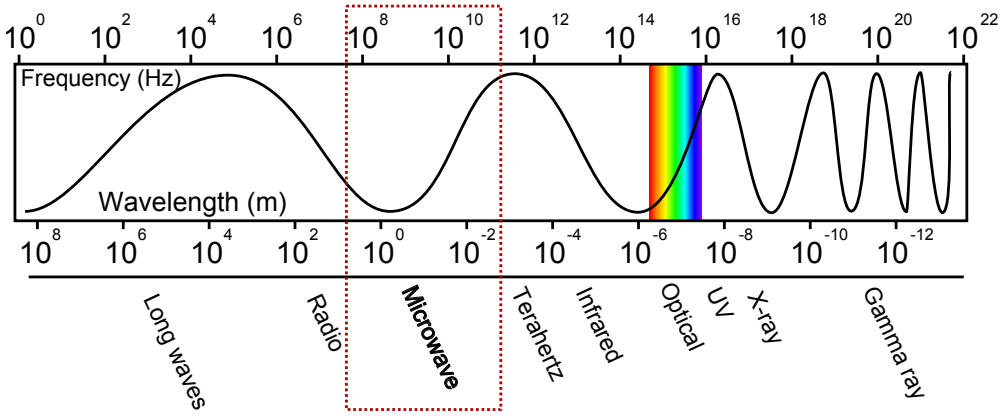


Figure 1.1: The electromagnetic spectrum from single to zetta Hz. The optical range is highlighted by the colours of the optical spectrum. The electromagnetic spectrum utilised within this thesis is outlines by a red box.

Microwave and RF devices are typically associated with revolutionising how communication occurs throughout the world. Despite Maxwell theorising the existence of electromagnetic waves in 1873 [1] it wasn't until Nikola Tesla proposed that radio waves may be capable of information transfer in 1892 that wireless radio communication appeared [9]. The advantages of microwave communication were made apparent as soon as 1895 when Guglielmo Marconi (Nobel Prize Laureate 1909) demonstrated signal transmission to a location 2.5 km away from the source [10]. Other prominent uses of radio waves have been in radar [11], astronomy and microwave heating [12].

Improvements in microwave sources and measurement techniques have permitted the development of accurate broadband spectroscopy and resonant techniques that have been utilised for the measurement of dielectric materials. Consequently, discoveries such as the strong contrast in dielectric permittivities of tumorous and healthy tissue has lead to the ability to distinguish tumours from other cellular tissue in the human body [13, 14]. Microwave heating methods have also been demonstrated as a means of altering enzyme-catalysed reactions, destruction of malignant neoplasia by hyperthermic therapy or thermotherapy for sterilisation and wound healing [15, 16, 17, 18].

The dielectric response of many polar liquids such as water, ethanol and acetone varies according to the strength of molecular dipoles and the density

of dipole moments. Subsequently security applications have been developed for the purpose of liquid threat detection [19].

1.0.1 Motivation

Biomedical microwave techniques have typically been limited to heating effects and tumour imaging [14] though many spectral features unique to the microwave spectrum and biological samples, specifically biological liquids, remain unexplored for diagnostic or analysis purposes. By analysing the complex permittivity of organic solutions from electrolytes to cellular solutions the aim is to discover and highlight means and methods to create new analysis techniques for furthering either physical understanding or for the development of biomedical applications.

1.0.2 Thesis outline

The work presented within this thesis focuses on the microwave dielectric analysis of polar liquids and organic solutions of varying complexities from electrolytes to whole blood. Based on the microwave dielectric response of electrolyte and protein solutions, differentiation techniques are explored using the spectral response of hydration water (water at the surface of a solute, often with different dynamics to bulk water) surrounding many salts and proteins. The most important finding of this work is the discovery of a means to conduct non-destructive haematological analysis that provides accurate haemoglobin (Hgb) concentration measurements on sample sizes less that a microlitre. This is achieved using a high frequency microwave (GHz) dielectric resonator using low-loss dielectrics and microfluidic integration to produce a highly sensitive and stable biosensor.

The thesis comprises of seven chapters, two outlining the theoretical background of electromagnetics, polar liquids, and measurement techniques and three on the experimental dielectric findings of electrolyte and biological solutions.

Chapter 2 introduces the fundamental mechanisms responsible for permittivity focusing in particular on polar liquids. The Clausius-Mossotti and Onsager models are used to explain the permittivity of materials, in particular polar liquids. The time-dependent interaction of a material with an electromagnetic wave is discussed and in the case of polar liquids the limit of reorientation examined in terms of Debye relaxation. Extended Debye models for complex systems are presented as well as conductivity and dielectric temperature dependence.

Current measurement techniques employed for dielectric spectroscopy and single frequency analysis are discussed in **Chapter 3**. In particular focus is given to coaxial techniques for broadband spectroscopy on large sample volumes and dielectric resonators for material characterisation on volumes of the order of μL (nm^3).

Measurements of polar liquids and electrolytes are presented in **Chapter 4**. Studies of the response of polar liquids and electrolytes are compared and discussed with respect to literature.

Chapter 5 explores the dielectric response of protein solutions and examines the best means to deconvolve the dielectric spectrum. Based on the observed response two methods are presented for differentiating pure protein solutions by utilising hydration effects surrounding a protein. Having examined pure protein solutions studies were conducted on more complex solutions namely whole blood. The dielectric impact of the most common solutes within blood are examined. The findings demonstrate the importance of haemoglobin (Hgb), serum proteins and electrolytes on the microwave response of blood. A method to determine the concentration of the aforementioned constituents is proposed.

Chapter 6 builds upon the Hgb methodology outlined in Chapter 5 and applies a dielectric resonator technique outlined in Chapter 3 that is capable of conducting dielectric measurements on volumes as low as 500 nL. By integrating a microfluidic system a device is developed that may determine Hgb levels to an accuracy equivalent to current commercial techniques and that is also non-destructive.

A summary of the thesis and results are given in **Chapter 7** as well as an outline of future work.

Chapter 2

Electromagnetic theory of liquids

2.1 Polarisation

A governing property of many electromagnetic interactions with matter is a material's polarisability; the fundamental property that underpins a material's dielectric properties. Various forms of polarisability occur even in an electrically neutral material, atoms polarise thereby forming dipoles, in liquid phases permanent dipoles reorientate in an electric field and ions in an ionic crystal are displaced. Atomic polarisation can be explained by classical means using an atom with a spherical electron cloud of charge e and radius R. Note that in real systems the electron cloud consists of atomic orbitals that are non-spherical. The electric field $\mathbf{E}$ arising from charge q_{enc} at distance r can be calculated using Gauss's law [20]

$$\oint_S \mathbf{E} \cdot d\mathbf{S} = \frac{q_{enc}}{\epsilon_0}, \tag{2.1}$$

where $d\mathbf{S}$ is the elemental surface of the closed Gaussian surface, ϵ_0 the permittivity of free space and q_{enc} the charge enclosed by the Gaussian sphere of radius r (Fig. 2.1A). Outside the electron cloud at distance r the electric

field is

$$\mathbf{E} = \frac{1}{4\pi\epsilon_0}\frac{q_{enc}}{r^2}\hat{\mathbf{r}}. \tag{2.2}$$

The concept of an electric field is used to describe the force a particle of charge q would impart upon another of charge q_2 at distance r. An electric field is also the gradient of the electric potential Φ at a point $\mathbf{r}$ arising from the charge q which gives a charge q_2 an electric potential energy (the work done to move the charge q to position $\mathbf{r}$ from infinity). Within the electron cloud the electric field is given as in (2.2) though q_{enc} is given as a ratio of the total charge depending on the electron shell volume and the enclosed volume of the Gaussian surface at distance r such that

$$q_{enc} = q_{total}\frac{V_{Gauss}}{V_{total}} = -q\frac{r^3}{R^3}, \tag{2.3}$$

where q is the total charge of the electron cloud (Fig. 2.1B). By substitution of (2.3) into (2.2) we arrive at the electric field at position r within the cloud (Coulomb's Law [21]),

$$\mathbf{E} = \frac{-q\mathbf{r}}{4\pi\epsilon_0 R^3}. \tag{2.4}$$

If an external homogeneous electric field $\mathbf{E_0}$ is applied and the positively charged nucleus and electron cloud are displaced by distance $\mathbf{d}$, we may then assume that the force of the external electric field acting on the charges is equal to the force between the displaced charges (Fig. 2.1D). The force acting on the nucleus of charge q is therefore proportional to the electric field of the cloud at distance $r = d$ such that

$$\mathbf{F} = q\mathbf{E_0} = q\mathbf{E_{cloud}} = \frac{-q^2\mathbf{d}}{4\pi\epsilon_0 R^3}. \tag{2.5}$$

The equilibrium distance at which the external and internal forces acting on the charges are equal is given by

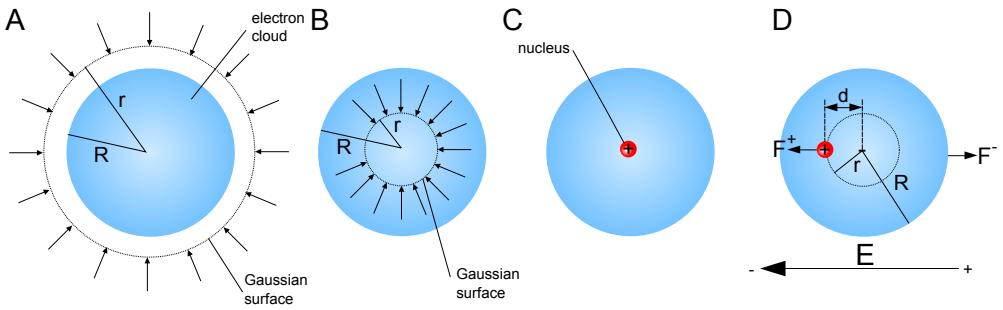


Figure 2.1: An electron cloud surrounding a nucleus (A) with a Gaussian sphere outside (B) and inside the cloud (C). Subjected to an external electric field the cloud displaces relative to the electric field thereby inducing a dipole (D).

$$\mathbf{d} = 4\pi\epsilon_0 R^3 \frac{\mathbf{E_0}}{q}, \tag{2.6}$$

and the induced dipole moment as

$$\mathbf{p} = q\mathbf{d} = 4\pi\epsilon_0 R^3 \mathbf{E_0} = \epsilon_0 \alpha \mathbf{E_0}, \tag{2.7}$$

where $\alpha = 4\pi R^3$ and is the atomic polarisability of the molecule (Fig. 2.1). The direction of the vector of the induced dipole moment is given in the same direction as the applied electric field though unlike an electric field it travels from a negative to a positive charge. The polarisation of a material comprising of multiple atoms is given as the linear (vector) sum of dipoles per unit volume,

$$\mathbf{P}(\mathbf{r}) = N_i \langle \mathbf{p}_i \rangle, \tag{2.8}$$

where N_i is the average number of molecules per unit volume at a point $\mathbf{r}$ and $\langle \mathbf{p}_i \rangle$ is the average dipole moment of a molecule at point $\mathbf{r}$. This model, though simple, provides the building blocks for many macroscopic and microscopic observations that can be confirmed experimentally. Assuming that all dipole moment are orientated parallel we arrive at

$$\mathbf{P} = N\epsilon_0\alpha\mathbf{E_0}. \tag{2.9}$$

If an external electric field $\mathbf{E}$ is applied and the material polarised to $\mathbf{P}$ then the resultant electric displacement field is

$$\mathbf{D} = \epsilon_0\mathbf{E_0} + \mathbf{P}. \tag{2.10}$$

By substituting (2.7) into (2.9) it may be approximated that the polarization is proportional to the applied electric field such that

$$\mathbf{P} = \epsilon_0\chi\mathbf{E}_0, \tag{2.11}$$

where χ represents a materials electric susceptibility. By substitution of (2.11) into (2.10) we arrive at

$$\mathbf{D} = \epsilon_0(1+\chi)\mathbf{E}_0 = \epsilon_0\epsilon_r\mathbf{E}_0, \tag{2.12}$$

where $\epsilon_r = 1 + \chi$. This provides a relative permittivity ϵ_r that ties the applied electric field to the resultant displacement field. ϵ_r remains scalar for all isotropic and homogeneous materials but becomes a second order tensor when materials are anisotropic and a function of position with inhomogeneity. A material with a relative permittivity greater than one could also be thought of as storing energy proportional to the value of its permittivity.

2.1.1 Induced dipoles and the Clausius-Mossotti equation

The material descriptions laid out thus far are accurate for materials where the atomic constituents are displaced at a large distance. However, the relationship between permittivity and molecular properties described in (2.10) and (2.12) are found to be incomplete when dealing with dense materials due

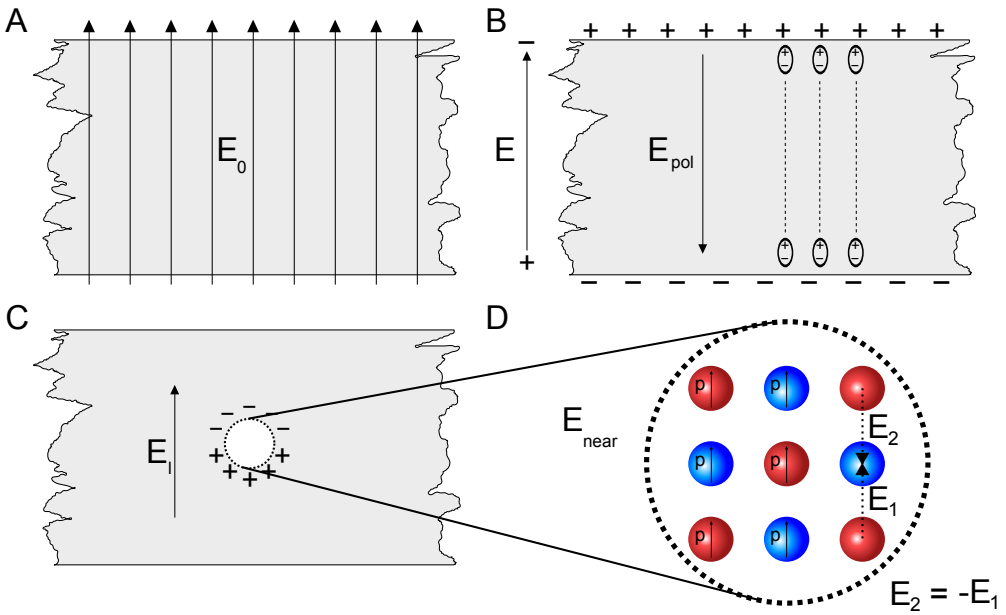


Figure 2.2: Visual depiction of the Clausius-Mossotti model used to solve for the local electric field in a material. The local electric field may be solved from the applied electric field (A), depolarisation field (B), macroscopic polarisation effects (C) and atomically local polarisation (D).

to the interaction of dipoles from atomically local atoms. The local field $\mathbf{E}_l$ (the electric field experienced by a single particle) is comprised of a number of polarisation effects in addition to the applied electric field. Using the approach of Lorentz there are three material polarisation effects to consider to calculate $\mathbf{E}_l$; de-polarisation induced by dipoles at the surface of the material (Fig. 2.2B), the atomic interactions from atoms surrounding the particle of interest (defined to be an atom or ion within a sphere of radius r) (Fig. 2.2D) and lastly the polarisation effects from outside of the sphere (Fig. 2.2C).

$$\mathbf{E_l} = \mathbf{E_0} + \mathbf{P}_{depol} + \mathbf{E}_{atoms} + \mathbf{E}_{out}. \tag{2.13}$$

The de-polarisation field is dependent on the material thickness, thus for materials that are not atomically thin the de-polarisation effects are considered to be negligible. The following theoretical approach to describe the dielectric response of a solid is based upon the assumption that the material is of an atomically cubic arrangement and an ionic crystal (i.e. NaCl) or in the case

of atoms that the induced atomic dipoles are point dipoles. The total electric field contribution from the surrounding molecules is found to be zero (Fig. 2.2D) owing to the equal spacing of dipoles or ions. Beyond the radius of the sphere the material consists of polarisable ions or atoms with a relative permittivity ϵ_r. The resulting solution to $\mathbf{E}_l$ is calculated as though the atom or ion of interest is suspended in a hollow sphere of radius r within a material of ϵ_r (Fig. 2.2C). In a homogeneous electric field a hollow sphere in a material of permittivity ϵ_r is polarised with a surface charge γ such that

$$\gamma = -\mathbf{P} \cdot \hat{\mathbf{r}} = -P \cos\theta, \tag{2.14}$$

where θ is the angle between the polarisation $\mathbf{P}$ and $\mathbf{r}$ (Fig. 2.2). The negative sign corrects for the orientation of the dipole moments. By integrating over the surface of the sphere the sum of the electric field from the surface charge is calculated to be

$$\mathbf{E} = \frac{\mathbf{P}}{3\epsilon_0}. \tag{2.15}$$

The sum of the average electric field in the dielectric and the influence of other molecules within the sphere yields the local electric field,

$$\mathbf{E_l} = \mathbf{E_0} + \frac{\mathbf{P}}{3\epsilon_0}. \tag{2.16}$$

By substituting (2.7) and (2.11) into (2.16) we arrive at

$$\frac{N\alpha}{3} = \frac{\epsilon_r - 1}{\epsilon_r + 2}. \tag{2.17}$$

This is known as the Clausius-Mossotti equation that relates the polarisability or static permittivity of a molecule to its intrinsic properties in a solid, isotropic and homogeneous cubic crystalline material [22, 23]. This equation can also be derived by re-arrangement of (2.16) and substituted into (2.10) along with (2.7) and (2.11) where $\mathbf{D} = \epsilon\mathbf{E}$.

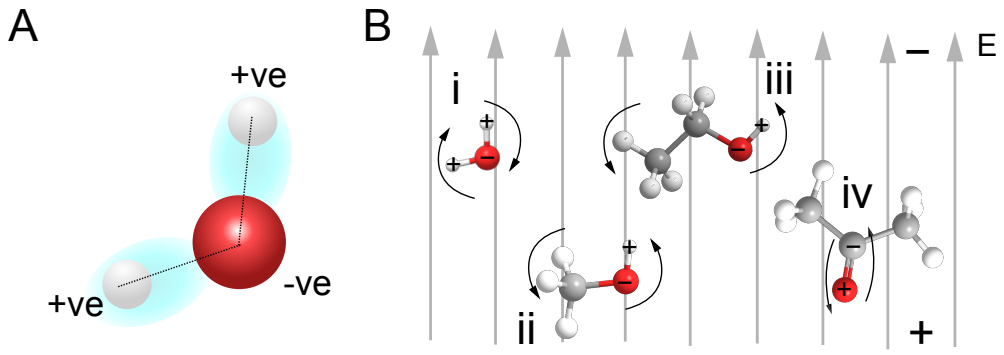


Figure 2.3: A water molecular depicting the charge distribution (A). Polar liquids exhibit a range of possible reorientational mechanisms (B).

2.1.2 Reorientational polarisation

Polar molecules in a liquid state have additional degrees of freedom in which they may respond to an applied electric field (rotational polarisation) compared to solids. The first step to understanding the dielectric response of a polar liquid is by studying how a molecule in a thermally active system may response to an electric field.

The effective dipole moment of a polar molecule in a thermally active system with an applied homogeneous electric field can be considered to be the average dipole moment calculated from the distribution of all molecules (Fig. 2.4A). If an electric field is applied we may assume that owing to the molecular thermal energy (k_BT) this will lead to a distribution of orientated states depending on the magnitude of the applied field. To calculate the average dipole moment at a temperature T we use the Boltzmann distribution to provide a statistical model for the number of molecules with an electric field interaction energy of U such that

$$N(U) = A \cdot \exp \frac{-U(\theta)}{k_BT}, \tag{2.18}$$

where A is an undefined constant and k_B the Boltzmann constant. The dipole interaction energy $U(\theta)$ with the applied electric field is given by

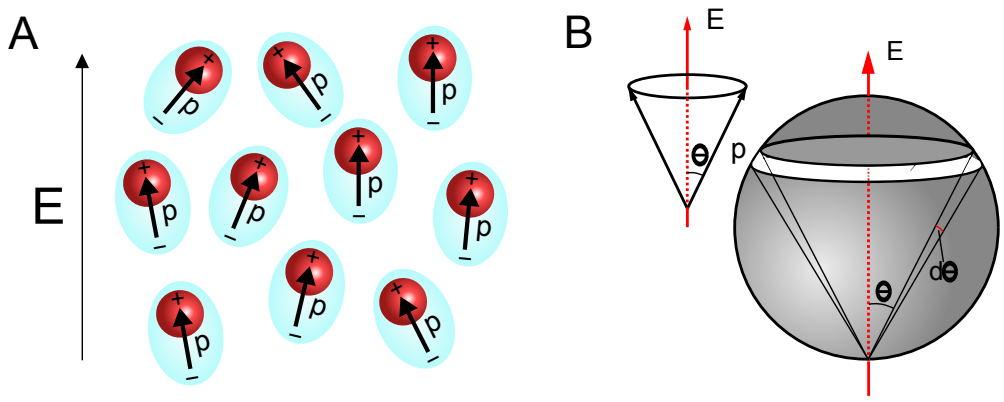


Figure 2.4: The average distribution of dipole moments in an electric field due to thermal distribution (A). A visual representation of the integration over the dipole distribution (B).

$$U(\theta) = \mathbf{p} \cdot \mathbf{E} = pE\cos\theta \tag{2.19}$$

where θ is the angle between the applied electric field and the molecular dipole moment (Fig 2.4). The number of molecules with a given interaction energy $U(\theta)$ is therefore dependent on the interaction angle. To calculate the average molecular dipole moment we must integrate across all possible angles (Fig. 2.4B) thereby calculating the total average polarization and normalise against the number of molecules. The average dipole moment is therefore

$$\langle p_F \rangle = \frac{\int_0^\pi N(U(\theta)) \cdot p \cdot \cos\theta \cdot d\Omega}{\int_0^\pi N(U(\theta)) \cdot d\Omega} \tag{2.20}$$

where $d\Omega$ is $sin\theta d\theta$. The numerator of (2.20) is the sum of the dipole moment in the same directional component as the electric field. The denominator is the normalisation from the total number of molecules N. This leaves us with a description of the average dipole moment though one that is dependent on the magnitude of the electric field and temperature. Let us examine the average directional component of (2.20) by removing $\mathbf{p}$ and substituting the identities $x = \cos\theta$ and $\beta = pE/k_BT$ to arrive at

$$\langle \cos\theta \rangle = \frac{\int_{-1}^{1} x \exp \beta x dx}{\int_{-1}^{1} \exp \beta x dx} = \frac{e^{\beta} + e^{-\beta}}{e^{\beta} - e^{-\beta}} - \frac{1}{\beta} = \coth \beta - \frac{1}{\beta}. \tag{2.21}$$

This identity is known as the Langevin function. In the case of $\beta << 1$ the right hand side of (2.21) reduces to $\beta/3$ and for $\beta > 1$ the equation tends to 1. In practice electric field strengths high enough to move out of the low-limit case are rarely produced, especially in dielectric measurement techniques and even in a microwave oven. The average dipole moment in weak electric fields is given as

$$\langle p_F \rangle = \frac{p^2}{3k_B T}\mathbf{E}. \tag{2.22}$$

Polar liquids will experience both the aforementioned polarisation as well as induced polarisation from surrounding molecules. Therefore the polarisation is

$$\mathbf{P} = \mathbf{P_{ind}} + \mathbf{P_{or}} = N\left(\alpha + \frac{p^2}{3k_B T}\right)\mathbf{E} \tag{2.23}$$

where $P_{ind/or}$ are the induced and orientational polarisation, respectively.

Assuming that the liquid is in a highly ordered state the Clausius-Mosotti equation can be reformulated to incorporate induced and rotational polarisation by combination of (2.23) and (2.17), giving

$$\frac{N}{3}\left[\alpha + \frac{p^2}{3k_B T}\right] = \frac{\epsilon_r - 1}{\epsilon_r + 2}. \tag{2.24}$$

This variation of the Clausius-Mosotti equation was first proposed by Debye ($\epsilon_{ind} = 1$) [24] to account for the temperature dependence observed in many liquids and which subsequently led to the proposal that some molecules had permanent dipoles. Onsager observed that a difference existed between the dipole moments of high permittivity liquids in the gas and the liquid phase. It has been found that in high permittivity liquids where the molecules are in

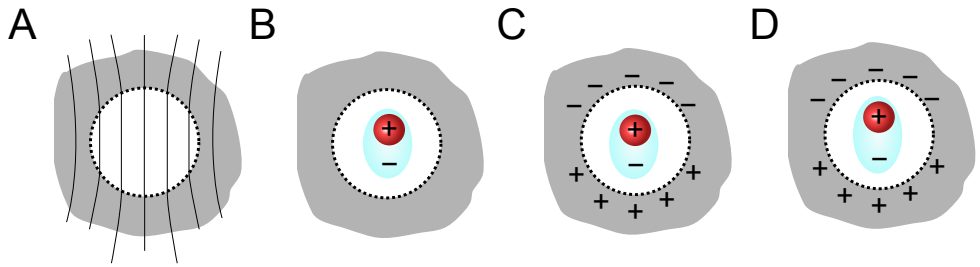


Figure 2.5: Onsager's approach to solving the local electric field. The change in the electric field due to different permittivities inside and outside the sphere (A). The polarised molecule within a sphere (B). The polarisation of the surrounding medium (C). The additional polarisation of the molecule by the surrounding medium (D).

close proximity to each other there is a strong dipole-dipole interaction. This interaction induces an additional polarisation thereby increasing the dipole moment.

Two models have been developed to account for the discrepancy described which both make use of continuum approaches (the use of cavities with a continuous material outside of it) and only differ in the relative atomic dimensions of the cavity. Onsager reduced the spherical cavity of microscopic interactions to include just a single molecule [25]. He also introduced the concept of a reactive electric field. This was constructed on the basis that a solute with dipole moment $\mathbf{p}$ was placed in a sphere of radius a, surrounded by a homogeneous, polarisable medium of dielectric constant ϵ. The presence of the dipole moment $\mathbf{p}$ polarises the surrounding medium (Fig. 2.5B) that in turn creates an additional electric field known as the reactive electric field $\mathbf{E}_r$ (Fig. 2.5C) that acts upon the existing dipole moment and increases the polarisation (Fig. 2.5D). The reactive field is therefore proportional to the original dipole moment. The total field acting on the dipole moment is given as

$$\mathbf{E_l} = \mathbf{E_c} + \mathbf{E_R}, \tag{2.25}$$

where $\mathbf{E}_c$ is the applied electric field within the cavity and $\mathbf{E}_R$ the reactive field. The applied field in the cavity is calculated from the sum of the external

field in the continuous dielectric and the induced polarisation at the surface of the sphere such that

$$\mathbf{E_c} = \mathbf{E_d} + \frac{\mathbf{P}}{3\epsilon_0\epsilon_r}, \tag{2.26}$$

This result is similar to (2.16) though in this case it is the polarisation of the medium outside the cavity that leads to the additional electric field inside the cavity. By substitution of (2.11) into (2.26) , where $\mathbf{E}_0 = \mathbf{E}_c$, the applied electric field within the cavity in terms of the electric field in the dielectric is

$$\mathbf{E_c} = \frac{3\epsilon_r}{2\epsilon_r + 1}\mathbf{E_d}, \tag{2.27}$$

Considering the effect of the dipole acting on the surrounding medium the polar molecule induces a charge distribution in the dielectric medium such that

$$\mathbf{E} = \frac{\mathbf{P}}{3\epsilon_0\epsilon_r}. \tag{2.28}$$

This electric field then acts on the cavity according to (2.27) giving us

$$\mathbf{E_r} = \frac{1}{2\epsilon_r + 1}\mathbf{P}. \tag{2.29}$$

The polarisation of the dielectric is dependent on the polar molecule within the cavity (2.10) such that $\mathbf{P_d} = (\epsilon_r - 1)\mathbf{E}_c$ where the electric field is as given in (2.7). This results in an expression for the reactive field

$$\mathbf{E_r} = \alpha\frac{\epsilon - 1}{2\epsilon + 1}\mathbf{p}. \tag{2.30}$$

The sum of the cavity and reactive field yield the total electric field experienced by the dipole which induces an additional dipole moment on the permanent dipole. Note however that only the cavity field applies torque on

the dipole and rotate it owing to the reactive field always being parallel to the dipole moment. We can re-express (2.23) with a correction to the electric field experienced by the molecule as

$$\mathbf{P} = \mathbf{P_{ind}} + \mathbf{P_{or}} = \frac{N}{3\epsilon_0}\frac{3\epsilon_r}{2\epsilon_r + 1}\left(\alpha + \frac{p^2}{3k_BT}\right)\mathbf{E_d}. \tag{2.31}$$

Using the fundamental electrostatic formula (2.10) where the polarisation is given by (2.31) and ($\mathbf{D} = \epsilon\mathbf{E}_d$) we arrive at

$$(\epsilon_r - 1)\mathbf{E}_d = \frac{N}{3\epsilon_0}\frac{3\epsilon_r}{2\epsilon_r + 1}\left(\alpha + \frac{p^2}{3k_BT}\right)\mathbf{E_d}. \tag{2.32}$$

This then simplifies to

$$\frac{(\epsilon_r - 1)(2\epsilon_r + 1)}{3\epsilon_r} = \frac{N}{3\epsilon_0}\left(\alpha + \frac{p^2}{3k_BT}\right). \tag{2.33}$$

which is known as the Onsager model [25]. Note that in the case of two systems contributing to the permittivity such as reorientation polarisation and induced polarisation then (2.33) is re-expressed in terms of both permittivities such that

$$\frac{(\epsilon_{or} - \epsilon_{ind})(2\epsilon_{or} + \epsilon_{ind})}{\epsilon_{or}(\epsilon_{ind} + 2)^2} = \frac{Np^2}{9\epsilon_0 k_BT}. \tag{2.34}$$

This version was given in his original work ([25], equation (27)) with the difference of $\epsilon_{ind} = n^2$ and $p = \mu_0$.

Using given experimental values ($\epsilon_{or} = 70$, $\epsilon_{ind} = 5$, T=300 K) the dipole moment of a water molecule may be calculated to be approximately 1.6 D (5.5×10^{-30} Cm). Known values of water's dipole moment are given as 1.85 D (6.2×10^{-30} Cm).

Unlike Onsager the Kirkwood approach to the relationship between a materials dielectric properties and microscopic properties incorporated a number of

molecules surrounding the molecules of interest into the microscopic sphere to account for local structure and interactions. The difference to the Onsager equation comes from having to account for the average polarisation of a collection of molecules within the sphere before accounting for the reactive field. Subsequently (2.35) can be re-expressed as [26]

$$\frac{(\epsilon_{or} - \epsilon_{ind})(2\epsilon_{or} + \epsilon_{ind})}{\epsilon_{or}(\epsilon_{ind} + 2)^2} = g\frac{Np^2}{9k_BT}. \tag{2.35}$$

g is the scalar corrective parameter that defines the short-range orientational order of the local molecules such that,

$$g = \frac{\langle M^2 \rangle}{Np^2}, \tag{2.36}$$

where p_0 is the molecular dipole moment, N the number of molecules and $\langle M^2 \rangle$ the mean square average of the total dipole moment of the cavity. Depending on how the cavity encompassing the molecules is defined relates to the outcome of the local electric field. Subsequently much work has been conducted on defining the ideal cavity for polar liquids and the molecular orientation in an electric field [27, 28].

2.2 Propagating electromagnetic waves in dielectrics

Up until now the material dielectric response has been based upon static electric fields however in a time varying electric field new material effects must be explored.

2.2.1 Maxwell's equations

Maxwell's equations are built around Gauss's laws, both magnetic and electric, Faraday's law of induction and Ampere's law with Maxwell's correction

(noting that changing electric fields also induce magnetic fields and therefore allowing for the postulation of the self-sustaining electromagnetic wave), which together provide the building blocks for all electromagnetic interactions. These four relationships were originally developed around electrostatics and low frequency AC currents and at the time of their discovery and consolidation there was no confirmation of light being a part of the electromagnetic spectrum. The equations are given as [1]

$$\nabla.\mathbf{D} = \rho_f, \tag{2.37}$$

$$\nabla.\mathbf{B} = 0, \tag{2.38}$$

$$\nabla \times \mathbf{E} = -\frac{\partial \mathbf{B}}{\partial t}, \tag{2.39}$$

$$\nabla \times \mathbf{H} = \mathbf{j}_f + \frac{\partial \mathbf{D}}{\partial t}, \tag{2.40}$$

where $\mathbf{B}$ is the magnetic flux density, $\mathbf{j}_f$ is the free current density and $\mathbf{H}$ the magnetic field strength. From (2.39) and (2.40) it is apparent that a changing electric field induces a magnetic field that is perpendicular to the direction of change and vice versa.

2.2.2 Wave equations

From Maxwell's equations one can derive the wave equations for which electromagnetic waves must obey within a vacuum. By taking the curl of (2.39) and (2.40) and using the identity of $\nabla \times \nabla \times \mathbf{F} = \nabla(\nabla \cdot \mathbf{F}) - \nabla \cdot (\nabla \mathbf{F})$ we arrive at

$$\nabla^2 \mathbf{E} - \frac{1}{c^2}\frac{\partial^2 \mathbf{E}}{\partial^2 t} = 0, \tag{2.41}$$

$$\nabla^2 \mathbf{B} - \frac{1}{c^2}\frac{\partial^2 \mathbf{B}}{\partial^2 t} = 0. \tag{2.42}$$

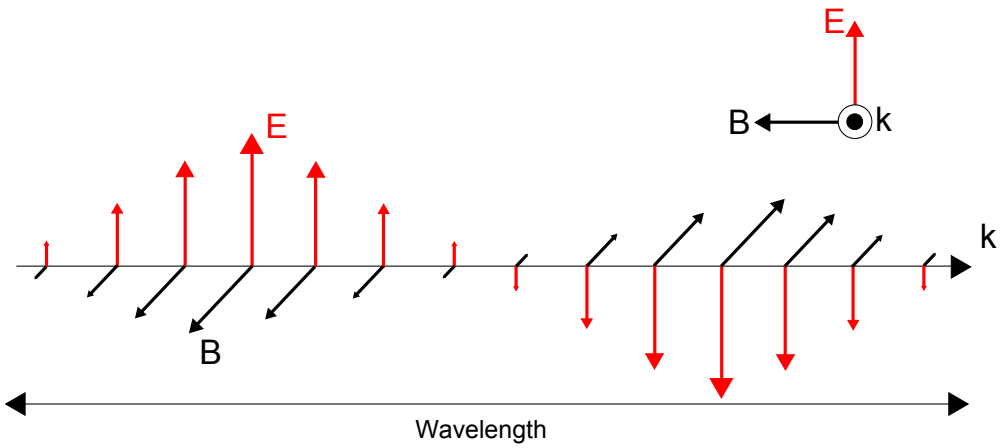


Figure 2.6: A propagating EM plane wave with wavevector $\mathbf{k}$ and frequency f.

Sinusoidal solutions to (2.41) and (2.42) are given as

$$\mathbf{E} = \mathbf{E_0} \exp(i(\mathbf{k} \cdot \mathbf{r} - \omega t)), \tag{2.43}$$

and

$$\mathbf{B} = \mathbf{B_0} \exp(i(\mathbf{k} \cdot \mathbf{r} - \omega t)), \tag{2.44}$$

provided that the speed of propagating wave (Fig. 2.6) c is

$$c = \frac{1}{\sqrt{\mu\epsilon}}. \tag{2.45}$$

The given solutions describe electromagnetic plane waves that are constant frequency with infinite parallel wavefronts. The speed of the propagating wave also directly related to the frequency f (angular frequency $\omega = 2\pi f$) and wavelength λ (wavevector $k = 2\pi/\lambda$) such that $c = f\lambda = \omega/k$. Note also that the electric field must be related to the magnetic field by

$$\mathbf{B} = \frac{1}{c}\left(\hat{\mathbf{k}} \times \mathbf{E}\right) \tag{2.46}$$

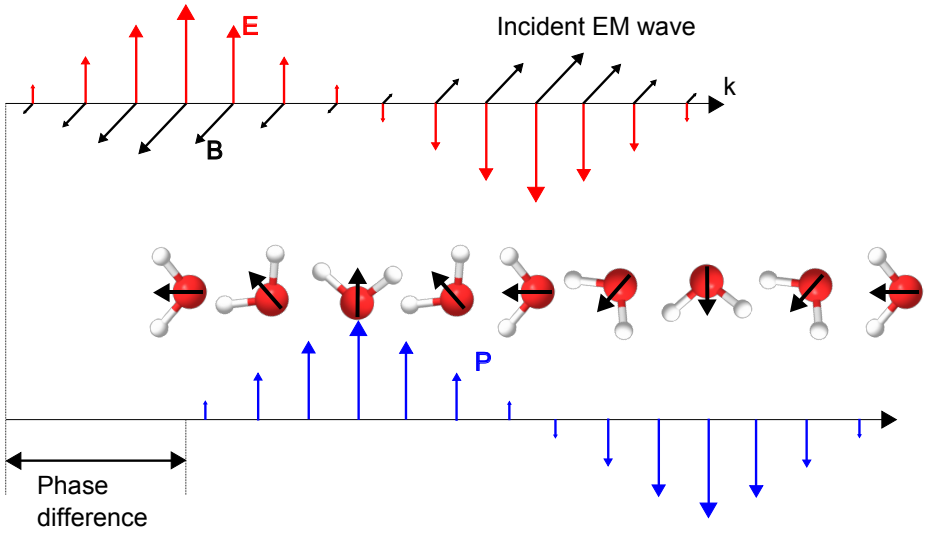


Figure 2.7: Phase difference between an applied electric field and a polar molecule.

By inserting the known constants of the permittivity and permeability of free space we arrive at the speed of light and it was this discovery that lead to Maxwell's realisation that light was likely a sinusoidal propagating wave.

From the solutions to (2.41) and (2.42) it is apparent that they are complex in nature (Euler's formula). The real component of the solution describes the waves magnitude and the imaginary component provides information on the progress of the waves cycle known as phase ϕ.

$\mathbf{H}$ is linearly proportional to $\mathbf{B}$ in paramagnetic and diamagnetic materials such that

$$\mathbf{H} = \frac{\mathbf{B}}{\mu}, \tag{2.47}$$

where μ is the permeability of the medium.

As previously discussed the electric field at a point $\mathbf{r}$ in a material of permittivity ϵ will see an increased local electric field according to (2.16). However, unlike the discussed static case there is also the time dependent response to consider.

2.2.3 Phase

A polar molecule in a liquid phase and in a homogeneous time varying electric field will not respond instantaneously to the field owing to a degree of resistance arising from the moment of inertia of the molecule and the breaking of bonds with surrounding molecules.

The polar molecule will respond with the same driving frequency f of the incident electric field though with a phase difference δ due to this resistance to displacement (Fig. 2.7). From (2.12) we know that permittivity is dependent on the ratio of $\mathbf{D}$ and $\mathbf{E}$, however, if $\mathbf{D}$ responds with a phase difference of δ then the permittivity must contain a phase difference such that

$$\epsilon^*(\omega) = \epsilon'(\omega) + i\epsilon''(\omega) = \frac{D_o}{E_0}(\cos\delta + i\sin\delta). \tag{2.48}$$

If a material has a permeability, μ, the incident electromagnetic wave will interact with the materials magnetic dipoles with magnitude and phase change of

$$\mu^*(\omega) = \mu'(\omega) + i\mu''(\omega) = \frac{B_0}{H_0}(\cos\delta + i\sin\delta). \tag{2.49}$$

The oscillation of the polar molecules leads to the re-emission of the radiation absorbed albeit with a corresponding phase difference. In the case of a homogeneous and isotropic distribution of polar molecules the resulting re-emission leads to a reduction in the wave's phase velocity as well as a decrease in the wavelength by a factor known as the refractive index n. The phase difference is highly dependent on the driving wave frequency as at low frequencies the different would be negligible however at frequencies near the systems natural orientation time the phase difference is large. This difference in phase is addressed in later sections.

Note that the imaginary component of permittivity is is a direct result of the phase difference. The resistance of a molecule to reorientation leads to a dissipation of energy (such as the breaking and formation of intermolecular

bonds) and therefore the imaginary component may also be approached as a measurement of loss.

2.2.4 Losses

The relationship between the phase velocity of light and permittivity given in (2.45) ties the permittivity to the wavevector by $k = \omega/c$. The relative change to the speed of light is therefore

$$n + i\alpha = \sqrt{\epsilon_r'(\omega) + i\epsilon_r''(\omega)}, \tag{2.50}$$

and where n is the refractive index (change in wave phase velocity and wavelength) and α the absorption coefficient. With known values of permittivity the refractive index and absorption coefficient can be solved using the rearrangement

$$n^2 - \alpha^2 = \epsilon_r', \tag{2.51}$$

$$2n\alpha = \epsilon_r''. \tag{2.52}$$

By substitution of (2.50) into (2.43) losses of the wave solution becomes

$$\mathbf{E} = \mathbf{E}_0 \exp(-\alpha k z) \exp i(\mathbf{k} \cdot \mathbf{r} - \omega t). \tag{2.53}$$

With increasing α we find that the propagating plane wave decays quicker.

When making dielectric measurements a more common approach to giving values of loss is to measure the ratio of the imaginary permittivity and real permittivity. The ratio is therefore the energy lost against energy stored which provides a relative medium loss known as the loss tangent, $\tan\delta$

$$\tan\delta = \frac{\epsilon''(\omega)}{\epsilon'(\omega)}. \tag{2.54}$$

The research conducted within this thesis will focus upon and be discussed in terms of the complex permittivity and loss tangent of the materials investigated.

2.2.5 Conductivity

The presence of free electrons, protons or ions in semiconductors, metals, liquids and gases lead to additional losses within a system. With no restoring force acting on the ions they follow the path of the applied electric field. The free ions collide with particles leading to a dissipation of kinetic energy by exciting molecular vibration or imparting kinetic energy. The ionic losses are highly frequency dependent with lower frequencies leading to increased path lengths and a greater number of intermolecular interactions (ionic drag) that equate to higher losses. Losses and the phase difference of free charge carriers are commonly denoted separately from the permittivity and phase information of bound charges such that the imaginary permittivity becomes

$$I(\epsilon^*(\omega)) = \epsilon''(\omega) + \frac{\sigma}{\omega\epsilon_0}, \tag{2.55}$$

where σ is the conductivity.

2.2.6 The Debye model

The dielectric response of a material to an electromagnetic wave can be given in complex form that in the case of a polar molecule in a liquid state arises from the molecular moment of inertia and interactions with surrounding molecules. The molecular interactions and moment of inertia limits the speed at which a molecule responses and relaxes when an electric field $\mathbf{E}$ is switched on and off, respectively. The time taken for a molecule to respond to such a

field is given as the relaxation time τ. In a time-dependent electric field when the frequency is low enough the molecule will continue to response almost in phase with the incident wave. As the frequency increases and approaches the limiting speed at which the molecule can respond then the phase difference increases. As the frequency increases it also limits the molecules ability to orientate in the electric field. The molecule still oscillates at the same frequency though does not complete a full orientation and is therefore more prone to re-bond with surrounding molecules and dissipate energy to them. At even higher frequencies the molecules no longer reorientate in the electric field and therefore exhibit no phase difference, loss or real permittivity. All that remains are induced dipoles that contribute to the permittivity.

This process is described by the Debye relaxation equation and can be formulated by considering the time-dependent evolution of the polarisation of the molecule as it relaxes [29]. We may begin by assessing the simplest case of a collection of dipoles with polarization $\mathbf{P}$ in an electric field $\mathbf{E}$. Once the electric field has been removed the dipoles will return to their lowest energy state and subsequently lead to an exponential decay of polarization as a function of time such that

$$\mathbf{P}(t) = \mathbf{P}_0 \exp -(t/\tau), \tag{2.56}$$

where τ is the molecules inherent relaxation time defined by the Einstein equation to be

$$\tau = \frac{r^2}{6D}, \tag{2.57}$$

where D is the diffusivity of a particle in the liquid and r the molecules effective radius. If we know the time evolution of the polarisation we are able to understand the frequency dependent response to a driven field by taking the Laplace transform ($t \geq 0$) of the time-dependent polarisation such that

$$\mathbf{P}(\omega) = \frac{1}{\tau}\int_0^\infty \mathbf{P}(t)\exp -(i\omega t)dt = \frac{\mathbf{P}_0}{\tau}\int_0^\infty \exp -(t/\tau)\exp -(i\omega t)dt. \quad (2.58)$$

The solution to this integral is given as

$$\mathbf{P}(\omega) = \frac{\omega_0 \mathbf{P}_0}{\omega_0 + i\omega} \quad (2.59)$$

where $\omega_0 = \tau^{-1}$. We can re-express (2.11) in the frequency domain such that

$$\mathbf{P}(\omega) = \epsilon_0 \chi(\omega)\mathbf{E}(\omega), \quad (2.60)$$

where $\chi(\omega)$ is the complex susceptibility including the phase difference between $\mathbf{P}(\omega)$ and $\mathbf{E}(\omega)$. From (2.60) (2.59) can be shown to be

$$\frac{\mathbf{P}(\omega)}{\mathbf{E}(\omega)} = \epsilon_0\chi(\omega) = \frac{\mathbf{P}_0}{\mathbf{E}_0}\frac{\omega_0}{\omega_0 + i\omega} = \chi_s \frac{\mathbf{1}}{1 + i\omega\tau} \quad (2.61)$$

where $\chi_s = \mathbf{P}_0/\mathbf{E}_0$ is the static ($\omega = 0$) electric susceptibility. Expressing the frequency dependence of a dipole in terms of permittivity is more useful. In (2.10) we assumed that there is only one polarisation process. In many real systems there are almost always more than one polarisation system contributing to the permittivity and rarely do they undergo relaxation at the same frequencies. Let us take a medium that has two contributing polarisation. The electric displacement is given as

$$\mathbf{D}(\omega) = \epsilon_0\mathbf{E}(\omega) + \mathbf{P}_1(\omega) + \mathbf{P}_2(\omega) = \epsilon_0[1 + \chi_1(\omega) + \chi_2(\omega)]\mathbf{E}(\omega). \quad (2.62)$$

Let us assume that we are only interested in χ_2 (referred to as χ) and that χ_1 relaxes at a much higher frequency than we are interested in. Assuming an isotropic and homogeneous medium then (2.62) can therefore be rearranged to be

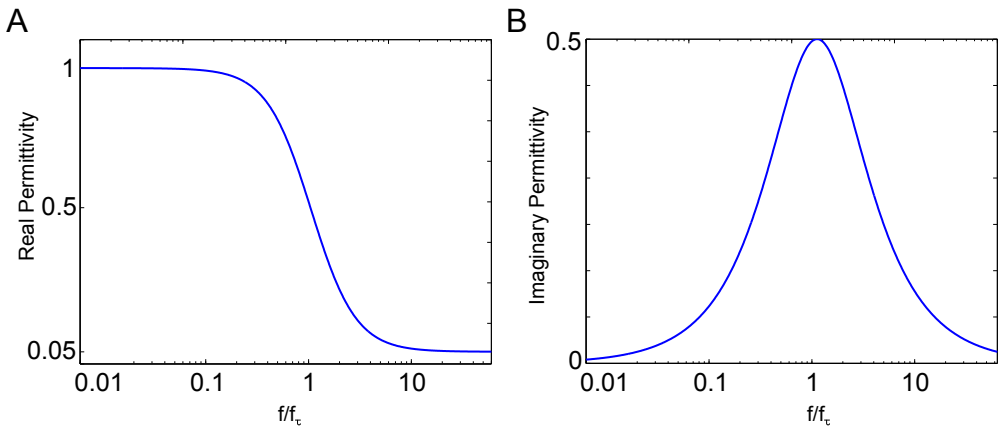


Figure 2.8: The real (A) and imaginary (B) permittivity from the Debye model across the relaxation frequency (f_τ) of the polar mechanism ($\epsilon_s = 1$, $\epsilon_\infty = 0.05$).

$$\mathbf{D}(\omega) = \epsilon_0(\epsilon_\infty + \chi(\omega))\mathbf{E}(\omega), \tag{2.63}$$

where ϵ_∞ is the high frequency permittivity. Similarly to (2.12) we may say that $\epsilon(\omega) = \epsilon_\infty + \chi(\omega)$ and therefore for substitution into (2.61) that

$$\chi(\omega) = \epsilon(\omega) - \epsilon_\infty. \tag{2.64}$$

In the limit of low frequency ($\omega \to 0$) we arrive at

$$\chi_s = \epsilon_s - \epsilon_\infty, \tag{2.65}$$

where ϵ_s is the static permittivity. By substituting (2.64) and (2.65) into (2.61) we now arrive at the well known Debye relaxation equation (Fig. 2.8)

$$\epsilon^*(\omega) = \epsilon_\infty + \frac{\epsilon_s - \epsilon_\infty}{1 + i\omega\tau}. \tag{2.66}$$

Note that the numerator of the right hand side of (2.66) $\epsilon_s - \epsilon_\infty$ is often denoted as Δ. Note that according to previous assumptions, the use of a Debye model and any subsequent model related to the Debye response requires that

the system measured be independent of the intensity of **E** (as assumed in (2.22)), that is be in a steady state, in equilibrium and that $\epsilon(\omega)$ evolves as an ordinary causal response.

2.3 Extended relaxation models

In many media there are multiple relaxation processes occurring owing to the complex intermolecular network of molecules. This distribution can be expressed as a collection of polarisations such that electric displacement is

$$\mathbf{D}(\omega) = \epsilon_0 \left[1 + \sum_{k=1}^{N} \chi_k(\omega)\right] \mathbf{E}(\omega), \tag{2.67}$$

where N is the number or polarisation processes occurring. The Debye equation therefore becomes

$$\epsilon^*(\omega) = \epsilon_\infty + \sum_{k=1}^{N} \frac{\epsilon_k - \epsilon_{k+1}}{1 + i\omega\tau_k}. \tag{2.68}$$

In addition to permittivity contributions from the multiple polarisations we must also include ionic contributions from free ions as given in (2.55). This leads to

$$\epsilon^*(\omega) = \epsilon_\infty + \sum_{k=1}^{N} \frac{\epsilon_k - \epsilon_{k+1}}{1 + i\omega\tau_k} + \frac{i\sigma}{\omega_0}. \tag{2.69}$$

Thus far the equations used to describe relaxation processes of dipole moments have been built upon analytical derivations based upon physical processes. In particularly complex systems where there are a large distributions of relaxation phenomena occurring it often becomes more beneficial to adopt a semi-empirical approach to describe the distributions of relaxations such that

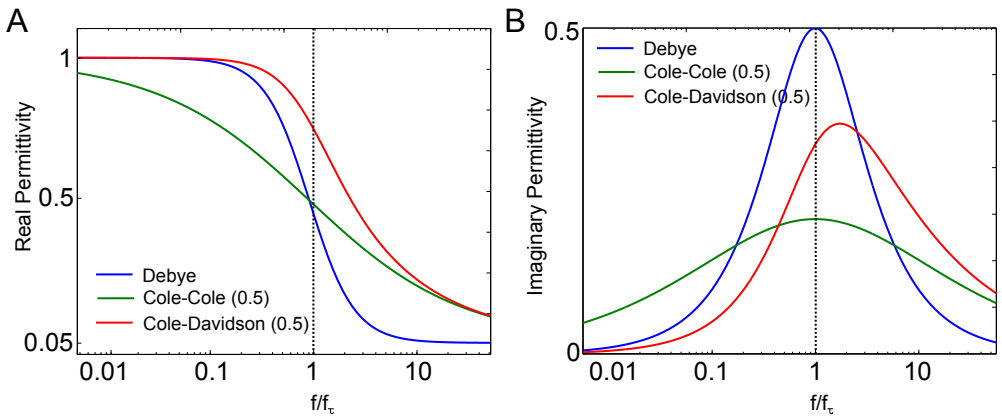


Figure 2.9: The real and imaginary permittivity comparing the response of a Cole-Cole ($\alpha = 0.5$), Cole-Davidson ($\beta = 0.5$) and a Debye model.

$$\epsilon^*(\omega) = \epsilon_\infty + (\epsilon_s - \epsilon_\infty) \int_{\tau_{min}}^{\tau_{max}} \frac{f(\tau) d\tau}{1 + i\omega\tau}. \tag{2.70}$$

The distribution of relaxation times $f(\tau)$ in (2.70) has many solutions and depends on the system analysed. Few of these solutions are based upon exact theoretical derivations instead they are developed around the response of real systems. The most common functions used are Cole-Cole [30, 31],

$$f(\tau) = \frac{\sin \alpha\pi}{2\pi \cosh[(1-\alpha)\ln \tau/\tau_0] - \cos \alpha\pi}, \tag{2.71}$$

where τ_0 is the central relaxation time of the distribution, Davidson-Cole [32],

$$f(\tau) = \frac{\sin \beta\pi}{\pi} \left(\frac{\tau}{\tau_0 - \tau} \right)^\beta, \tag{2.72}$$

and Fuoss-Kirkwood [33, 34],

$$f(\tau) = \frac{\gamma \cos(\gamma\pi/2) \cosh(\gamma s)}{\pi \cos^2(\gamma\pi/2) + \sinh^2(\gamma s)}. \tag{2.73}$$

where α, β and γ are distribution parameters. A general case exists that describes both the Cole-Cole and Davidson-Cole relaxations (Fig. 2.9) known

as Havriliak-Negami relaxation [35].

2.3.1 Cole-Cole diagrams

Cole-Cole diagrams provide a visual representation of one or more relaxation process by plotting the real permittivity against the imaginary permittivity (Fig. 2.10). A perfect single frequency relaxation process will correspond to a circular arc with the centre positioned on the real permittivity axis. Often for molecularly large solutes and solutions the centre of this arc is found below the real permittivity axis and it was in fact this observation that lead Cole and Cole to propose their distribution (2.71), which when applied to (2.70) yields

$$\epsilon^*(\omega) = \epsilon_\infty + \frac{\epsilon_s - \epsilon_\infty}{1 + (i\omega\tau)^{(1-\alpha)}}. \tag{2.74}$$

It was also noted that the Cole-Cole plot appears skewed or asymmetrical in some cases. A distribution described by the Davidson-Cole function given as

$$\epsilon^*(\omega) = \epsilon_\infty + \frac{\epsilon_s - \epsilon_\infty}{(1 + i\omega\tau)^{\beta}}, \tag{2.75}$$

when (2.72) is inserted into (2.70). In the case of both an offset centre and a skewed arc the permittivity is given by the aforementioned HavriliakNegami equation,

$$\epsilon^*(\omega) = \epsilon_\infty + \frac{\epsilon_s - \epsilon_\infty}{(1 + (i\omega\tau)^{(1-\alpha)})^{\beta}}. \tag{2.76}$$

Cole-Cole and Cole-Davidson are most commonly applied to polymer systems.

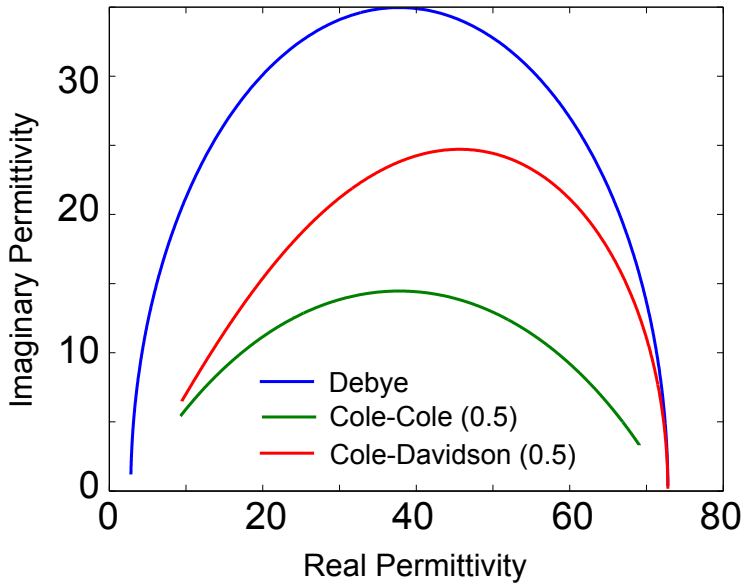


Figure 2.10: The real permittivity verses the imaginary permittivity comparing the response of a Cole-Cole ($\alpha = 0.5$), Cole-Davidson ($\beta = 0.5$) and a Debye model.

2.3.2 Permittivity and relaxation temperature dependence

As given by (2.24) and (2.35), the static permittivity of liquids containing molecules with permanent dipole moments is temperature dependent owing to increased temperatures yielding greater kinetic energy and therefore a greater chance to overcome the applied electric field.

In addition to the permittivity response being temperature dependent the relaxation time is also highly sensitive to the temperature owing to the diffusivity dependence on temperature as given in (2.57). This relationship was derived from Einstein's observations of the diffusivity of a spherical particle in a liquid ($D = \mu k_B T$) and expanded upon by Stokes by linking mobility to the viscosity of the liquid $\mu = 1/(6\pi\eta r)$. This was finally tied to the relaxation of a molecule by Debye leading us to the Stokes-Einstein-Debye relation [36, 37, 29] given as

$$\tau = \frac{r^2}{6\mu k_B T} = \frac{\pi\eta(T)r^3}{k_B T}. \tag{2.77}$$

This description demonstrates that the relaxation time not only depends on temperature but also viscosity that is in turn temperature dependent. The exact molecular mechanics behind the viscosity of various liquid mediums is somewhat poorly defined though generally can be expressed as the resistive force acting on the motion of a molecule. In this case it is the resistive force acting on the rotation of the molecule. For most common polar liquids (water, alcohols, acetone etc) the viscosity temperature dependence is described by an Arrhenius equation [38] (thermally activated) and therefore (2.77) becomes

$$\tau = \tau_0 \exp[E_\tau / k_B T], \tag{2.78}$$

where $\tau_0 = \pi r^3 \eta_0 / k_B T$ and E_τ the system activation energy (approx. 3.2 for pure water). The temperature dependence of each of the parameters in the Debye equation is shown in figure 2.11.

2.3.3 Electrolyte conductivity

The last important component of the dielectric response of liquids to consider is electrolytic conductivity. The response of an ion to an applied electric field is the acceleration in the relevant direction of the applied field. The conductivity of an electrolyte solution is therefore given as

$$\sigma = \sum_{k}^{N} \mu_k q_k C_k, \tag{2.79}$$

where N is the number of different ions present, μ the mobility of the ion, q the charge and C the concentration of ions. The mobility in a low Reynolds number system of viscosity η can be approximated to be

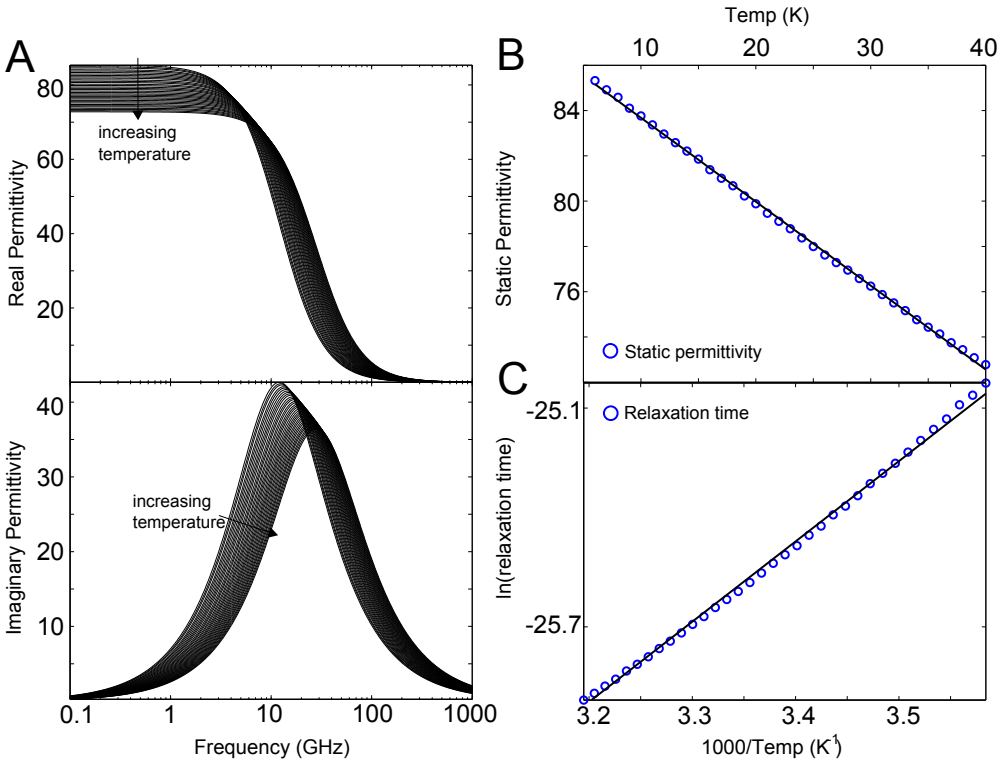


Figure 2.11: The temperature dependence of the real and imaginary permittivity of water around the relaxation frequency (A). The change in static permittivity as a function of temperature (B). An Arrhenius plot of relaxation time and inverse temperature (C).

$$\mu_q = \frac{1}{6\pi r\eta} = \frac{1}{6\pi r\eta_0}\exp(-E_\eta/k_BT), \tag{2.80}$$

where E_τ the system activation energy. The radius of the ion is r and again the viscosity is given as a thermally activated process. The concentration density has additional temperature dependence. The conductivity contribution from a single species of ion is

$$\sigma = \frac{qC}{6\pi r\eta_0}\exp(-E_\eta/k_BT). \tag{2.81}$$

2.4 Summary

The polarisation of solid and liquid materials in an electric field was theoretically examined and the concept of permittivity presented. The Clausius-Mossotti approach in explaining the static permittivity of a polar liquid was found to be inaccurate and therefore a second approach discussed, the Onsager model. Time-varying propagating electromagnetic fields were introduced and a materials time-domain response explored. The frequency dependent response of polar liquids led to the derivation of the Debye equation that characterises a polar liquids limiting response to a time-varying electric field. Semi-empirical variations of the Debye equation to account for complex systems with varying molecular dynamics were presented. The temperature dependence of the Debye equation was theoretically studied, in particular the relaxation time and lastly the electrolytic conductivity and relation to ion charge, radius and temperature.

Chapter 3

Microwave dielectric measurement techniques

The accurate measurement and deconvolution of the dielectric spectrum of polar solutions requires broadband frequency measurements across ranges as great as 1 MHz to 1 THz. Even with the most advanced equipment multiple measurement techniques are required to cover such a frequency range of which the most commonly used are described herein.

3.1 Waves at interfaces

Abrupt spatial changes of a materials permittivity or permeability has profound effects on electromagnetic propagation. The same is true for a wave confined to a transmission line that changes dimensions over a short distance. Consideration of such changes, however large or small, reveals the well defined Fresnel equations (Fig. 3.1). Considering the most general case of an interface we can take the relationship between the amplitude of the transmitted wave and reflected wave to be

$$t = 1 + r. \tag{3.1}$$

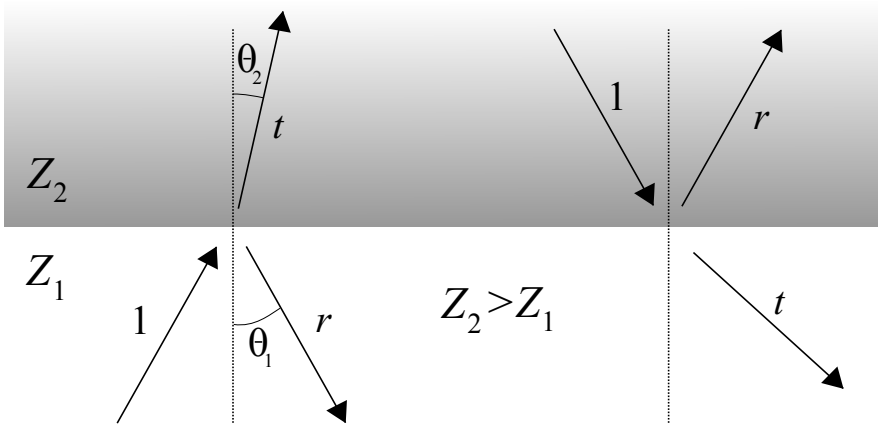


Figure 3.1: The reflection and transmission of an electromagnetic plane wave at an interface of two materials of different permittivities. $Z_{1,2}$ denote a material's characteristic impedance and r and t the reflected and transmitted amplitude of a plane wave as given in (3.1).

Note that the reflected wave amplitude may be positive or negative and therefore it is possible that the transmitted amplitude be greater than unity. Note also that a waves amplitude is dependent on the electromagnetic properties of the medium and therefore will not violate the law of energy conservation. The measurement of energy transfer across a boundary is a useful way to derive the reflection and transmission coefficients. A valuable parameter in measuring energy transfer is the wave impedance, Z, given as the ratio of the electric and magnetic field strength such that

$$Z = \frac{E}{H} = \sqrt{\frac{\mu}{\epsilon}}, \tag{3.2}$$

in the case of a free propagating plane wave in a material with permittivity ϵ and permeability μ. The relationship of impedance to energy is given in the Poynting vector $\mathbf{S}$ (energy flux density, Wm^{-2}) of a wave such that

$$\mathbf{S}^* = \frac{1}{2}(\mathbf{E} \times \mathbf{H}) = \frac{1}{2}(\mathbf{E} \times \frac{\mathbf{n} \times \mathbf{B}}{\mu}) = \frac{1}{2}(\mathbf{E} \times \frac{\mathbf{n} \times \mathbf{E}}{c\mu}) = \frac{1}{2Z}(\mathbf{E} \cdot \mathbf{E})\mathbf{n} \tag{3.3}$$

At an interface of two mediums the energy transfer is denoted by

$$Z_2 1^2 = Z_2 r^2 + Z_1 t^2. \tag{3.4}$$

By rearranging (3.4) and substituting (3.1) r and t are given as

$$r = \frac{Z_2 - Z_1}{Z_2 + Z_1}, \tag{3.5}$$

$$t = \frac{2Z_2}{Z_2 + Z_1}, \tag{3.6}$$

for a plane wave at normal incidence to the interface. In the case of waves propagating in a confined dimension such as in a transmission line the impedance takes a much more complex form, often highly dependent on the transmission line dimensions.

3.2 Vector Network Analyser

The vector network analyser (VNA) has become the standard tool and microwave source for component and circuit testing and material characterisation. Able to monitor both magnitude and phase information VNAs are well suited to signal transmission and reflection measurements, ideal for the purpose of dielectric characterisation.

Typical VNAs function with a two-port set-up with a built-in signal generator, receiver, processor and display (Fig. 3.2). More advanced devices operate with four ports and two signal generators though such devices are beyond the need of measurements conducted within this thesis. The built-in signal generator is a continuous wave (CW) source capable of covering a large frequency range. Many modern VNAs will typically cover ranges of 1 KHz to 3-10 GHz or 50 MHz to 20-67 GHz though extensions can provide a CW source up to 1 THz. The VNA functions with stepped frequency measurements such that

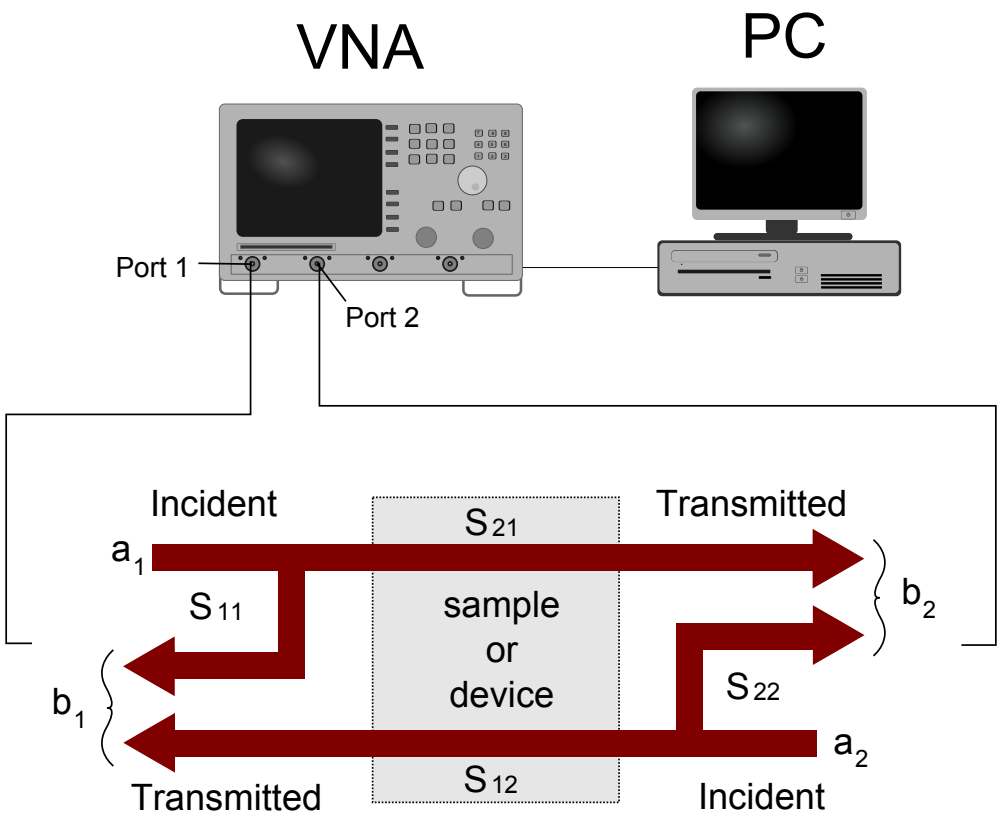


Figure 3.2: A vector network analyser with depicted transmission and reflection capabilities.

single frequency measurements are made before the frequency is increased and the measurement repeated. The receiver measures the magnitude and phase of the transmitted or reflect wave. In order to accurately ascertain the phase of the measurement signal a reference is split from the the source that is later combined with the measurement signal in a phase detector whose output is proportional to the phase difference. A typical measurement is made in terms of the S-parameters of a sweep where S_{11} and S_{21} are given as

$$S_{11} = \frac{\text{Reflected}}{\text{Incident}} = \frac{b_1}{a_1}, \tag{3.7}$$

and

$$S_{21} = \frac{\text{Transmitted}}{\text{Incident}} = \frac{b_2}{a_1}, \tag{3.8}$$

where the transmitted, reflected and incident measurements are made as a function of voltage (Fig. 3.2). The S_{11} is related to the reflection coefficient by

$$S_{11} = \frac{1 + |r|}{1 - |r|}, \tag{3.9}$$

where the reflection coefficient is given as

$$r = \frac{V_r}{V_f} = \frac{A \exp i(\phi + \delta)}{B \exp i(\phi)}, \tag{3.10}$$

and is the same as given in (3.6). A and B are the magnitude of the forward propagating and reflected wave and δ is the induced phase change of the reflected wave. For frequencies up to 70 GHz the source signal is carried in a coaxial cable to the device or sample under measurement. Above this frequency waveguides are used due to the complexity and tolerances involved in manufacturing coaxial cables small enough to support a fundamental mode above 70 GHz.

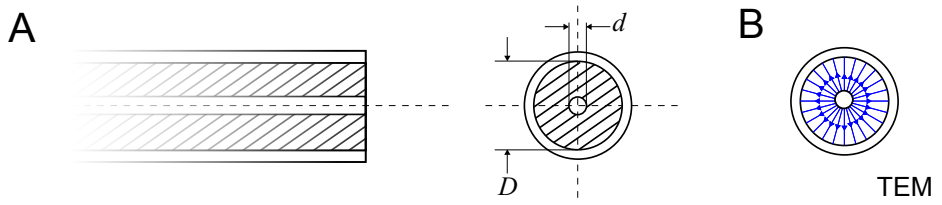


Figure 3.3: A cross-sectional depiction of a coaxial cable (A). The fundamental TEM mode of a coaxial cable (B).

Changes in the spatial dimensions, permittivity or permeability in the transmission line carrying the signal, in a device under measurement or a material will result in a change in the reflection and transmission of the signal and thus a change in the S_{11} and S_{21}.

Permittivity measurements and resonant techniques discussed within this thesis are made using an HP 8510 VNA with a frequency range of 50 MHz to 40 GHz.

3.3 Coaxial measurements

Dielectric measurements with coaxial cables for accurate high frequency spectroscopy have only been made possible in the last few decades owing to improved manufacturing techniques. For low frequency permittivity characterisation, coaxial cables become somewhat large and unwieldy and for higher frequencies coaxial cables require small dimensions to suppress higher order modes and maintain accuracy.

The coaxial cable comprises of a cylindrical inner and a tubular outer electrical conductor separated by a low-loss dielectric. The first advantage of using this type of transmission line is the confinement of the electric and magnetic field within the dielectric component of the cable thereby shielding the signal from external influence. The dimensions are held constant over the length of the cable thus maintaining a constant impedance for the propagating electromagnetic wave. The second notable advantage of coaxial cables is that they

can be engineered to be flexible and thus bent without any or little change in the phase of the propagating wave.

The properties of conducting interfaces instil boundary conditions on incident waves that, in the case of a coaxial cable waveguide confine the electromagnetic wave between the inner and outer conductor. These boundary conditions confine the type of wave that can be excited within the transmission line. Only one type of field distribution, the transverse electromagnetic (TEM) mode (no electric or magnetic field in the direction of propagation), can be excited and at any frequency within the coaxial cable. The field distribution of the mode is of a radial nature from the inner to outer conductor (Fig. 3.5). At high enough frequencies other defined modes exist such as transverse electric (TE) and transverse magnetic (TM) modes (see **resonant modes** below). Currents exist at the surface of the conductors though the wave does not propagate into the bulk of the material. It is preferential to maintain a single mode for all frequencies when making measurements of for communication to prevent unwanted interference and loss of information. To ensure single mode propagation the coaxial cable must suppress high order modes by operating at frequencies below the cut-off of the second mode (TE_{11} Fig. 3.5B/C) given by

$$f_c = \frac{c}{\pi \left(\frac{d+D}{2}\right) \sqrt{\epsilon\mu}}, \tag{3.11}$$

where d and D are the inner and outer diameters of other conductors, respectively. The characteristic impedance of a coaxial cable is given as

$$Z_0 = \frac{1}{2\pi}\sqrt{\frac{\mu}{\epsilon}} \ln \frac{D}{d}. \tag{3.12}$$

Coaxial material analysis is commonly carried out by reflection S_{11} measurements though there are established techniques for transmission measurements [39]. The cable is cleaved and polished to produce a smooth interface. Due to the large impedance miss-match between air and the coaxial cable, almost all of the wave is reflected back down the coaxial cable. The magnitude of

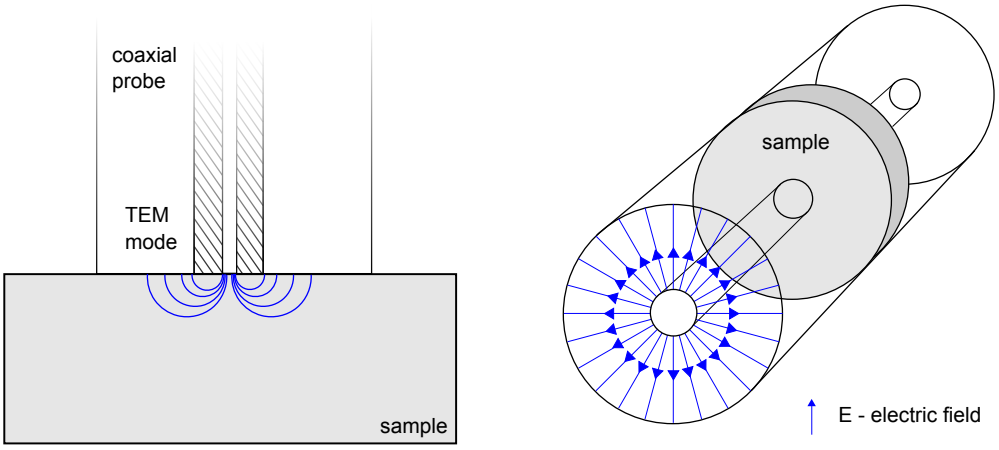


Figure 3.4: Dielectric measurements technique for bulk samples using a coaxial cable (A). Measurement of samples placed within the coaxial cable (B).

the reflected wave is dependent on the material interfaced with the coaxial cable.

Owing to the complex electric field distribution into the medium under measurement (fringe field) it is difficult to analytically solve the reflection coefficient for the permittivity of the medium being measured (Fig. 3.4B). A range of analytical solutions to this problem have been reported based on comprehensive studies using an equivalent circuit model outline in ref. [40].

3.3.1 Modelling, calibration, errors and permittivity calculations

Determining the dielectric properties of a material under measurement is most accurately achieved by first implementing finite element modelling to calculate the theoretical reflection coefficients and how they relate to a materials permittivity. The modelled response is implemented in post-measurement processing for the reverse calculation of the permittivity based upon the measured reflection coefficients.

A calibration serves to define a measurement reference plane by measuring the reflection coefficient of a number of materials with known dielectric properties at the probe-material interface across all frequencies used. Additionally the

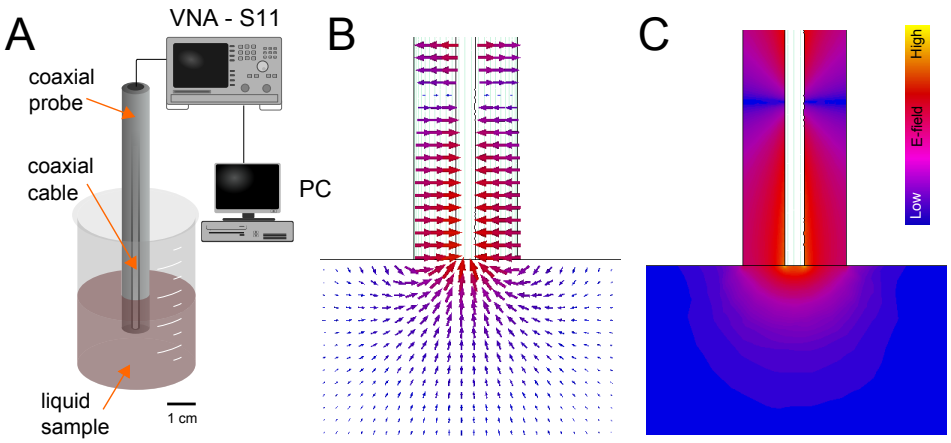


Figure 3.5: Experimental setup of the open-ended coaxial dielectric probe (A). The fundamental TEM mode of a coaxial cable visualising the electric field vector in the fringing fields (B). The electric field magnitude of the TEM mode and fringing fields (C).

calibration procedure removes effects of miss-matching via transmission line connection or defects prior to the probe-material measurement interface.

The first calibration for defining a reference phase and amplitude is a **short**-circuit where an infinite permittivity interface reflects all of the power at the probe-material interface with a 180 degree phase shift thereby giving a reflection coefficient of -1 (see (3.10), $\delta = \pi$). This calibration is conducted with a metal foil that is bought into contact with the open termination of the coaxial probe. A second calibration standard is an **open**-circuit where the material has a negligible permittivity and a high impedance of 376.6 Ω. The large imperdence miss-match leads to the reflected wave having no phase change and a resulting reflection coefficient of approximately 1. Another common calibration standard is a **matched**-circuit. The characteristic impedance of the transmission line is matched by the material and there is no reflected wave ($r = 0$). Owing to the smooth termination of the probe (coaxial cable) it is near-impossible to physically attached a matched load. A common replacement for such a calibration is a polar liquid with known complex permittivity. The use of a polar liquid proves to be a useful replacement to a matched calibration. By calibrating against permittivity values of a polar liquid the system is able to provide more accurate measurements on other

polar liquids.

Whilst the short-open-liquid calibration is simple to conduct there are a number of issues related to the calibration of an open-ended coaxial dielectric probe. The calibration involving the short requires the positioning of a smooth metal foil or block at the end of the probe whilst ensuring complete contact at all places. The second issue arises from the calibration standard of a known liquid. Such a calibration requires that the dielectric values are well documented across a range of temperatures and that the calibration temperature be accurately documented. For the calibrations conducted within this thesis deionised water (18 MΩ) at room temperature (approx. 293 K) was used for the calibration standard. Having calibrated the probe a second polar liquid (within this thesis - Methanol) is measured and the values compared to literature values to ensure a high quality calibration. The static permittivities must be within $\epsilon \pm 1.0$ else the calibration is repeated.

Errors may also arise from the permittivity calculation algorithm using S parameters owing to differences in the modelled probe dimensions and the manufactured geometries. Errors from surface roughness, certainly in commercial systems, are small in comparison to errors induced by the aforementioned issues. Methods for calculating the uncertainties in the permittivity calculation procedure are commonly done using Monte Carlo modelling [41].

There have been two commercial developments by Agilent and Speag of coaxial probes offering permittivity measurement capabilities between 50 MHz and 50 GHz. Broadband measurements conducted within this thesis use the Agilent performance probe kit and high temperature probe. Whilst the commercial probes offer fast measurements and minimal preparation there is little or no accessibility to the permittivity calculating algorithms or residual errors.

Based on the aforementioned uncertainties Agilent have quoted the absolute value accuracy of permittivity measurements conducted with the probe kit to be within $\epsilon' = \epsilon' \pm 0.05|\epsilon^*|$ and $\epsilon'' = \pm\epsilon'' \pm 0.05|\epsilon^*|$. This equates to approximately a 5 % uncertainty in the absolute values stated. Interestingly Gregory and Clarke demonstrated much lower error margins using a Monte

Carlo model concerning coaxial probes (including the Agilent 85070 temperature probe) and quoted uncertainties typically less than 1 %. Repeatability across different systems and between calibrations is given by Agilent to be within 1-2 % of the measured values. Our measurements found the repeatability between calibrations regarding the permittivity of water, ethanol and methanol to be within approximately 1.7 % of the absolute value at 20±0.1 K.

The errors associated with absolute values and the repeatability means that it is important to direct the development of analysis or biosensing techniques towards relative measurements and not absolute values.

A detailed study on measurement uncertainties in probe measurements by Gregory and Clarke has demonstrated that low frequency permittivity measurements become less accurate due to the reflection coefficient tending towards +1 +0i and thereby reducing sensitivity to the sample [41]. At low frequency (<0.5 GHz) the noise in the permittivity may be seen to become as large as $\epsilon^* = \epsilon^* \pm 0.5$. High frequencies are more prone to calibration errors as the smaller wavelength has a greater sensitivity to mechanical defects. Measurements by Gregory and Clarke have demonstrated a general increase in the residual calibration error when using a short calibration at higher frequencies (0.0005, 6 GHz) compared to lower frequencies (0.0001, 0.1 GHz) [41].

The cause of additional uncertainty and error from measurement techniques can arise from:

- sample size,
- temperature,
- air bubbles.

Consideration of sample size when undertaking measurements using a coaxial probe is important. Possible excitation of resonances within the sample, the additional reflections of the fringing fields or the fringing fields extending further than the sample dimensions are all potential by-products of a poorly chosen sample size. Careful selection of beaker size (liquids) or sample size

and shape is important to suppress resonances, avoid reflections and to confine the fringing field to the sample dimensions.

Temperature effects have been shown to be one of the largest contributions to measurement uncertainty [41] and variations between measurements. The importance of ensuring the sample is maintained within a ± 0.1 K environment is vital for performing accurate measurements. From figure 2.11 it may be shown that a 0.1 K variation in temperature is equivalent to a change in the permittivity of 0.04. Subsequently all measurements performed in the thesis were conducted in a temperature controlled laboratory (± 0.5 K) and the temperature of samples recorded to an accuracy of ± 0.05 K (absolute accuracy ± 0.5 K).

The requirement for the calibration liquid's temperature introduces an uncertainty of $\epsilon^* \pm 0.025$ to permittivity values (absolute value accuracy $\epsilon^* \pm 0.2$). The calibration liquid used in this thesis is water and subsequently measurements performed on samples with similar permittivities are assumed to carry the same uncertainty. Measurements conducted relative to a normalised sample (i.e. measuring the change in protein solution permittivity against the permittivity of water) effectively remove the uncertainty of calibration errors though an error due to the possible difference in temperature between measurement sample and the normalised sample exists (approx. 0.1 % change in permittivity). This is an important contribution to the uncertainty in the protein differentiation techniques highlighted in Chapter 5.

Thermal expansion of a coaxial probe such as the metal and dielectric core could result in a change to the phase difference especially in high frequency measurements. Subsequently materials with low thermal expansion coefficients are employed for the high temperature probe that are stable up to 470 K.

Ensuring the removal of bubbles from the probe-liquid interface is paramount to ensuring good accuracy. This is of particular importance for temperature dependent measurements. Two methods for the clearance of bubbles have been used. The first makes used of a malleable tool such as a clinically clean sponge that is wiped across the probe-liquid interface. This method is of

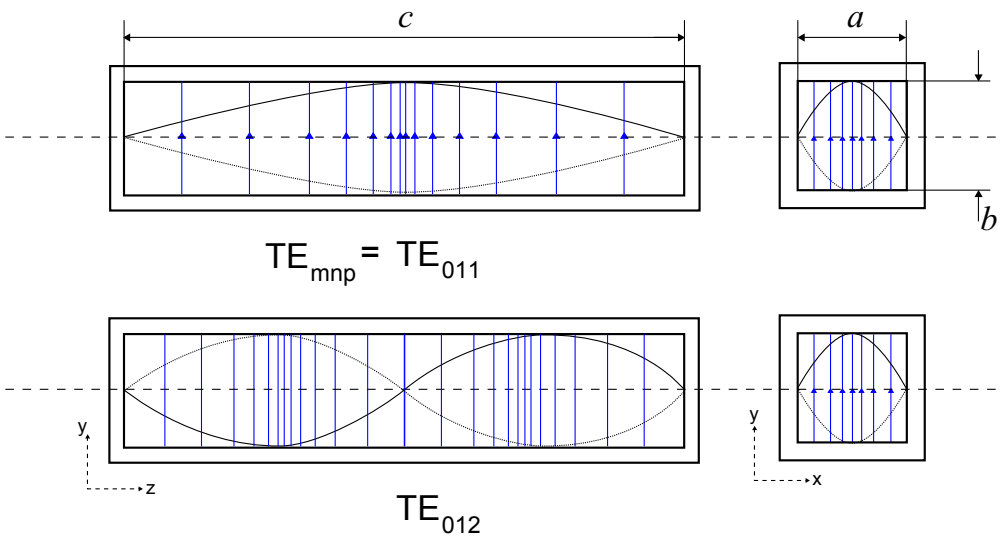


Figure 3.6: First and second order modes in a resonant cavity, $m = 1$, $n = 1$ and $p = 1, 2$.

particular use in solutions of high viscosity such as protein solutions. The second method uses large bubbles blown through a syringe positioned more than 20 mm from the probe tip to collect and remove other smaller bubbles from the interface. This has been implemented for temperature dependent measurements on salt solutions and water. Measurements are made within seconds of the probe tip being cleared. Uncertainties induced by bubbles are calculated based on the observed experimental data.

The measured complex permittivity is often deconvolved to obtain parameters (i.e. Debye equation - permittivity, relaxation time and conductivity). The accuracy of fits and the uncertainties of relevant parameters is covered in Chapter 4 - Fitting routines.

3.4 Resonators

A microwave resonator may be created in a number of geometries however all function on the same principle that the boundary conditions within the resonator lead to the reflected waves constructively interfering. Additionally, the material from which the resonator is constructed must have low enough losses

to ensure that the resonance is not over dampened. Possibly the simplest case of an electromagnetic resonance is that of a square waveguide short-circuited at either end and known as a cavity resonator (Fig. 3.6). The presence of conductive walls in multiple directions causes the formation of modes and when all three axis are confined this leads to discrete modes at stepped frequency intervals at which the boundary conditions allow for constructive interference. The permitted resonant frequencies are therefore given as

$$k_{res}^2 = \left(\frac{\omega}{c}\right)^2 = \left(\frac{m\pi}{a}\right)^2 + \left(\frac{n\pi}{b}\right)^2 + \left(\frac{p\pi}{c}\right)^2, \tag{3.13}$$

where a, b and c are the dimensions of the cavity and m, n and p the mode number. Visual solutions for $p = 1$ and $p = 2$ can be seen in figure 3.6. In the case of a cylindrical cavity resonator the allowed modes are somewhat more complex but can be solved using Bessel functions. The resonant wavevectors of a cylindrical resonator are

$$k_{res}^2 = \left(\frac{X_{r\theta}}{r}\right)^2 + \left(\frac{p\pi}{c}\right)^2, \tag{3.14}$$

where c is the cylindrical cavity height and $X_{r\theta}$ the solution to the Bessel function of mode numbers r and θ.

When comparing resonances the quality of a resonance can be considered to be the ratio of total energy stored in the system at any given time (W_J) and energy lost per cycle (P_τ/ω). The dimensionless parameter known as the quality factor Q denotes such a ratio such that

$$Q = \frac{2\omega W_J}{P_\tau}. \tag{3.15}$$

The Q can also be used to denote the number of cycles the resonant standing wave would complete before the amplitude drops to 1/e. In a system with loss the standing wave time-dependent response of the wave is

$$\mathbf{E}(t) = \mathbf{E_0} \exp(-\gamma t) \exp(-i\omega t), \tag{3.16}$$

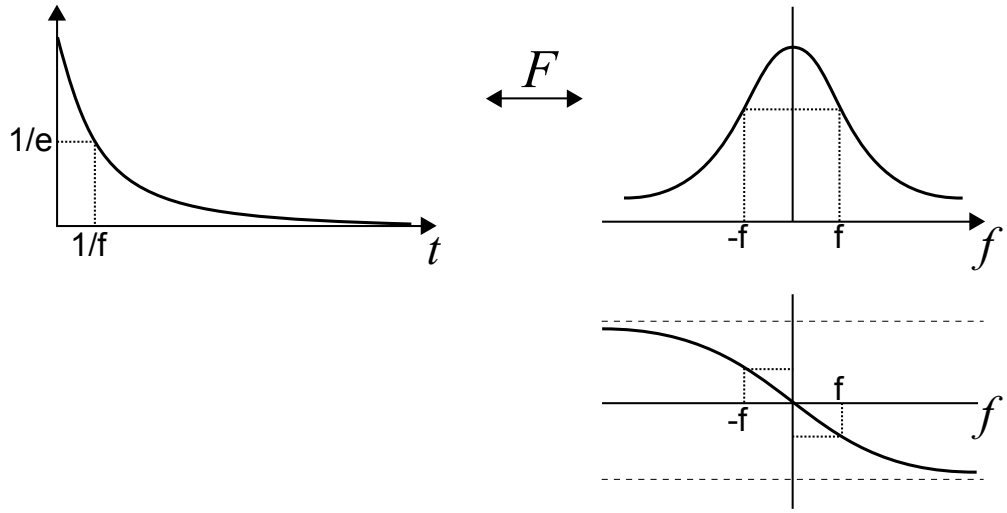


Figure 3.7: The Fourier transform between the time domain response of a resonance and frequency. The LHS shows the time-domain response of dampend resonance and the RHS the magnitude and phase response with respect to frequency.

where γ relates to the energy lost per cycle. The frequency response is calculated from the Fourier transform of the time domain and the result is a Lorentzian distribution around ω

$$\exp(-\gamma t)u(t) \overset{F}{\longleftrightarrow} \frac{1}{\gamma - i\omega}, \tag{3.17}$$

where F denotes the Fourier transform operation (Fig. 3.7). The frequency distribution is seen in almost all resonant systems and many fitting routines make use of the Lorentzian curve distribution. Transmission measurements across a resonator are visualised in the S_{21} and are seen to display a Lorentzian distribution. At high Qs where the half-width-max of the resonance is much less than the resonant frequency the quality factor can be given to be

$$Q = \frac{f_0}{\Delta f}, \tag{3.18}$$

where Δf is the bandwidth of the resonance at half of the maximum value at the resonant frequency f_0 (Fig. 3.8).

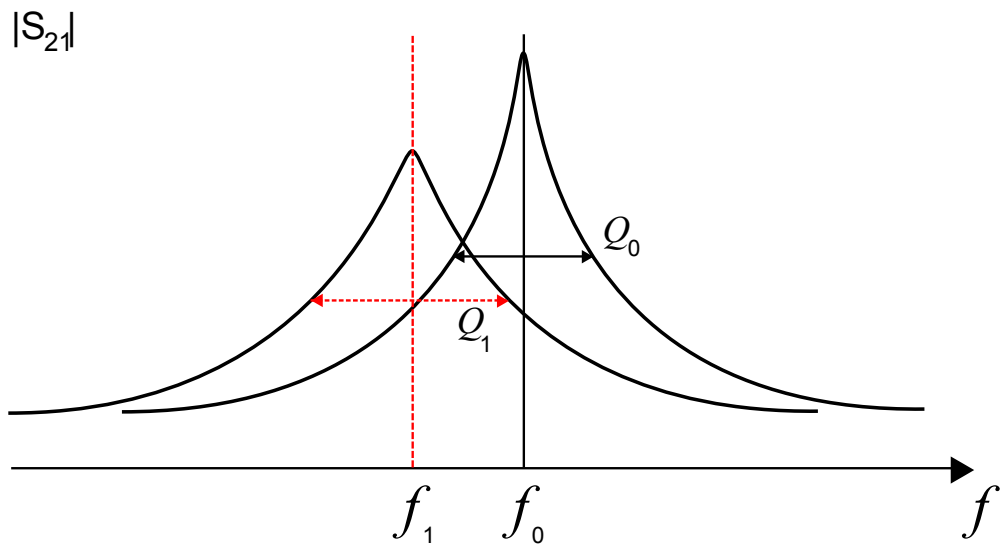


Figure 3.8: The resonant frequency and bandwidth of two resonant curves as a function of frequency.

3.4.1 Dielectric resonators

Unlike a cavity resonator that relies on constructive interference built up in a reflective metal cavity, the resonant properties of a dielectric resonator may outperform a cavity resonance owing to high field confinement in a low-loss, high permittivity ceramic. Using a high permittivity resonator in a low permittivity environment results in the large reflection coefficients that lead to high field confinement within the resonator. The absence of metal interfaces reduces the losses induced in the reflection, however, the electric and magnetic field are non-zero at the boundary of the resonator and surrounding environment. There are consequently three field components to consider within a resonator; the field within the resonator, the evanescent fields outside of the resonator (see Evanescent fields below) and radiative fields. In the case of a cylindrical dielectric resonator that is operated at its fundamental TE_{01} mode the electric field, though predominantly confined to the cylindrical resonator also has field lines outside of the resonator that decay exponentially as a function of distance from the resonator (Fig. 3.9). Such a mode will also radiate with the resonator acting as an antenna. The field distribution in a resonator is highly dependent on the mode number with each having a specific ratio of confined, radiative and evanescent components. At high fre-

quencies solutions appear that are known as whispering gallery modes (Fig. 3.9F and 3.10F). At these frequencies the wavelength of the electromagnetic wave is often significantly smaller than the resonator. A whispering gallery mode arises from the wave inside the resonator unable to escape the high permittivity due to an angle of incidence with the interface that is greater than the critical angle and so is total internally reflected. These modes are highly confined with very low radiative components and high evanescent field components. For lower order azimuthal modes the radiative components can be suppressed by housing the dielectric resonator in a metal cavity thereby increasing the total energy within the resonator and thus the Q-factor. This latter technique is chosen for the measurements conducted within this thesis and shall be the focus of further discussion.

Though resonator techniques have found a range of applications in research environments there are only a few examples of microwave techniques extending to commercial settings such as communication filters [42, 43], material analysis [44] and security [19].

3.4.2 Manufacture

Dielectric resonators are most commonly manufactured from high permittivity, low-loss and temperature stable ceramics such as barium zirconate titonate (BZT). Low levels of inhomogeneity in the manufacture of a resonator is key to ensuring low-losses. Similarly the purity and consistency of the crystalline structure has been shown to be vital to ensuring a high permittivity [45]. The high dielectric constant is attributed to ionic displacement polarisation as discuss in the first instance in chapter 2 concerning the Clausius-Mossotti equation. Though low-loss in the microwave regime this mechanism is typically associated with low permittivities (i.e. NaCl), however, titanium dioxide and related titanium compounds have been found to create high permittivity whilst maintaining low losses [46]. To achieve high purity and homogeneity the production of high permittivity ceramics is predominantly achieved via sintering, the heating of a compressed powder to a temperature below its melting point leading to atomic diffusion between

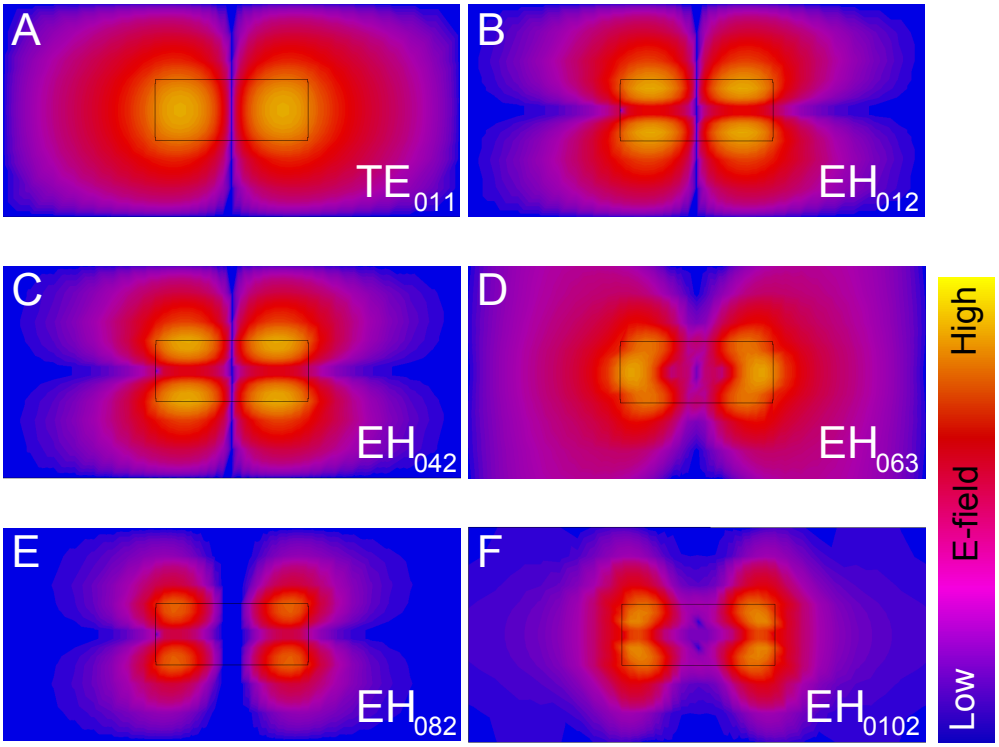


Figure 3.9: The vertical cross-section of the electric field distribution of a cylindrical dielectric resonator within a cylindrical metal cavity. The black rectangular line denotes the boundaries of the dielectric resonator. The numerical sub-text relates to the radial, azimuthal and vertical mode numbers. The TE_{011} mode is the fundamental dielectric mode with electric field lines only in the horizontal plane (A). Other sub-figures display resonant modes (B-F) where the modal number causes a large change to the electric field distribution. Cross-sections of the horizontal plane of the respective modes are shown in figure 3.10.

powder molecules and subsequent binding of the material.

3.4.3 Resonant modes

As discussed with cavity resonators discrete resonant frequencies exist at which the boundary conditions of the system favour constructive inference. The non-zero boundary conditions of the fields lead to complex analytical solutions to derive the resonant modes and frequencies. Four types of mode can be excited within a dielectric resonator each relating to the distribution

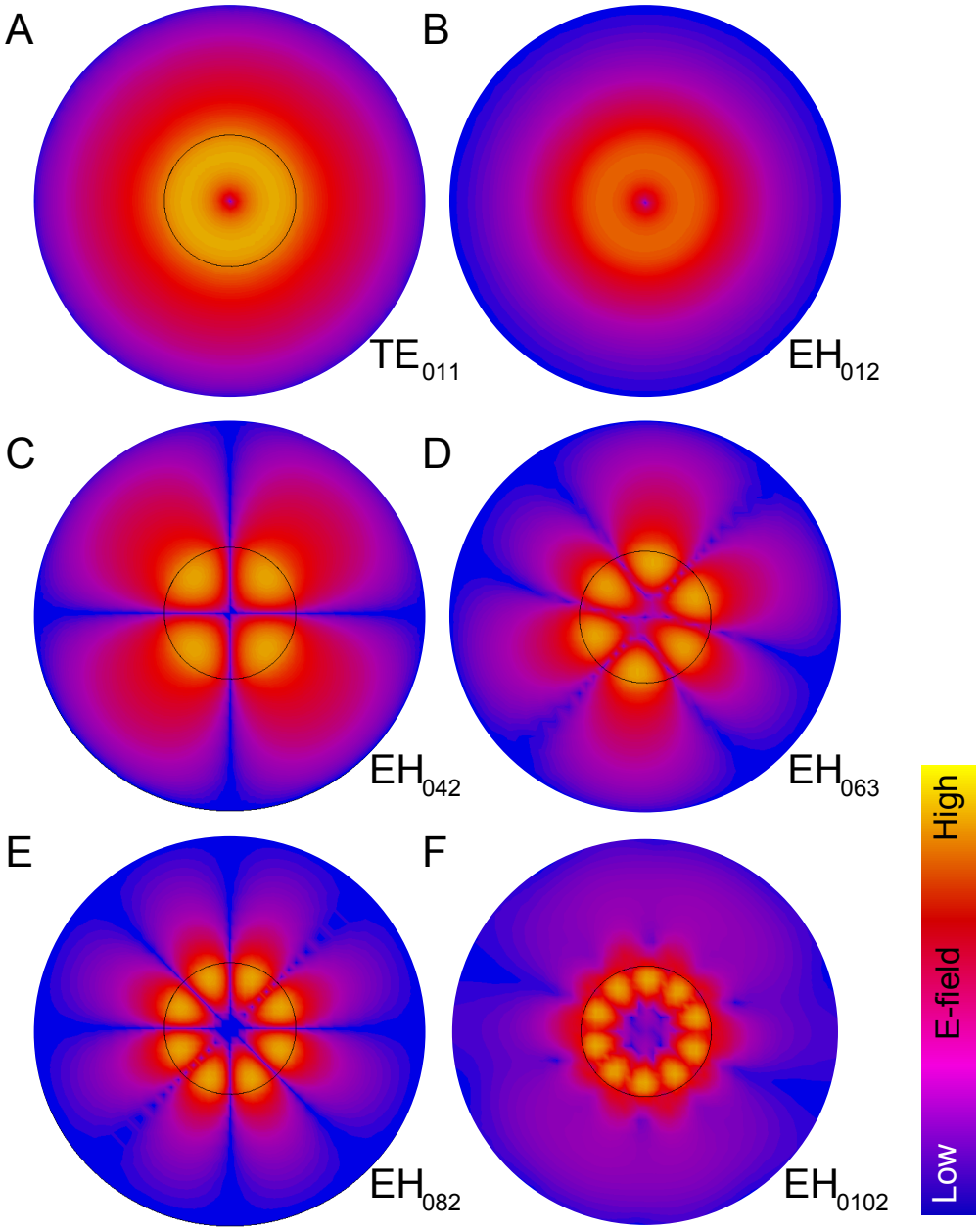


Figure 3.10: The horizontal cross-section of the electric field distribution of a cylindrical dielectric resonator within a cylindrical metal cavity. The black cylindrical line denotes the boundary of the dielectric resonator. The numerical sub-text relates to the radial, azimuthal and vertical mode numbers. The TE_{011} mode is the fundamental dielectric mode with electric field lines present only in-plane (A). Other sub-figures display resonant modes (B-F) where the modal number causes a large change to the electric field distribution. As the modes (and frequency) become higher order (whispering gallery) the electric field confinement to the resonator increases.

of the electric and magnetic fields within.

- $\mathbf{TE}_{r\theta z}$ - Transverse electric. No electric field component acts in the vertical plane (resonator) or direction of propagation (transmission line). r, θ, z are the radial, azimuthal and vertical mode number of the resonance.

- $\mathbf{TM}_{r\theta z}$ - Transverse magnetic. No magnetic field component acts in the vertical plane (resonator) or direction of propagation (transmission line). (Fig. 3.11A)

- $\mathbf{EH}_{r\theta z}$ - Electric dominant hybrid. Electric and magnetic field in all planes. (Fig. 3.11B)

- $\mathbf{HE}_{r\theta z}$ - Magnetic dominant hybrid. Electric and magnetic field in all planes.

The development of modern computational systems has provided the means to model highly complex systems to determine their electromagnetic response [47, 48]. Used for resonant systems they can solve for modes, field distributions with amplitude and phase, resonant frequencies and Q-factors. Depicted in figures 3.9 and 3.10 are the electric field distributions of a number of modes from the fundamental TE_{01} mode (Fig. 3.9A and 3.10A) to a $\theta = 10$ whispering-gallery mode. The choice of a mode is highly dependent on the role the system is to play. The simple field distribution of a TE_{01} mode makes it well suited for dielectric measurements however in an open system a higher order mode may prevail as a result of the low radiative component. Matching a mode to the sample location maximizes field-sample interaction such as a fundamental mode to a sample volume within the resonator, a whispering gallery mode for measurement on the outer edge of the resonator and a second or third order z mode for enhanced electric fields for measurements at a surface.

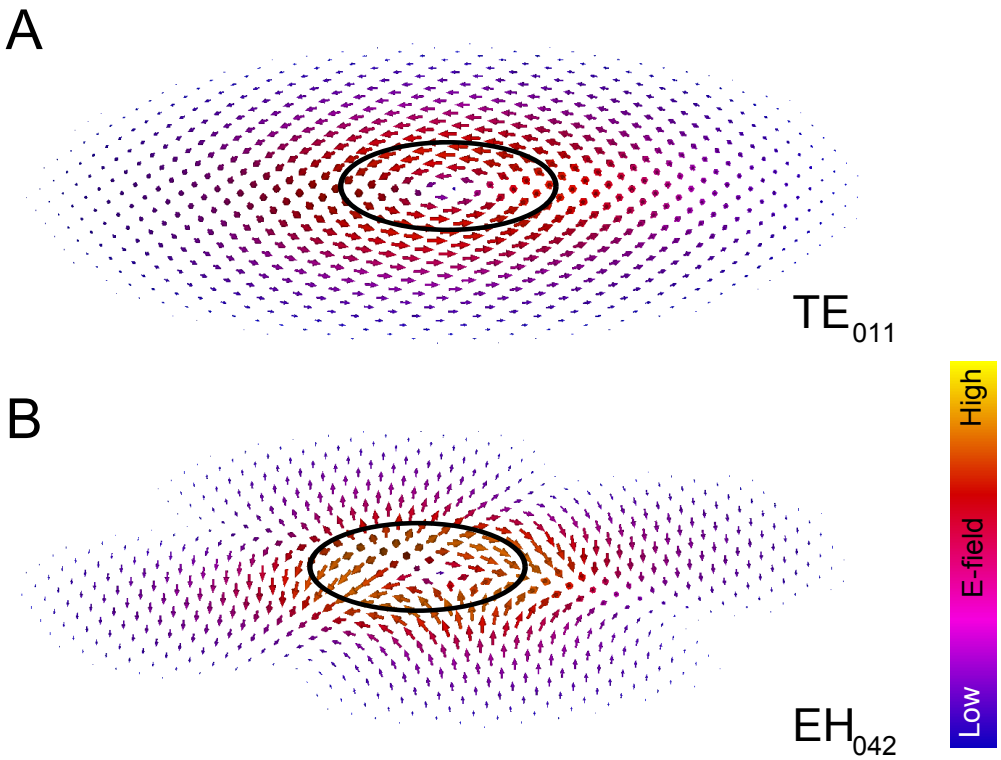


Figure 3.11: Horizontal cross-section of the electric field vector distribution of a cylindrical dielectric resonator within a cylindrical metal cavity. As described the fundamental TE_{011} mode has field lines only in the horizontal plane (A). For higher order modes such as the EH_{042} electric field lines are present in all directions however the electric field is dominant in the horizontal plane (B).

3.4.4 Quality factor

The quality factor of a system has been discussed in brief for a system with losses (see introduction Resonators above). Based on (3.15) a detailed description of how the Q of a dielectric resonator can be related to the material and dimensions of the resonator is discussed.

Considering the case of a dielectric resonator of complex permittivity ϵ^* the Q factor according to (3.15) is related to the total energy of the system in addition to the energy lost per cycle. The total energy stored within the system is given by

$$W = \int_{V_{res}} \mathbf{E_0} \cdot \mathbf{D_0} dV + \int_{V_{cav}} {\mathbf{E_0}}^2 dV = (\epsilon') \int_{V_{res}} {\mathbf{E_0}}^2 dV + \int_{V_{cav}} {\mathbf{E_0}}^2 dV, \quad (3.19)$$

for a system with only dielectric properties. The energy lost per cycle is calculated by

$$P = \omega \epsilon'' \int_{V_{res}} {\mathbf{E_0}}^2 dV, \quad (3.20)$$

Losses from the metallic boundaries of the cavity must also be considered assuming the evanescent fields have not negligibly decayed. The resulting Q of the system is

$$Q = \left[\frac{\epsilon'}{\epsilon''} + \frac{\epsilon'' \int_{V_{res}} {\mathbf{E_0}}^2 dV}{\int_{V_{cav}} {\mathbf{E_0}}^2 dV} + \frac{1}{Q_{cond}} \right]^{-1} = \left[\tan \delta^{-1} + \frac{1}{Q_c av} + \frac{1}{Q} \right]^{-1}. \quad (3.21)$$

Assuming that the losses from the conductive boundaries are small the power lost per cycle is

$$P_\tau = \frac{R}{2} \int_{S_{walls}} H^2 dS, \quad (3.22)$$

where $R = \sqrt{\omega\mu_0/2\sigma}$ (sheet resistance) and where the integration is made over all surfaces [49].

3.4.5 Evanescent fields

The previously considered case of reflection and transmission coefficients dealt only with a wave approaching normal to the material interface. If the the wave approaches from an angle then (3.6) can be expressed for s- and p-polarised light as

$$r_s = \frac{Z_2 \cos\theta_1 - Z_1 \cos\theta_2}{Z_2 \cos\theta_1 + Z_1 \cos\theta_2}, \tag{3.23}$$

$$r_p = \frac{Z_2 \cos\theta_2 - Z_1 \cos\theta_1}{Z_2 \cos\theta_2 + Z_1 \cos\theta_1}. \tag{3.24}$$

One can recognise that reflection tends to 1 as $\theta_2 > \theta_{crit}$ for $\epsilon_2 < \epsilon_1$. Within this condition an interesting phenomena occurs, related directly to the continuity requirement of the electric and magnetic fields at a boundary. An exponentially decaying electric field component that transmits no power decays into the transmission region of the boundary. To realise this, consider the transmission wavevector at a boundary between two dielectric mediums, $\mathbf{k}_t = k_t(\sin\theta_t\hat{\mathbf{x}} + \cos\theta_t\hat{\mathbf{z}})$. From Snell's law one can state

$$\sin\theta_t = \frac{\sqrt{\epsilon_1}}{\sqrt{\epsilon_2}} \sin\theta_i, \tag{3.25}$$

and thus with $\sqrt{\epsilon_2} < \sqrt{\epsilon_1}$

$$\cos\theta_t = \sqrt{1 - \sin^2\theta_t}, \tag{3.26}$$

$$\cos\theta_t = i\sqrt{\sin^2\theta_t - 1}. \tag{3.27}$$

The wavevector can now be define as

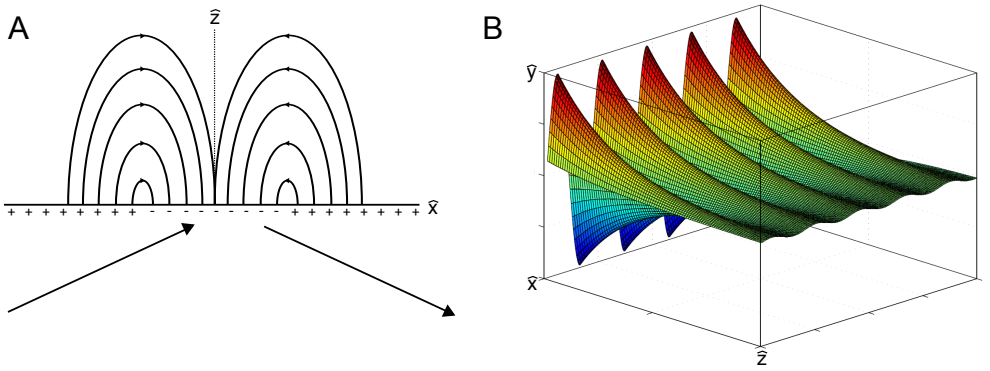


Figure 3.12: The electric field distribution at an interface between a high permittivity and low permittivity material with the incident wave past the critical angle. A totally internally reflected wave may transfer no energy into the second medium however the polarisation of the first material at the interface leads to the presence of a non-propagating electric field in the second medium (A). A cross-section of the second medium shows the electric field intensity as a function of distance from the interface (**z**) and as a function of the length (**x**) of the interface (B).

$$\mathbf{k}_t = \frac{k_t}{n_t}\left(\alpha\hat{\mathbf{x}} + K\hat{\mathbf{z}}\right), \tag{3.28}$$

where $\alpha = n_i \sin\theta_i$ and $K = i\sqrt{(n_i \sin\theta_i)^2 - n_i^2}$. Applied to a wave solution at a single point in time the electric field under total internal reflection in the transmission region becomes

$$E = E_0 \exp(-\alpha z)\exp(iKx), \tag{3.29}$$

as shown in figure 3.12. Though non-propagating and non-transmitting the evanescent wave still comprises of a real electric field and is therefore highly sensitive to local changes in the dielectric constant.

3.4.6 Dielectric measurement and perturbation theory

The dielectric measurement samples by resonator technique is advantageous when the material in question is only present in small volumes ($V_{sample} <<$

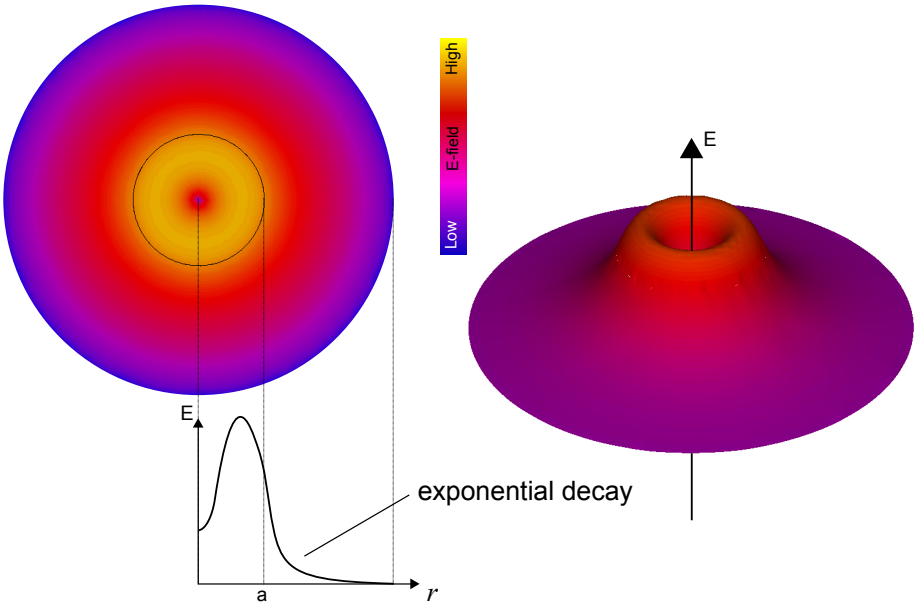


Figure 3.13: The electric field distribution inside and outside a cylindrical dielectric resonator.

V_{res}). High Q resonators provide accurate and stable measurements of which the most common are built upon a cavity [50, 51], re-entrant [52, 53, 54] or dielectric [55, 56, 57, 58] designs. In order to accurately measure the permittivity of the sample under measurement an analytical model must be constructed to allow for the deconvolution of data. Typically the resonant frequency and Q are recorded with and without the sample present and the relative change related to the real and imaginary permittivity, respectively [59]. A detailed analytical derivation reporting the change in resonant parameters in a resonator induced by a sample of relative permittivity ϵ_r may be found in [60] as well as a review of the accuracy of such an approach in [61]. Whilst this model, known as perturbation theory, was constructed with cavity resonators in mind, it has been shown that it is sufficient for the description of sample measurement with dielectric resonators [55, 56]. Considering a resonant perturbation in its simplest case the electric and magnetic field in an unperturbed resonator at resonant angular frequency ω are given as

$$\mathbf{E} = \mathbf{E_0} \exp(i\omega t), \tag{3.30}$$

and

$$\mathbf{H} = \mathbf{H_0} \exp(i\omega t). \tag{3.31}$$

Considering the same resonator with a sample present results in a change to the fields such that

$$\mathbf{E'} = \mathbf{E_1} \exp(i(\omega + \delta\omega)t), \tag{3.32}$$

and

$$\mathbf{H'} = \mathbf{H_1} \exp(i(\omega + \delta\omega)t, \tag{3.33}$$

where $\delta\omega$ is complex. The resulting ratio between the resonant frequency and the induced change to the complex frequency is given according to the change in energy stored against the total system energy such that

$$\left| \frac{\Delta\omega^*}{\omega} \right| = \frac{\int_{V_l} \left[(\mathbf{E_1} \cdot \mathbf{D_0} - \mathbf{E_0} \cdot \mathbf{D_1}) - (\mathbf{H_1} \cdot \mathbf{B_0} - \mathbf{H_0} \cdot \mathbf{B_1}) \right] dV}{\int_V (\mathbf{E_0} \cdot \mathbf{D_0} + \mathbf{H_0} \cdot \mathbf{B_1}) dV}, \tag{3.34}$$

where the numerator need only be integrated over the volume of the perturbing volume V_l as the rest of the volume would be unchanged. The right hand side of (3.34) may be thought of as the ratio of the change in energy stored in the sample volume to the total energy in the resonator. It is possible for this equation to be applied to any system that is perturbed by an object with any permittivity or size. It is however hard to apply (3.34) to many real systems due to the difficulty in knowing the electric and magnetic field within the perturbed system. If the material is homogeneous and isotropic and the field distribution remains unchanged within the sample then (2.12) and (2.47) can be applied to (3.34) and in the case of the material also possessing no ferroelectric properties then (3.34) may be reduced to [62]

$$\frac{\Delta\omega}{\omega} + i\frac{1}{2}\Delta\left(\frac{1}{Q}\right) = \frac{1}{4W} \int_V (\mathbf{E_1} \cdot \mathbf{D_0} - \mathbf{E_0} \cdot \mathbf{D_1}) dV, \tag{3.35}$$

where W is the energy stored in the resonator. The real component of (3.34) becomes

$$\frac{\Delta\omega}{\omega} = \frac{\epsilon_0(\epsilon_r' - 1)}{4W} \int_V \mathbf{E_0}^2 dV, \tag{3.36}$$

and the imaginary,

$$\Delta\left(\frac{1}{Q}\right) = \frac{\epsilon_0\epsilon_r''}{2W} \int_V \mathbf{E_0}^2 dV, \tag{3.37}$$

where ϵ_r' and ϵ_r'' are the real and imaginary components of the relative permittivity. (3.36) and (3.37) can be expected to remain a valid analytical tool for permittivity analysis for modes such as the fundamental TE_{01}. Issues arise with high order modes or complex resonators owing to the requirement of an analytical solution to $\mathbf{E_0}$ in (3.36) and (3.37). Additionally the scalar product of the electric fields $\mathbf{E_0} \cdot \mathbf{E_1}$ may be highly complex and only exasperated by high permittivity samples or of increased size. A semi-empirical approach to solving (3.35) has been reported for complex resonant systems and high permittivity samples in ref. [63].

3.4.7 Coupling

The excitation of a microwave cavity resonator can be achieved in a number of ways though the most common are coupling loop and aperture methods (Fig. 3.14). Typical systems make use of two coupling components, the first for the excitation and the second for the measurement. Coupling loops short circuit the inner and outer conductor on a coaxial cable which at any given time will be polarised with opposite charge. The potential difference induces a current through the loop which in turn creates a magnetic field that curls around the loop (Fig. 3.14D). The magnetic field then excites any number of modes depending on its orientation within the cavity. An aperture is commonly used with a waveguide and is a sub-wavelength slit in a conductive wall with a cutoff frequency above the propagating wave frequency that leads to an evanescent coupling into the cavity. Though useful for cavity resonator excitation coupling into a high permittivity dielectric resonator is likely to be low. Coupling loops prove far more advantageous for exciting dielectric

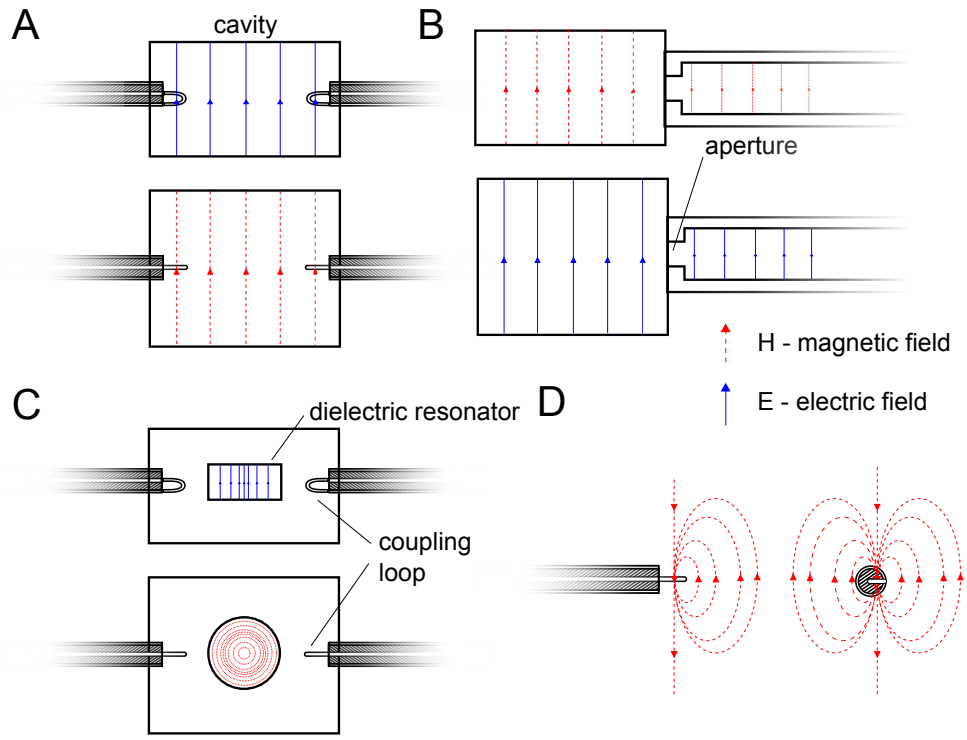


Figure 3.14: The electric and magnetic field excited by coupling loops in a resonant cavity (A). Aperture excitation of a cavity mode (B). Field excitation of a dielectric resonator by coupling loops (C). The magnetic field distribution of a coupling loop (D).

resonators due to the ability to excite an electric field inside the dielectric puck via the magnetic fields created by the loop. Positioning and orientation of the coupling method is important for ensuring optimum coupling coefficients and excitation of the correct mode.

3.4.8 Loaded Q

The Q factor of a system as discussed previously depends heavily on the losses in the system. Implementing coupling loops can be thought of as being synonymous with system losses as energy within the resonator is being lost to the coupling device (P_{cpl}). As such the loaded Q becomes

$$Q = \frac{2\omega W}{P_{cav} + P_{cpl}} = \left[\frac{1}{Q_{res}} + \frac{1}{Q_{cpl}}\right]^{-1}. \tag{3.38}$$

Additionally, the coupling loop provides the driving frequency and energy. It is subsequently important to optimise the coupling to both couple energy in and out of the system. A valuable means of estimating the effectiveness of the coupling is the coupling coefficient g where

$$g = \frac{Q_{res}}{Q_{cpl}}. \tag{3.39}$$

Consequently the loaded Q can be defined by the unloaded Q (Q_{res}) and coupling coefficient such that

$$Q = \frac{Q_{res}}{1 + g}. \tag{3.40}$$

For the excitation of the resonance the coupling loop would ideally couple all energy into the resonance. Values of g below 1 are referred to as under coupled, above as over coupled and $g = 1$ as critically coupled. The coupling coefficient is related to the reflection coefficient such that

$$r = \frac{g-1}{g+1}, \tag{3.41}$$

showing that at critical coupling all energy is transferred to the resonant system at the resonant frequency. For the read-out or transmission measurements under-coupling is desirable so as to ensure minimal energy is removed from the system.

3.5 Time domain spectrometers

Unlike frequency domain spectroscopy such as that carried out by a VNA, time domain spectrometry (TDS) carries out spectroscopy as a function of time. Measuring both the amplitude and phase of the electric field of the wave TDS yields broadband frequency domain measurements by carrying out a Fourier transform of the measured time domain response. TDS methods have been employed for over two decades in the THz regime (0.1-20 THz) since the discovery of a valid THz source [64] and have been used for a wide range of material measurements and imaging systems [65]. A major advantage of TDS is the short time pulse of the measurement allowing for the gating of unwanted reflections. Additionally, all frequencies are contained within a single pulse and therefore unlike the VNA which requires a measurement at each frequency TDS simultaneously measures all source frequencies. Excitation of a THz-TDS source is carried out by photoconduction in a semiconductor such as gallium arsenide excited by a pulsed infrared laser. To time gate the response of the measurement the laser beam is split into a probe and pump beam. The source is excited by the pump beam and the signal measured by a detector excited by the probe source thereby giving the detector the same time window as the source (Fig. 3.15). For the single measurement conducted within this thesis a commercial TeraView TPS 3000 is implemented covering a frequency range of 60 GHz to 4 THz.

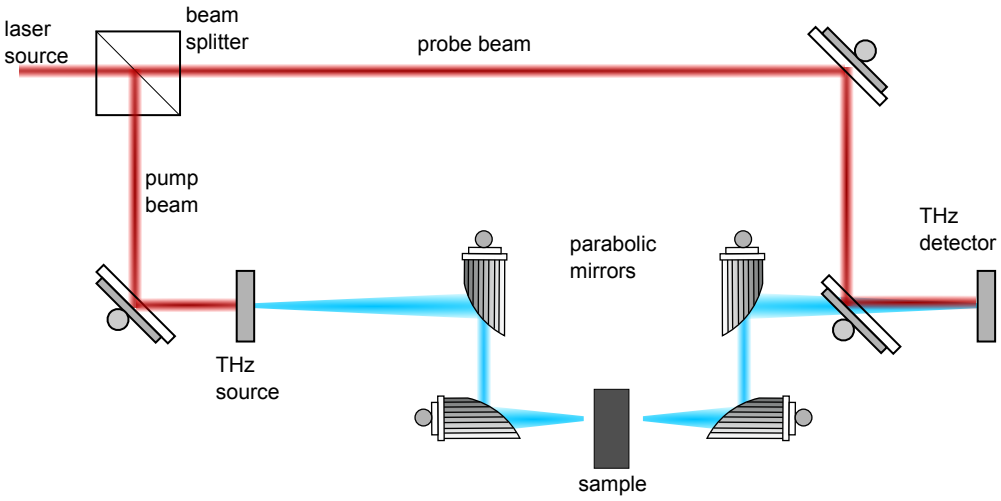


Figure 3.15: A schematic outlining the path taken for the probe and pump beam and subsequent excitation and focusing of the THz beam.

3.6 Summary

Three experimental techniques for microwave permittivity characterisation have been presented; coaxial and resonant methods as well as quasi-optical TDS. THz-TDS provides fast and relatively accurate frequency dependent dielectric material characterisation between 100 GHz and 4 THz. The accuracy and traceability of coaxial probes prove useful for dielectric measurements from single MHz up to approximately 50 GHz though require calibration against known standards. The ability to conduct contact mode measurements and the broad frequency range of a coaxial cable make it well suited to dielectric measurements of liquids. Resonant techniques provide accurate single frequency measurements on small sample volumes of low permittivity. The fundamental properties of electromagnetic resonators were explored and the properties of modes examined. Additionally the relationship between the resonant parameters (Q and f) and the internal and external dielectric properties was characterised. Microwave resonant measurements can be conducted on very small sample volumes and can even be utilised for dielectric measurements in certain configurations.

Chapter 4

Dielectric properties of polar solutions and electrolytes

To begin understanding and developing analysis methods of organic or biological solutions a study into the response of the simplest constituent (polar liquids) should be made to highlight and confirm the mechanisms and processes described in Chapter 2.

The abundance of electrolytes in organic and biological solutions make them an important solute to investigate. Comprehending the dielectric influence of the simplest building blocks in a complex solution allows for a more accurate understanding of the heterogeneous features of biological solutes such as proteins.

4.1 Polar liquids

The dielectric response of dipole moments in a liquid phase has been discussed in some depth in Chapter 2 though the detailed response of real polar liquids remains to be explored. The complex permittivity of many common liquids vary by large amounts due to the range of molecular sizes, intermolecular spacings and variations in the strength and density of dipole moments.

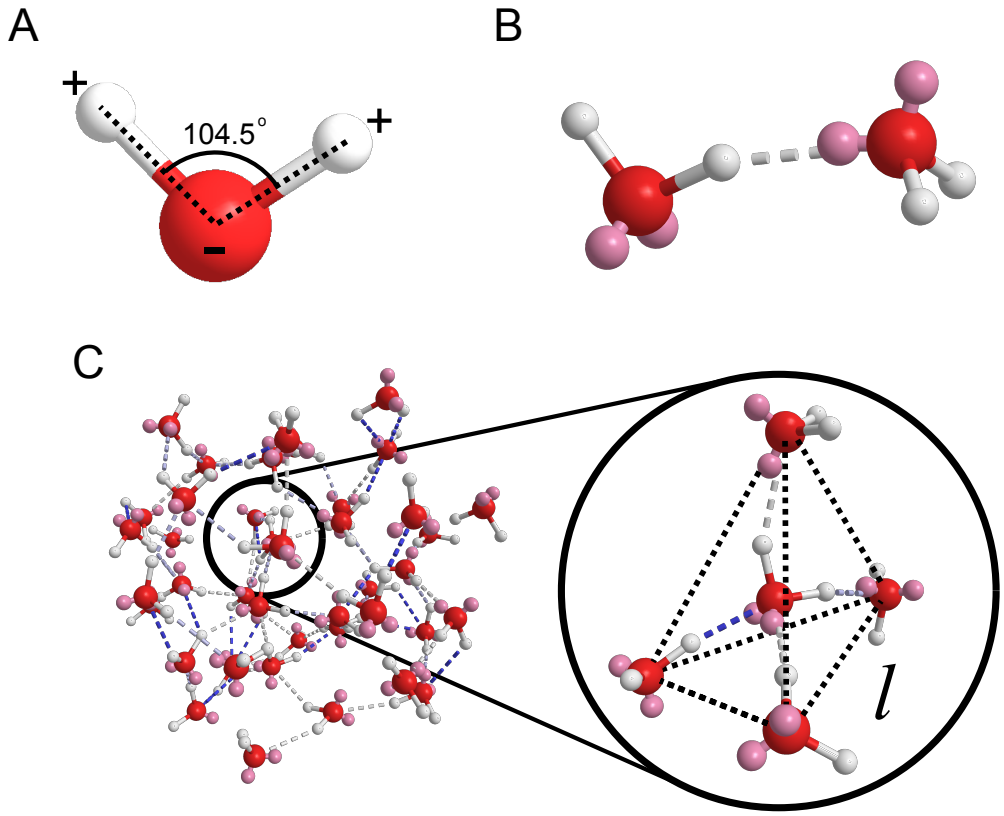


Figure 4.1: The structure of a water molecule (A). The common intermolecular hydrogen bonding between two water molecules (B). A lattice of water molecules modelled in ChemDraw Bio 3D at 300K (C). The tetrahedral structure of water (C) inset.

Water is unquestionably the most abundant liquid present on earth and is vital for the existence of all life. Water comprises of an oxygen molecule covalently bound to two hydrogen atoms (Fig. 4.1A) with the oxygen nucleus causing the electron cloud distribution to distort towards the oxygen atom resulting in directional dipole moments across both hydrogen bonds. The strength of the hydrogen bond is 1.82 D (6.1×10^{-30}Cm) which can increase up to 2.4D (8×10^{-30} Cm) in its liquid phase owing to the surrounding water molecules (see the analytical description given in Chapter 2). Consequently water remains in a liquid phase across temperatures ranging 0 - 100^{o}C (273 - 373 K). Water bonds with surrounding molecules with the positive end of the hydrogen dipole bonding with the electronegative oxygen molecule (Fig. 4.1B). The shape of the water molecule and its bond angles limit the number of hydrogen bonds that can be made with neighbouring molecules. It is energetically favourable that a water molecule forms four bonds with its nearest neighbours forming a tetrahedral structure as depicted in figure 4.1C. In real systems, however, the thermal energy of the molecules means that hydrogen bonds are relatively short lived, existing for approximately 1-20 ps as given by Keutsch and Saykally. These measurements we conducted using terahertz laser vibration-rotation-tunneling spectra and mid-IR laser spectra of dimer and hexamer water clusters [66]. Despite the short-lived bond time the tetrahedral structure can still be given as the time-averaged orientation of the water molecules [67].

Other common solvents and liquids such as ethanol, methanol and 2-propanol each have unique dielectric features due to multiple relaxations arising from the dipole positioning in a large molecule that subsequently reorientate in a number of ways [68, 69] (Fig. 4.2).

To experimentally access the reported features of the aforementioned liquids the dielectric spectrum was acquired using commercial probes (Agilent dielectric probe 85070E) from 200 MHz to 40 GHz.

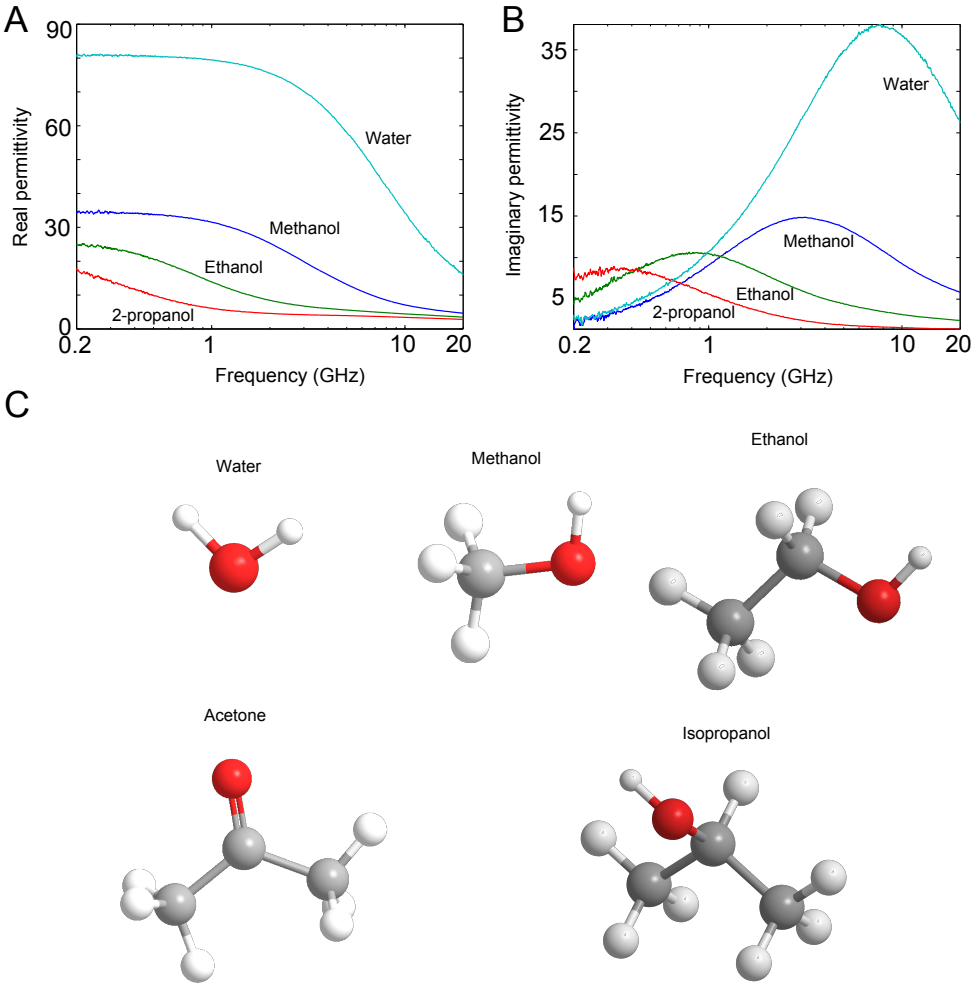


Figure 4.2: The real and imaginary permittivity response of methanol, ethanol, propan-2-ol and water across the microwave frequency range (A, B). The molecular composition of each of the chemicals (C).

4.1.1 Data fitting

The analysis and deconvolution of experimental dielectric data is somewhat complex with the presence of multiple relaxation features and conductivity. It is important to establish a sufficiently accurate model (one where the residual from a fit may be reduced no further through the introduction of additional parameters) to describe and understand the dielectric response. The method of deconvolution used within this thesis is based upon a least-mean-squares fitting routine with Debye relaxation models or aforementioned variations (2.74-2.76). The initial model employed for a fit is built on a single relaxation and the number of relaxations increased until the residual reaches a minimum given by

$$S = \sum_{k=1}^{N} W(Y_k^{meas} - Y_k^{est})^2, \tag{4.1}$$

where W is a weighting coefficient dependent on the inverse squares of the experimental values, Y^{meas} is the measured dielectric response, Y^{est} the estimated value from the model and N the total number of frequency data points. For complex data the real and imaginary components are fitted separately and the residuals combined. The frequency range covered by dielectric spectroscopy may preclude analysis of low or high frequency relaxations though tail ends of such relaxations still influence the measured response. In this case an approximation can be made by describing the one or more relaxations with a single relaxation and if necessary bind the models values to expected values from literature to help improve accuracy.

Calculating the uncertainty in the parameters used within a fitting routine of a non-linear system is a complex problem. In the cases presented within this thesis fitted models have anywhere between 3 to 11 unknown parameters such as the permittivity values, relaxation time and conductivity. Consequently a Jacobian error estimation technique is utilised for calculating the uncertainty of the parameters. Assumptions are made that the errors in the measurement are uncorrelated and that they follow a normal Gaussian distribution. The calculation of the standard error of the parameters may be given in the form

of

$$\delta = \sqrt{TR[sd^2(J^T J)^{-1}]}, \tag{4.2}$$

where TR is the trace of the matrix, sd is the standard deviation of the residuals (as given by (4.1)) and J the Jacobian matrix of the fit with the parameters given as those returned after the least-squares fit. A Jacobian matrix is the differential of the fitted function (in this case the Debye equation) where the function is differentiated with respect to the variables used within the model (i.e. Δ_1, τ_1) at each frequency. A detailed discussion regarding error analysis for parameters in non-linear fits is given by Burrell [70].

4.1.2 Analysis of polar liquids

The complex dielectric microwave spectrum of water, ethanol, methanol and isopropanol is shown in figure 4.2. Though somewhat difficult to observe by eye the presence of multiple relaxations in the frequency plot may be seen by viewing the Cole-Cole plots of ethanol, methanol and 2-propanol (Fig. 4.3). It is clear by the asymmetry of the chemical plots that multiple relaxation processes are present (Fig. 4.4). Using statistical fitting analysis given in (4.1) for the deconvolution of the spectra our results show that the dielectric spectrum of ethanol, methanol and 2-propanol all show three relaxation peaks (Table 4.1.2) and match (within the given uncertainty) previous reports on the dielectric values of common solvents [68, 69].

Owing to the high density of dipole moments, water is highly polarisable and has a relatively high static permittivity of approximately 80 at room temperature. With a complex intermolecular structure the relaxation has been suggested to not only undergo reorientational polarisation but also a translational motion [71]. In a weak electric field a water molecule begins by reorientating by rotation however this results in an energetically unfavourable equilibrium with one another and so the molecules undergo a translational motion to re-establish a low-energy structure. The reorientational and translational relaxation time of a water molecule in a liquid phase at room temperature is

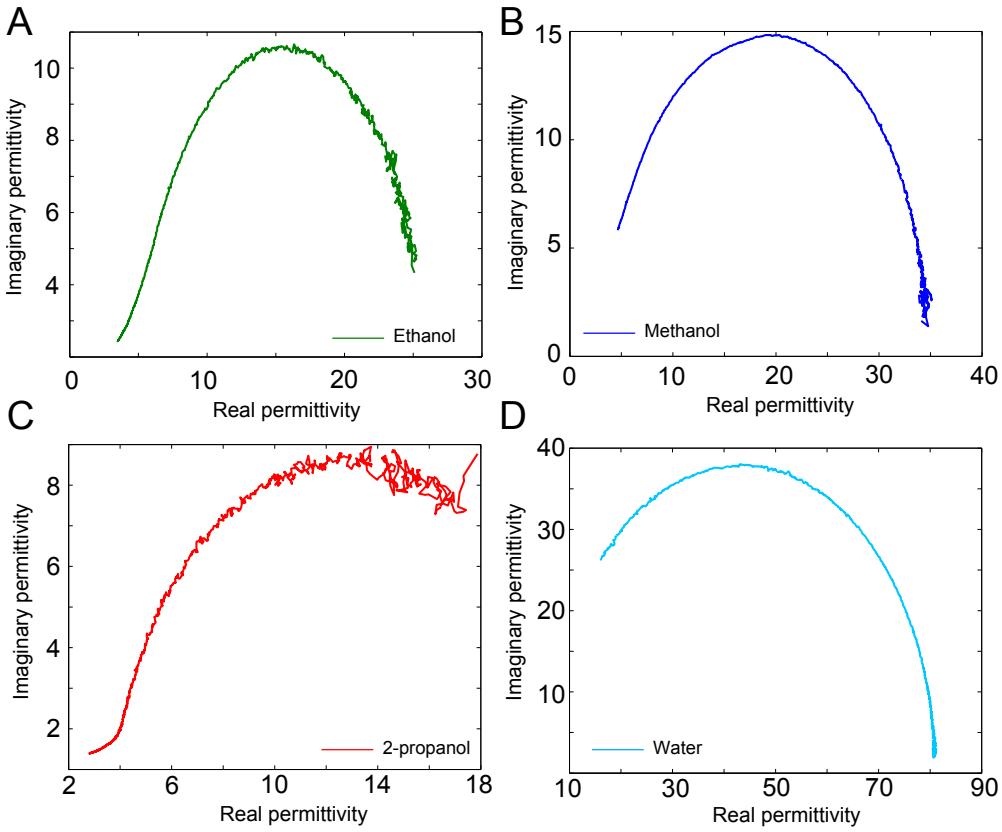


Figure 4.3: Cole-Cole plots of ethanol (A), methanol (B), propan-2-ol (C) and water (D) from 200 MHz to 20 GHz. The deviation from a single radial curve may be explained by the presence of more than one relaxation process in ethanol, methanol and 2-propanol. Of particular note is the low frequency noise. As previously discussed (Chapter 3 - Modeling, calibration, errors and permittivity calculations) the lower frequency measurements have a larger degree of uncertainty owing to the high reflection coefficients at the probe-sample interface.

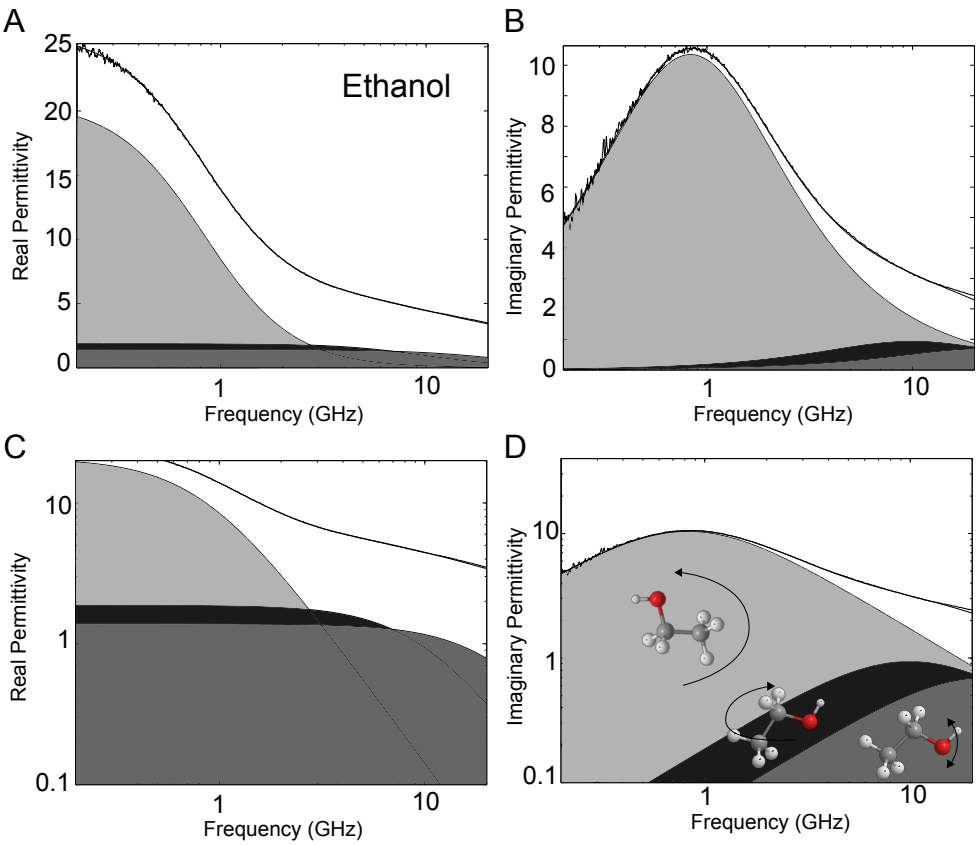


Figure 4.4: The deconvolution of ethanol into the separate dielectric contributing mechanisms (A, B). The same plot with a logarithmic scale demonstrating in detail the dielectric features of the individual constituents (C,D). The discrete relaxations may each be attributed to a form of reorientation such as the lowest to the rotation of the entire molecule around the centre of it's longest axis and the fastest to partial reorientation of the molecule. The dielectric contributions and relaxation times are given in table 4.1.2.

Liquid	ϵ_s	$\delta\epsilon_s$	Δ_1	$\delta\Delta_1$	Δ_2	$\delta\Delta_2$	Δ_3	$\delta\Delta_3$
Water	81.0	5.8	74.0	2.8	3.1	2.1	-	-
Ethanol	25.6	1.6	20.1	0.1	1.8	0.5	2.2	1.2
Methanol	35.8	2.0	19.3	1.4	11.4	1.2	4.0	1.3
2-propanol	21.3	1.2	17.1	0.1	0.9	0.5	1.6	1.0
	ϵ_∞	$\delta\epsilon_\infty$	$\tau_1(ps)$	$\delta\tau_1$	τ_2 (ps)	$\delta\tau_2$	τ_3 (ps)	$\delta\tau_3$
Water	3.9	0.9	9.8	0.3	0.1	0.0	-	-
Ethanol	1.5	0.5	193.0	0.4	19.2	2.9	4.4	3.5
Methanol	1.1	0.8	64.2	1.3	34.3	2.0	1.9	0.2
2-propanol	1.7	1.2	448.5	1.7	21.3	6.4	6.1	3.1

Table 4.1: The dielectric contributions of various polarisation mechanisms in common solvents at room temperature. Errors in the given values are based upon accuracy values quoted by Agilent in addition to variations due to the control of temperature (±0.1K) and the Jacobian parameter uncertainty estimate.

typically around 12 ps and 0.1-2 ps [68, 71, 72]. Improved measurement and modelling techniques have provided numerous reports of water confirming a second relaxation feature [68, 71]. Though the existence of a second relaxation in water is generally accepted, the exact frequency and nature of the relaxation is subject to debate [68, 71, 72]. The simplest approach was presented by Agmon [71] with a hoping distance relating to the time-averaged tetrahedral structure. More recently Zasetsky has proposed possible molecular motions of water under influence of an electric field where both relaxations are associated with large jump angle rotations (slower relaxation) and an intrawell rotational relaxation (faster relaxation) [73].

Our own measurements using microwave coaxial methods and time domain spectrometry between the frequency range of 500 MHz and 3 THz allows for the fitting of a bimodal Debye relaxation (Fig. 4.5). Using a revised version of (2.77) given by Agmon [71] the relaxation time becomes

$$\tau = \frac{\pi\eta r l^2}{k_B T}, \tag{4.3}$$

where l is the translational hopping distance. The relaxation time of the second relaxation feature was found to be 0.7±0.2 ps which compares well to

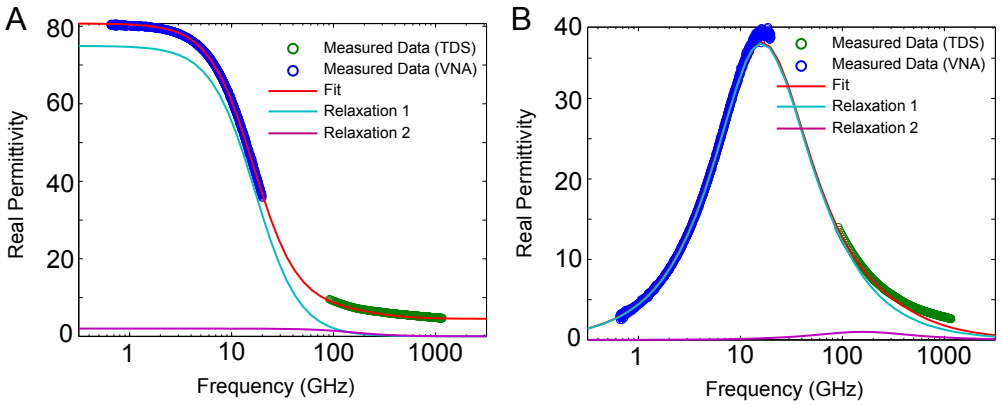


Figure 4.5: A measurement of de-ionised water at room temperature by microwave VNA (200 MHz - 20 GHz) and THz-TDS (100 GHz - 3 THz) (A, B). The deconvolution of the data confirms the presence of a high frequency relaxation component.

literature values of 0.2-1 ps. By taking the ratio of (2.77) and (4.3) we find that the translational hopping distance l is equivalent to $3.75r$. This finding clarifies the distance covered in the translational motion thereby helping to understand the mechanism driving the dielectric response. This distance was determined by Agmon [71] to correlate to a side length of the tetrahedral lattice (Fig. 4.1) suggesting after rotational reorientation the water molecules re-establish a structure similar to that found in a steady-state system.

The dielectric response of some of the most common polar liquids have been examined. In addition, a detailed analysis of water at room temperature was conducted to understand the mechanisms present and whether the Debye equation is sufficiently accurate to describe the dielectric response of water. Our findings suggest that in the frequency range of 0.2 GHz to 40 GHz a single Debye relaxation is sufficient to describe the response.

4.2 Electrolytes

The next step towards the analysis of biological solutions is to understand the role and response of ions in an aqueous solution.

Electrolyte solutions are of huge importance to our everyday lives. Whilst

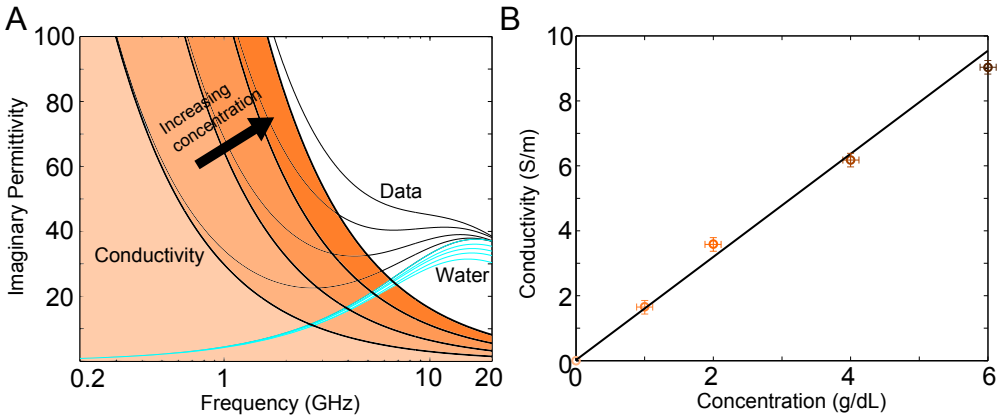


Figure 4.6: The dielectric spectrum of sodium chloride with deconvolved dielectric contributions from the ions and water (A). As ionic concentration increases so does the conductivity contribution to the imaginary permittivity (B).

water is a critical component of survival, without the presence of ions it would be unable to support biological systems. In addition to their physiological importance they are also crucial for a wealth of chemical processes and production methods in addition to a vital electrical sources in the form of batteries.

The concentration of ions present in electrolytes such as sea water, beer and blood is sufficiently high that the influences on the dielectric response described by (2.55) is present up to frequencies as high as 40 GHz (Fig. 4.6).

4.2.1 Conductivity

Typically ionic solutions are indistinguishable by spectroscopy due to a single conductivity that is the result of all ions present. Ionic concentration relates to the level of conductivity as given in (2.81) and shown in figure 4.6.

A dielectric study was conducted into the microwave response of a range of alkali metal chloride ions dissolved in water at low concentrations to measure conductivity dependence between group 1a ions (Fig. 4.7). In addition to examining the dielectric response of these ions the study can be used to confirm whether typical theories relating conductivity and mobility are upheld in the

	Group 1a	Group 2a											Group 3a	Group 4a	Group 5a	Group 6a	Group 7a
Period 1	H																
Period 2	Li	Be											B	C	N	O	F
Period 3	Na	Mg	Group 3b	Group 4b	Group 5b	Group 6b	Group 7b	Group 8	Group 8	Group 8	Group 1b	Group 2b	Al	Si	P	S	Cl
Period 4	K	Ca	Sc	Ti	V	Cr	Mn	Fe	Co	Ni	Cu	Zn	Ga	Ge	As	Se	Br
Period 5	Rb	Sr															
Period 6	Cs	Ba															

Figure 4.7: A partial periodic table highlighting the salts investigated. The elements highlighted in grey are the group 1a metal chlorides investigated concerning hydration water and the role it plays in conductivity. The elements zinc and copper were examined as copper sulphate and zinc sulphide solutions to explore the importance of ionic association and the influence on the microwave dielectric response.

limiting frequency response of conductivity. By examining the temperature dependence of electrolytes we were also able to look for a potential method to differentiate ionic solutions.

Group 1a metal chloride salts from hydrogen chloride to caesium chloride were dissolved at 250 mM concentrations in de-ionised water (5.6 $\mu\mathrm{Sm}^{-1}$). The choice of concentration was based upon a low enough conductivity so as to prevent saturation yet high enough to conduct appreciable measurement via dielectric spectroscopy. The choice of comparing group 1a ions has the advantage that the charge remains constant along with the chloride ion concentration so that ion size, mass and charge density of the group 1 elements could be investigated. The complex dielectric response was measured using the Agilent performance probe 85070 with a HP VNA in the frequency range of 500 MHz to 5 GHz. The imaginary permittivity was fitted to using a model outlined in [74] and given by

$$\epsilon''(\omega) = Af + \frac{\sigma}{\omega\epsilon_0}, \tag{4.4}$$

where A is an arbitrary fitting value used to describe the tail end of the higher frequency relaxation process of water. Temperature dependence mea-

surements were carried out from 280 K to 383 K using a digital hotplate with the electrolyte stirred at 200 RPM. The formation of bubbles at the probe tip were cleared using an air pump positioned beneath the probe prior to measurement.

The conductivity dependence of the ions investigated appears at first to be somewhat counter-intuitive. If r is assumed to be the ionic radius in (2.80) then the smallest ion such as lithium would be expected to have the highest conductivity with sodium, potassium, rubidium and caesium having a lower spread of values. This is contrary to our findings with lithium showing the lowest conductivity at identical molarity to the other ions (Fig. 4.8). Sodium is also seen to have a lower conductivity than larger ions. The explanation for this is found in the charge density and the hydrated ionic radius. Microwave dielectric studies on the relaxation of bound ionic water of a range of electrolytes have shown that lithium has a large hydration shell (approx. 3.9 bound water molecules per ion), as does sodium (approx. 2.6 bound water molecules per ion), however, potassium, rubidium and caesium have no hydration shell [75] (Fig. 4.9). Water molecules within a hydration shell are often irrotationally bound to the ion which leads to an increased cross-sectional area and therefore greater drag when the ion is accelerated through a liquid. From (2.81) it is inferred that a reduced mobility will subsequently lower the conductivity (Fig. 4.9). This rational is in good agreement with our experimental findings with lithium demonstrating the lowest conductivity, sodium the second lowest and potassium, rubidium and caesium all showing similar higher conductivity values at matched molar concentrations.

The study of hydrogen chloride also revealed an anomalous ionic conductivity three times greater than potassium chloride. Hydrogen chlorides large ionic mobility is attributed to the proton hopping phenomena described by the Grotthuss mechanism [76]. The additional hydrogen ions present in the solution diffuse by first bonding to a water molecule that has broken an existing hydrogen bond thereby liberating a hydrogen ion that in turn then bonds to a nearby neighbour (Fig. 4.10). This process continues further with each bonding occurring on a time scale of 1.5 ps as observed by NMR and calculated by simulation [76].

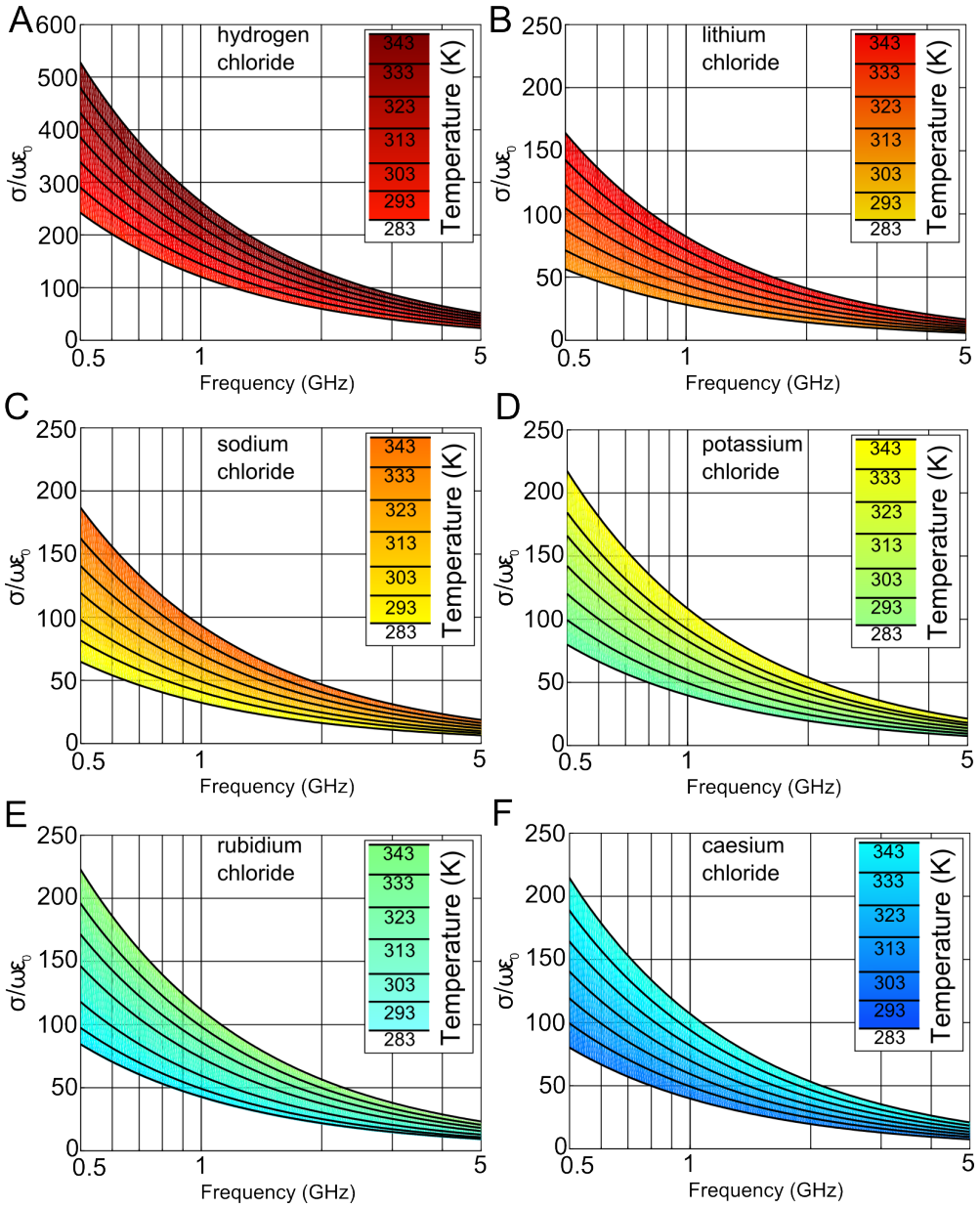


Figure 4.8: The conductivity contribution as a function of frequency and temperature of group 1a metal chlorides in water; hydrogen chloride (A), lithium chloride (B), sodium chloride (C), potassium chloride (D), rubidium chloride (E) and caesium chloride (F).

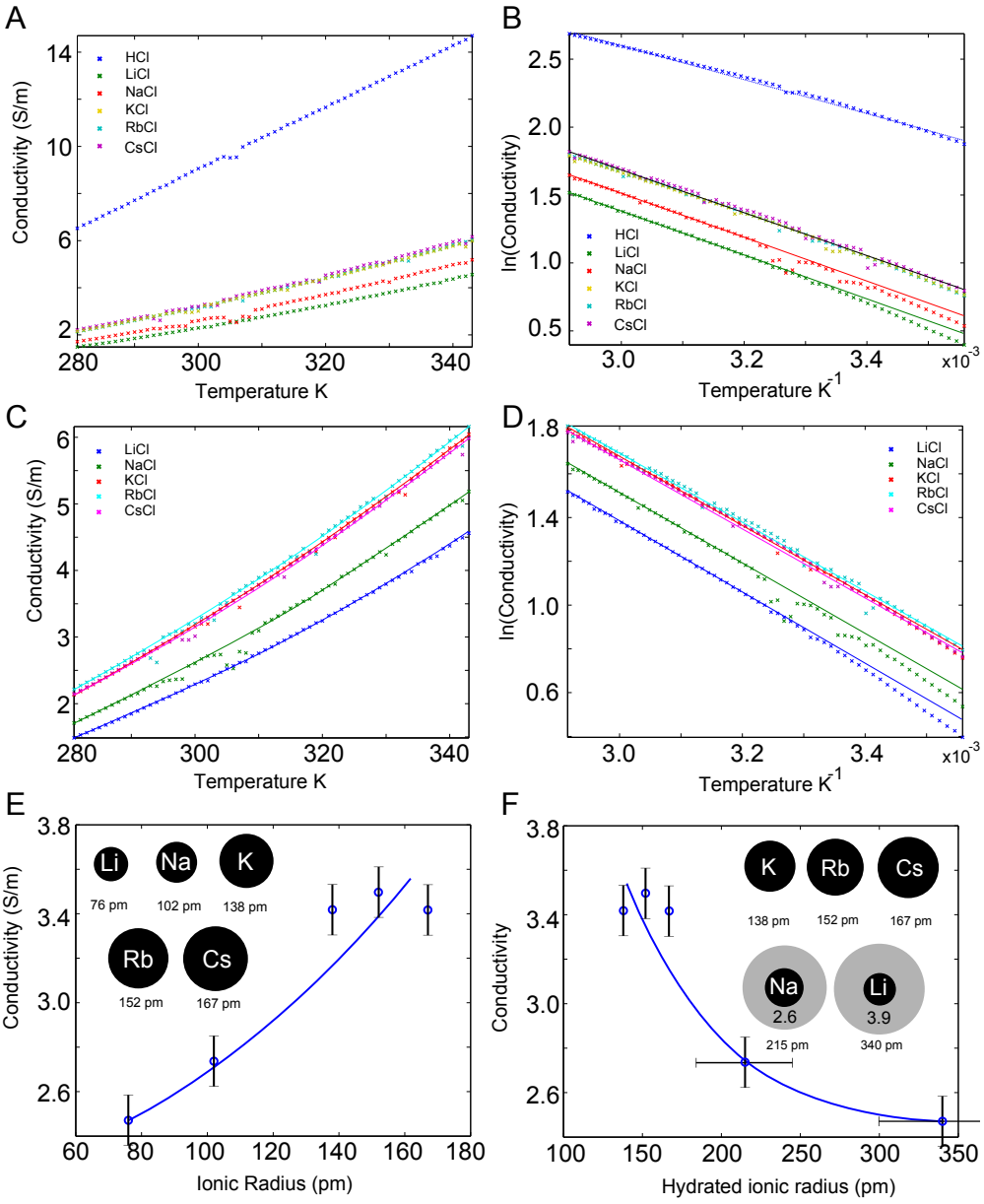


Figure 4.9: The change in conductivity as a function of temperature for the group 1a metal chlorides (A,C). The presence of bubbles are highly apparent by the sudden deviation from the expected trend. The error induced by the presence of bubbles is estimated to be $\sigma \pm 0.3$ S/m Arrhenius plot of conductivity as a function of inverse temperature highlighting the non-linearity of lithium and sodium (B,D). The conductivity as a function of ionic radius at room temperature (E) and conductivity as a function of hydrated ionic radius at room temperature (F).

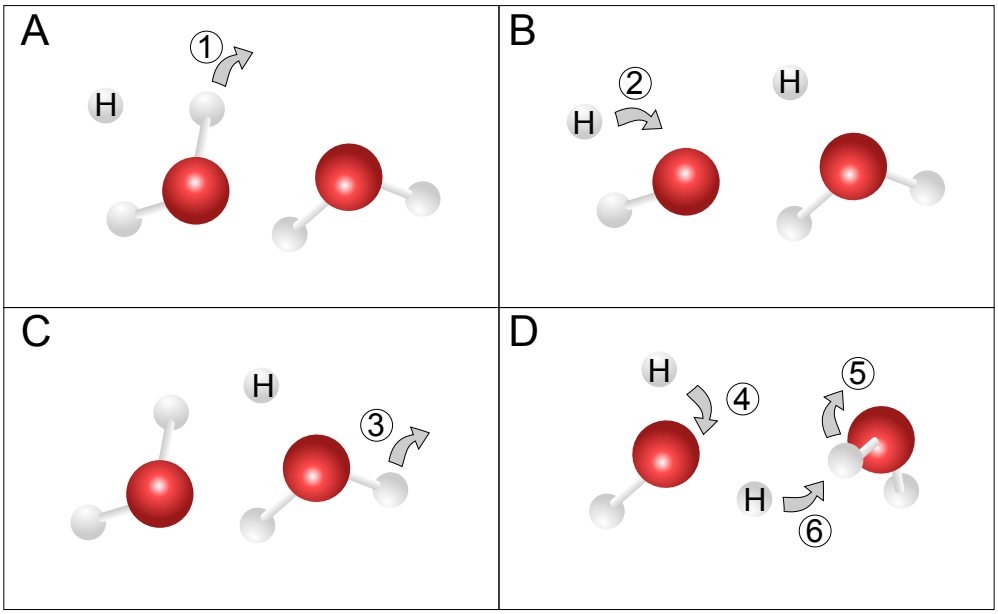


Figure 4.10: Proton hopping process that leads to anomalously high conductivity for hydrogen chloride. The additional hydrogen ions present in the solution diffuse by first bonding to a water molecule that has broken an existing hydrogen bond (A,B) thereby liberating a hydrogen ion that in turn then bonds to a nearby neighbour that has liberated a hydrogen atom (C,D).

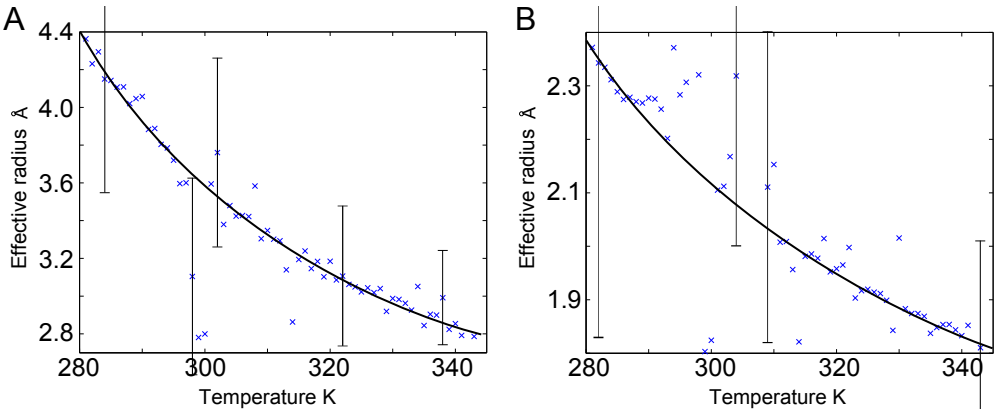


Figure 4.11: The calculated effective hydration radius of lithium (A) and sodium (B) as a function of temperature. Representative error bars show the uncertainty induced by the presence of bubbles in addition to the extrapolated parameters from the fit. Though the uncertainty is large the statistical trend is sufficient to make a fit.

The temperature dependence of the aforementioned ions presented a means to explore the temperature effects on the hydrated radius. As defined by (2.79) the conductivity of an electrolyte is given as the sum of the individual ionic conductivities, for example

$$\sigma_{LiCl} = \sigma_{Li} + \sigma_{Cl} = \frac{qc}{6\pi\eta}\left(\frac{1}{r_{Li}} + \frac{1}{r_{Cl}}\right), \tag{4.5}$$

in the case of lithium chloride. As already established the variation in conductivity between the various salts examined are attributed to an effective radius dependent on the size of the solvation shell. Our temperature dependent findings suggest that the hydrated ionic radius of lithium and sodium is highly temperature dependent. Based on reported experiment findings that potassium, rubidium, caesium and chlorine have no bound solvation shell [77] (in agreement with the linear Arrhenius plot of potassium, rubidium and caesium (Fig. 4.9)) the hydrated radius can be calculated by the ratio of electrolyte conductivities. The ratio of two electrolyte conductivities example the case of CsCl and LiCl is therefore

$$\frac{\sigma_{CsCl}}{\sigma_{LiCl}} = X = \frac{\sigma_{Cs} + \sigma_{Cl}}{\sigma_{Li} + \sigma_{Cl}} = \frac{1/r_{Cs} + 1/r_{Cl}}{1/r_{Li} + 1/r_{Cl}}, \tag{4.6}$$

which is re-expressed to solve for the hydrated radius of lithium

$$r_{Li} = \frac{X r_{Cl}}{\left[\left(\frac{r_{Cl}}{r_{Cs}} + 1\right) - X\right]}. \tag{4.7}$$

Using calculated hydrated ionic radii for r_{Cl}, r_K, r_{Rb} and r_{Cs} [78] values were obtained for the hydrated ionic radii of lithium and sodium. At room temperature (25^{o}C) the hydrated radii of sodium and lithium were in agreement with reported findings at 215±21 (225 [78]) and 340±39 (300 [78]) pm, respectively. With increasing temperature the calculated effective radii of sodium and lithium reduce to 180 and 280 pm, respectively, at 70^{o}C (Fig. 4.11). This is the first temperature dependent study of ionic hydration shells across such broad range of temperatures.

As discussed the rate of change in the conductivity as a function of concentration is highly dependent on the hydrated radius. The fact that only two of the ions had permanent hydrated radii suggests that temperature dependent measurements are ineffective for the differentiation or identification of ionic solutes, especially as most real solutions contain multiple ionic species. This study has however demonstrated an effective technique for the measurement of the temperature dependent hydration radii.

4.2.2 Ion-association

In addition to the conductivity effects of ionic solutions in the imaginary permittivity, relaxation mechanisms have been reported to occur in certain ionic species.

The dielectric spectrum of more complex salts were examined to explore the various relaxation processes that occur in some electrolytes. Solutions such as serum contain a range of ionic solutes therefore making it important to understand the dielectric impact of any complex salts present. Deconvolution of the spectrum was carried out using statistical analysis laid out in (4.1).

Many salts owe their multi-modal dielectric spectrum to the partial disso-

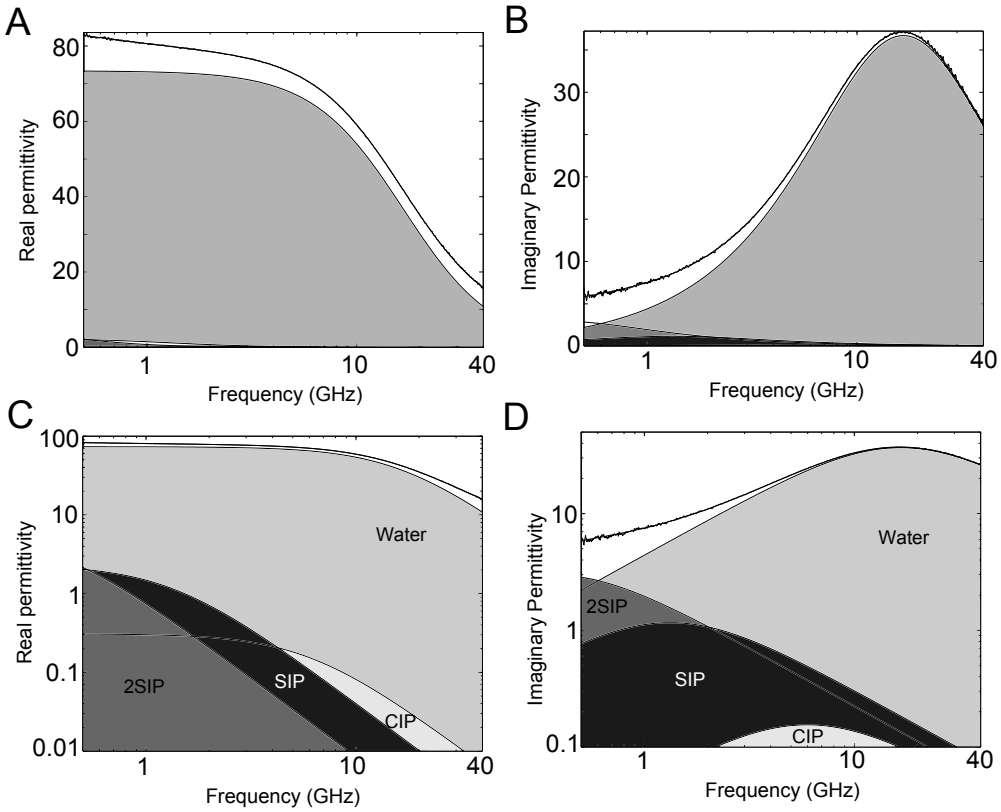


Figure 4.12: The deconvolution of the dielectric spectrum of copper sulphate by statistical analysis (A,B). Three of the four relaxations are attributed to varying degrees of ion-association; double solvent-separated ion pair (2SIP), solvent-shared ion pair (SIP) and contact ion pair (CIP). The double logarithmic plots highlight the contributions from the respective ion-pairs (C,D).

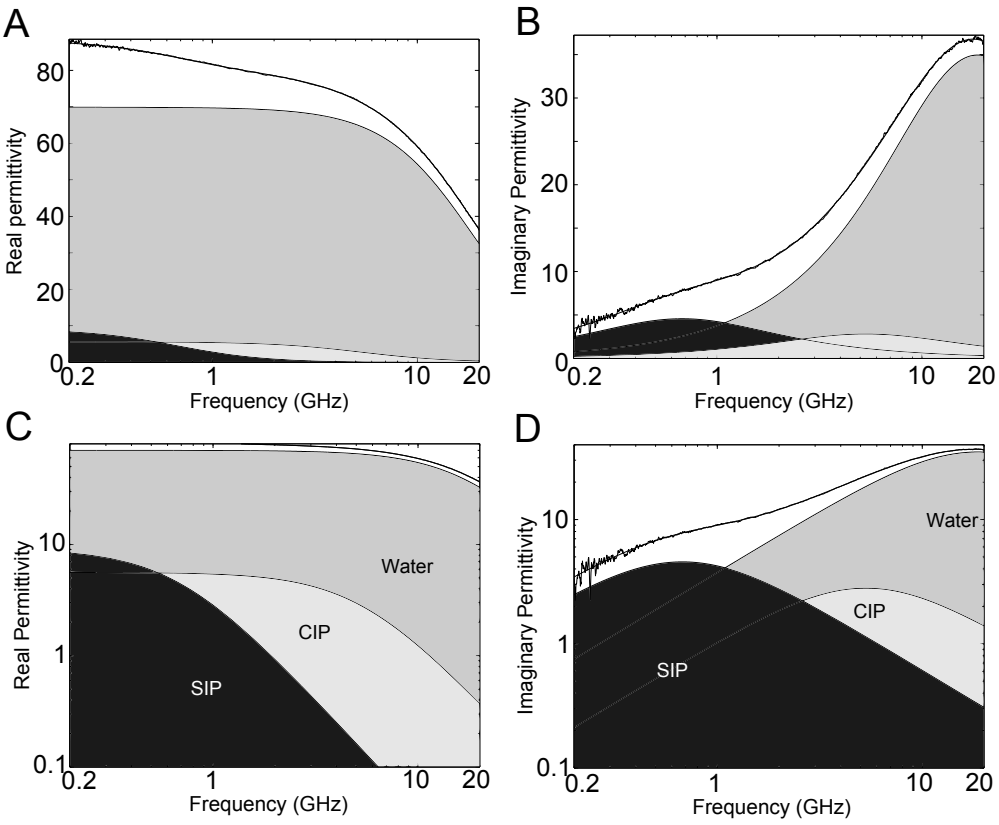


Figure 4.13: The deconvolution of the dielectric spectrum of zinc sulphide by statistical analysis (A,B). Two of the three relaxations are attributed to ion-association; solvent-shared ion pair (SIP) and contact ion pair (CIP). The double logarithmic plots highlight the contributions from the respective ion-pairs (C,D).

ciation of ions when dissolved in aqueous solution, a good example being copper sulphate ($CuSO_4$) [79]. The deconvolution of experimental data for copper sulphate and zinc sulfide solutions shows that the electrolyte exhibits no less than four relaxation processes between the frequencies of 500 MHz and 40 GHz (Fig. 4.12 and Fig. 4.13). The presence of multiple relaxations cannot be explained by hydration shell water owing to the static permittivity being significantly higher than that of pure water suggesting additional polarisation mechanisms at work. Ion-association can be utilised to comprehend the elevated permittivity. Ions form a number of associated states in a polar liquid depending on the Coulomb force between an anion and cation [80]. The governing features of ion association are ion charge and solution permittivity such that the inter-ionic force is

$$F = \frac{q_1 q_2}{4\pi\epsilon r^2}, \tag{4.8}$$

where ϵ is the permittivity of the solution and $q_{1,2}$ the charge of the respective ions. Higher permittivity liquids therefore electrostatically shield the ion from other ions thereby reducing ion-association. Three types of ion-association states exist; fully solvated, solvent-separated and contact (Fig. 4.14). Ions in a solvent-separated state adopt a number of discrete separation distances dependent on the number of hydrating molecules. In the case of copper sulphate all three states are present. For the previously investigated group 1a alkali metal ions almost all ions are fully solvated in water. Higher charges in ions such as magnesium, aluminium and copper result in measurable association in the form of solvent-separated pairs and contact pairs.

The largest contribution to the dielectric spectrum of the copper sulphate electrolyte is attributed to water, however, the three lower frequency relaxation processes are explained with various states of ion association (Fig. 4.14). Three known type of association may occur; double solvent-separated ion pair (2SIP), solvent-shared ion pair (SIP) and contact ion pair (CIP). In the case of zinc sulphate it is possible that the 2SIP association is energetically unachievable owing to the higher charge density of the sulphur ion in comparison to the sulphate ion in copper sulphate. It is inferred from (2.77) that ions

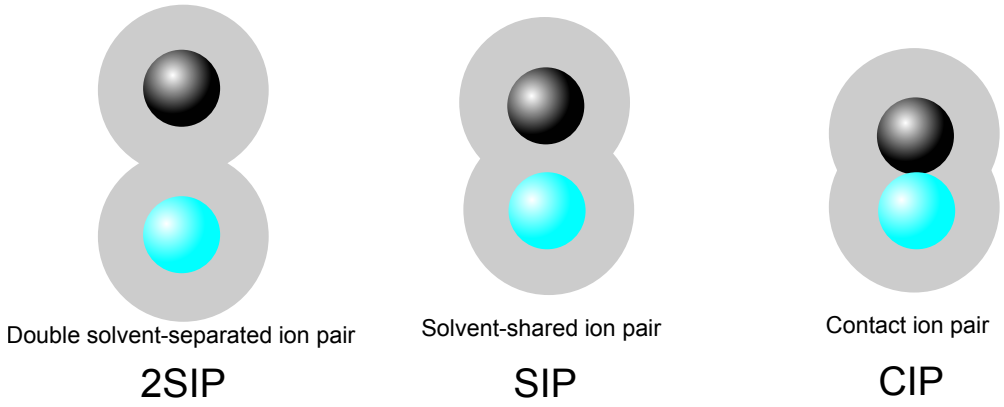


Figure 4.14: Varying degrees of ion-association responsible for multiple relaxation phenomena in the dielectric spectrum. The light grey circles highlight the hydration radii of the respective ions and the blue and black spheres the ions.

with the greatest dissociation will have the largest effective radius and therefore the lowest relaxation time. The lowest frequency relaxation is allocated to the double solvent-separated ion pairs, the second to solvent-shared ion pairs and the highest to contact ion pairs. Using (2.77) we can infer from the relaxation times that the effective radial distances are related such that $r_1 = 1.6r_2$ and $r_1 = 2.5r_3$.

The findings highlighted in this section demonstrate the range of relaxation process that can arise even from simple ionic solutes. Great care must therefore be taken when analysing solutions that contain a number of ionic solutes.

4.3 Summary

The dielectric response of polar liquids and electrolytes have been reported. The complex permittivity and relaxation features of polar liquids have been experimentally validated to relate to the dipole density and molecular size, respectively. The conductivity temperature dependence of group 1a alkali metals has been studied and the conductivity found to depend on the hydration ionic radius. Subsequently, the temperature dependent hydration radius of sodium and lithium was calculated. The deconvolution of the dielectric

spectrum of copper sulphate and zinc sulphate reveals a number of relaxation process. These results were discussed and compared to literature findings and explained in terms of ion association.

Chapter 5

Dielectric properties of biological solution

Having examined the dielectric contributions from the most basic constituents of a biological solutions, namely water and salts, analysis can now be conducted on more complex solutions.

5.1 Biological solutions

A biological solution refers to any liquid containing complex organic solutes for example the 5 L of blood circulating in our body and providing vital nutrients to our organs, tissue and cells. The most complex and varied constituents of blood are proteins, serving many roles such as the transportation of oxygen, hormones, lipids and vitamins as well as aiding the immune system. In other environments within the body proteins serve to encode genes, catalyse chemical reactions and aid in the selective transport of molecules [81]. Understanding how a protein responds to its environment is vital for understanding how a protein performs its role. Herein the dielectric response of proteins are examined and the role of hydration water explored.

5.1.1 Mixed media

To understand the average dielectric response of a material composed of two media mixed on a sub-wavelength scale we must use mixed media theories. A number of models exist for the calculation of the dielectric properties of mixtures such as the Maxwell-Garnett theory [82], Polder and van Santen theory [83], Pecharroman theory [84] and Bruggerman theory [85]. For the purpose of our study, at filling factors below 20 % and with solutes that are approximately 10^7 times smaller than the wavelength the Maxwell-Garnett theory is sufficient for the description of the dielectric properties of a solution with proteins.

Returning to the Clausius-Mossotti formula (2.17), let us consider the simplest case of spherical particles of permittivity ϵ_p suspended in a medium of permittivity ϵ_m. In such a case the Clausius-Mossotti formula becomes

$$\frac{N\alpha}{3\epsilon_p} = \frac{\epsilon_{eff} - \epsilon_p}{\epsilon_{eff} + \epsilon_p}, \tag{5.1}$$

where N is the average number of molecules per unit volume. An expression of the polarisability α for the sphere in terms of the permittivity of the medium and particle is given by

$$\mathbf{p} = \alpha\mathbf{E} = (\epsilon_p - \epsilon_m)\int_V \mathbf{E}_c dV \tag{5.2}$$

where α is

$$\alpha = \Phi(\epsilon_p - \epsilon_m)\frac{3\epsilon_m}{\epsilon_p + \epsilon_m}, \tag{5.3}$$

due to the relationship between the electric field inside the particle $\mathbf{E}_c$ from a field outside $\mathbf{E}_o$ as given in (2.27). By substitution of (5.3) into (5.1) we arrive at the relationship

$$\frac{\epsilon_{eff} - \epsilon_p}{\epsilon_{eff} + \epsilon_p} = \Phi \frac{\epsilon_p - \epsilon_m}{\epsilon_p + \epsilon_m}, \tag{5.4}$$

where $\Phi = NV$ and can be regarded as the volume fraction occupation of the medium with permittivity ϵ_m. Equation (5.4) is re-expressed as

$$\epsilon_{eff} = \epsilon_p + 3\Phi\epsilon_p \frac{\epsilon_m - \epsilon_p}{\epsilon_m + 2\epsilon_p - \Phi(\epsilon_m - \epsilon_p)} \tag{5.5}$$

which is known as the Maxwell-Garnett mixing formula [82]. In the limit of low concentration the equation can be approximated to be

$$\epsilon_{eff} = \epsilon_w \left(1 + \frac{3\Phi(\epsilon_m - \epsilon_p)}{\epsilon_m + 2\epsilon_p}\right) \tag{5.6}$$

By measuring the low frequency static permittivity of water using a VNA at 50 MHz the dielectric impact of four proteins on the dielectric constant of water was observed (Fig. 5.1). The static permittivity is seen to decrease with increasing protein concentration and from (5.5) the permittivity of the proteins is calculated to be within the range of 11 to 14. Ovalbumin - 12.7±0.6, lactoglobulin - 12.8±0.6, bovine serum albumin - 13.8±0.7 and lysozyme - 11.1±0.6.

5.1.2 Proteins and bound water

At the molecular level proteins are almost entirely constructed from the 20 molecular building blocks of life known as amino acids that bond via peptide bonds (amide bonds) and form linear polymers known as polypeptide chains. These primary structures then fold to form secondary structures due to hydrogen bonding between amino acid groups which form into two predominant structures, α helices and β sheets. Tertiary structures are the result of additional bonding between molecules within two different secondary structures. The final product of these large polypeptide chains is a complex but stable

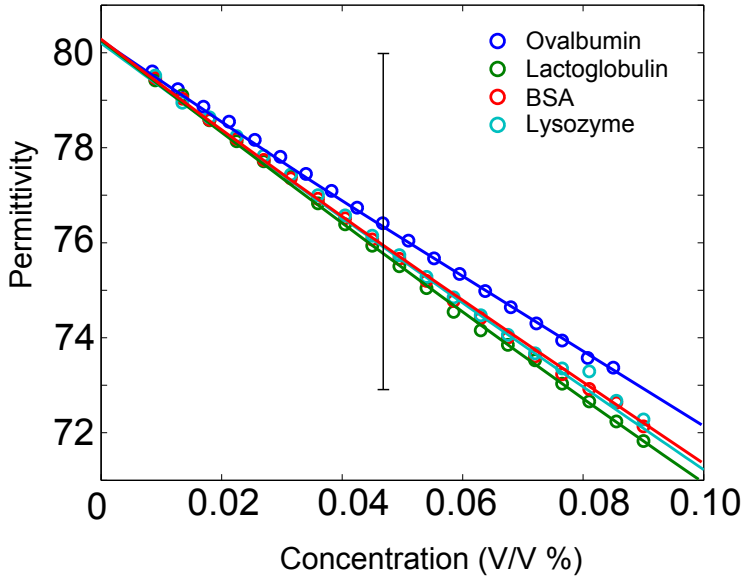


Figure 5.1: The permittivity at 200 MHz as a function of protein concentration (ovalbumin, lactoglobulin, bovine serum albumin and lysozyme) with fitted Maxwell-Garnett equations for the calculation of protein permittivity. A representative error calculated from the absolute value uncertainty of the measurement technique.

molecule known as a protein (Fig. 5.2). Additional binding with other proteins can occur to form quaternary structures. Proteins can be found within almost every biological system and are a vital constituent to life. They are present in a huge range of environments and serve a great range of purposes from molecular selective entry at cellular membranes to helping to supply and distribute oxygen to organs and tissue throughout the body.

Protein hydration is vital for protein activity and structure; mediating bonds between peptides [86], interacting with existing hydrogen bonds and aiding in the activation of folding processes of primary and secondary structures [87]. The surface of most proteins have a large surface density of amino acids with unbound dipole moments. Immersed in water the molecular dipoles of the solution will interact with the dipole moments of the solute leading to a variation in conformational state and stability of the protein as well as affecting the aqueous structuring more than 1 nm away [88]. Owing to the structural complexity of a protein the nature of a water molecules interaction varies dramatically across the surface and even in the interior of the protein.

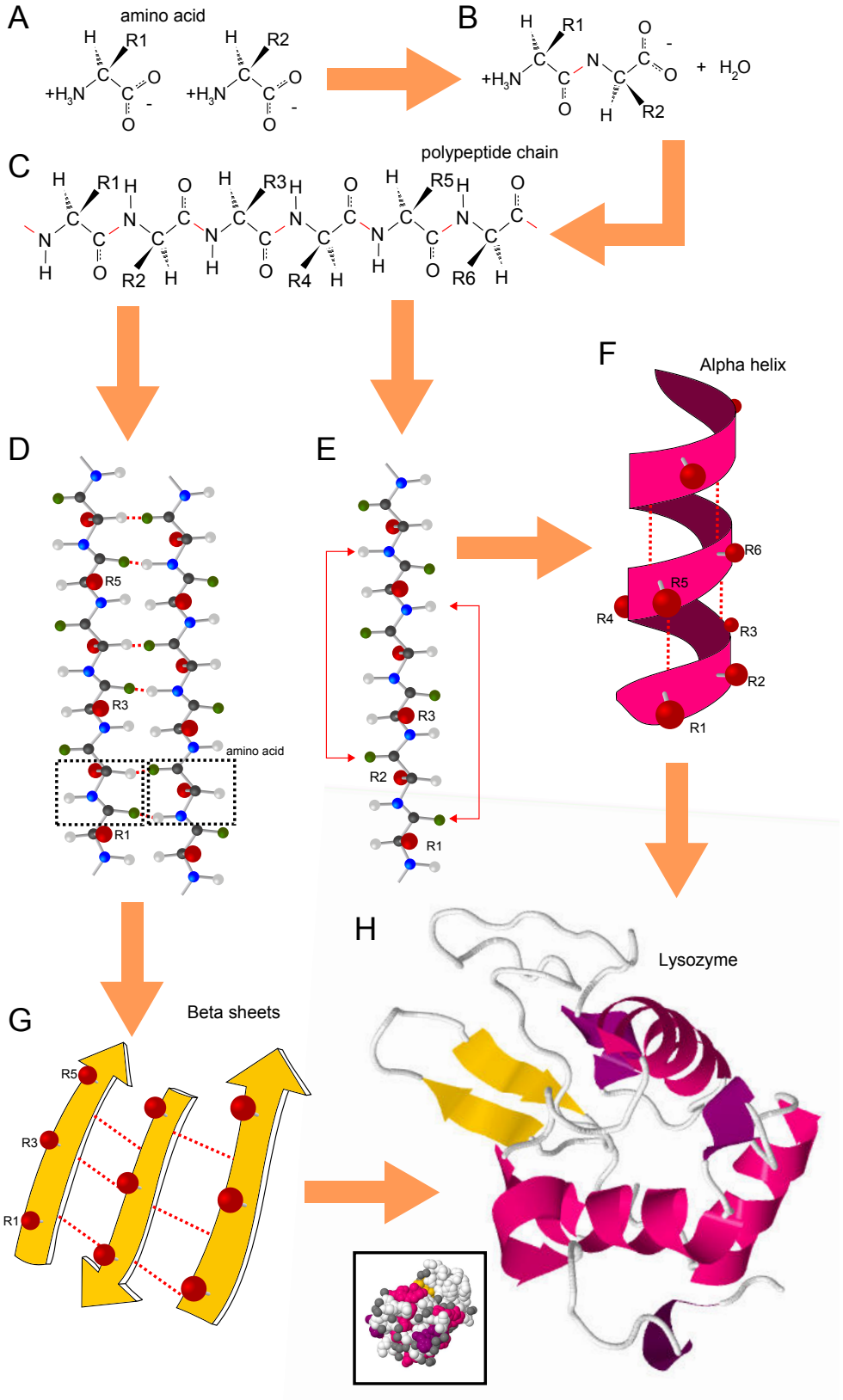


Figure 5.2: The construction of a protein. Amino acids (A) form the basis of a proteins by forming polypeptide chains (B,C) that in turn form secondary structures (Alpha (D,G) and Beta sheets (E,F)) before finally forming the tertiary protein structure (H).

Determining the location of water molecules in and around a protein has primarily been achieved via high resolution X-ray analysis [89] with bond strengths calculated by molecular dynamic simulations using the Monte Carlo technique [90].

A protein structure has a range of interesting hydrodynamic features from regions containing high densities of NH and CO groups, crevasses of nanometre length and hydrophobic areas. The mobility of a water molecule is highly dependent on the surrounding environment and bonding interaction. At an amine/carboxyl bond rich area such as the surface of an α helix or within a hydrophilic crevasse, water molecules will bond with a greater bond strength than with bulk water resulting in reduced mobilities [91]. Surfaces such as those described have been found to have an excess of hydration sites compared to the number of water molecules that is reported to increase bound water density by up to 20%. At hydrophobic protein sections water gains a greater degree of mobility than bulk water which is explained by the lack of interactions acting on approximately one half of the molecule. The mobility rapidly returns to that of bulk water as a function of distance from the protein surface however differences to bulk water have still been reported by THz-TDS up to 2 nm away [88]. This long distance effect of the protein surface on water assists the protein in having an extended electrostatic surface thereby making its presence more apparent to passing molecules. Additionally, there are many amino acids with charged side-chains leading to the immediate water being highly ordered.

The use of dielectric spectroscopy, for protein analysis has been used to determine protein hydration numbers as well as for the approximate determination of molecular size. Dielectric spectroscopy is however unable to spatially locate regions of bound water and therefore results from NMR, x-ray and neutron diffraction techniques must be drawn upon to make conclusive arguments regarding protein water dynamics.

From the point of view of relaxation dynamics bound water exhibits a different relaxation time to bulk water due to its reduced mobility as established in (2.77). Whilst it has been agreed within the scientific community that bound water exhibits different relaxation properties compared to bulk water it is a

subject of much contention as to what models best describe the distribution of relaxation times [92, 93, 94, 95, 96]. In addition to water many proteins have been found to exhibit reorientational properties in an electric field with relaxation times of the order of tens of nanoseconds [94, 95]. The relaxation time of a protein can still be described by (2.77) though discrepancies between experimental and theoretical predictions ($r = 1.2r_{prot}$) arise due to the non-spherical shape approximated by r in (2.77) and surface roughness of proteins [97]. In dielectric spectroscopy the relaxation time of these proteins occur around 1-10 MHz. As higher frequencies are approached (100 MHz-5 GHz) other relaxations are observed and commonly attributed to various mechanisms or types of water (bound/hydration water and bulk water) [92].

With the increasing accuracy of dielectric measurement techniques and microwave sources, measurements of the dielectric spectrum and relaxation times of proteins and bound water are improving. However, the small contribution of bound water to the static permittivity (2.2% at $\Phi = 0.16$) remains a hindrance to investigation. Across the frequency range of 1 Hz to 40 GHz current models typically employ four relaxation processes, attributing the lowest and highest to protein relaxation and bulk water, respectively. Reports on single [92, 93], double [94, 95, 96] and triple [94] relaxation process often make strong arguments for the case of using such models. The measurement techniques used may explain some variation though the common use of the same commercial equipment suggests otherwise (repeatability - 1-2 %). Owing to the unique topologies and structure of each type of protein it is possible that each species of protein should be approached with its own relaxation model.

Focusing upon the bimodal relaxation model of bound water there have been two opinions as to the cause. The first, proposes two types of hydration water, partially bound and tightly bound, the latter contributing to the slow relaxation time occurring around 800 ps and the former to high frequency relaxation at 40 ps [95, 93]. The second school of thought is that both fast and slow relaxations may be attributed to the cross-correlation (intermolecular interaction creating additional dielectric effects) of bound water at the surface of a protein and the free water within a second hydration layer [96]. Up until Nandi and Bagchi's work the cross-correlation of two systems leading

to a dielectric response had been largely overlooked. In a system comprising of three dielectric mechanisms, protein reorientation, bound water and bulk water there are be three self-correlated mechanisms that would appear as the normal relaxations and three further cross-correlated responses. At first cross-correlation may not appear an intuitive approach in explaining dielectric properties though it has been shown to be a very real mechanism in many molecular dynamic simulations and NMR studies [94, 98, 99]. The physical mechanism behind cross-correlation may be considered to be the result of the combinations of polarisation effects from two systems. As governed by a correlated response the effect will have a relaxation response that lies between the two governing mechanisms.

Nandi and Bagchi considered the cross-correlation of bound water and bulk water the likely mechanism responsible for the low frequency relaxation. The interchanging motion of bound and free water molecules was theoretically reported to exhibit a bimodal relaxation that exhibit similar relaxation times to those observed experimentally [96].

Both views have recently come under scrutiny by Oleinikova et al. based on new findings suggesting residence times of water at the surface of the protein are limited to 50-10 ps [94] (protein surface bonds are of insufficient strength to reduce a water molecules mobility more). According to the report high frequency relaxation (50-25 ps) is solely related to all forms of hydration water and that the nanosecond processes occurring is based on water-protein cross-correlations.

Oleinikova et al. have proposed what is likely the most complete argument for the features observed within the dielectric spectrum of protein solutions backed by a wealth of findings from other groups [94]. The dielectric community has however been slow to adopt such views and can still be seen citing tightly and loosely bound water as the reason for low and high frequency relaxations [93, 95].

The presence of an additional relaxation occurring around 500 MHz in the case of some proteins was also suggested by Oleinikova et al. [94] proposing that intraprotein motions such as solvent exposed side chains contribute to

the dielectric spectrum. However, most experimental dielectric measurements have failed to report such observations [93, 95, 92].

Based on dielectric measurements made by an Agilent temperature probe and performance probe our findings suggest that at least three relaxations provided the most accurate fit (Fig. 5.3) to the data of ovalbumin, lysozyme, bovine serum albumin (BSA) and lactoglobulin solutions in the frequency range of 200 MHz to 20 GHz (Fig. 5.4 and Fig. 5.5). BSA, ovalbumin, lactoglobulin and lysozyme (purchased from Sigma-Aldrich) were selected for the broad representation of protein structures and size. Owing to the limit of the low frequency range it is not possible to distinguish between cross-correlation effects and the lower frequency protein reorientation relaxation. Consequently the tail-end of any relaxation process would become amalgamated with the δ_1 relaxation therefore making a third-order fit ideal for our frequency range.

The large number of variables associated with a third- or fourth-order fit make fitting with unrestrained limits on variables impossible. Subsequently, reasonable fitting ranges were constructed for relaxation times and permittivity contributions up to the third-order model. The fourth-order fit was conducted with the relaxation time unconstrained so as to maximise the chance of finding any additional relaxation processes. The residual values given by (4.1) were calculated for each fit (first- to fourth-order) and for protein solutions of ovalbumin, lactoglobulin, BSA and lysozyme at a concentration of 18 g/dL. The residual values demonstrate that a third-order Debye fit yielded the simplest and most accurate fit. It is possible to implement Cole-Cole or Cole-Davidson fitting however the addition of three extra variables would make the fitting cumbersome and possibly less accurate without improved variable constraints. The assessed dielectric response is therefore given by three Debye relaxations

$$\epsilon^*(\omega) = \epsilon_\infty + \frac{\Delta_1}{1 + i\omega\tau_1} + \frac{\Delta_2}{1 + i\omega\tau_2} + \frac{\Delta_3}{1 + i\omega\tau_3}, \tag{5.7}$$

where $\Delta_k = \epsilon_k - \epsilon_{k+1}$ and is the relative dielectric contribution assigned to the given relaxation.

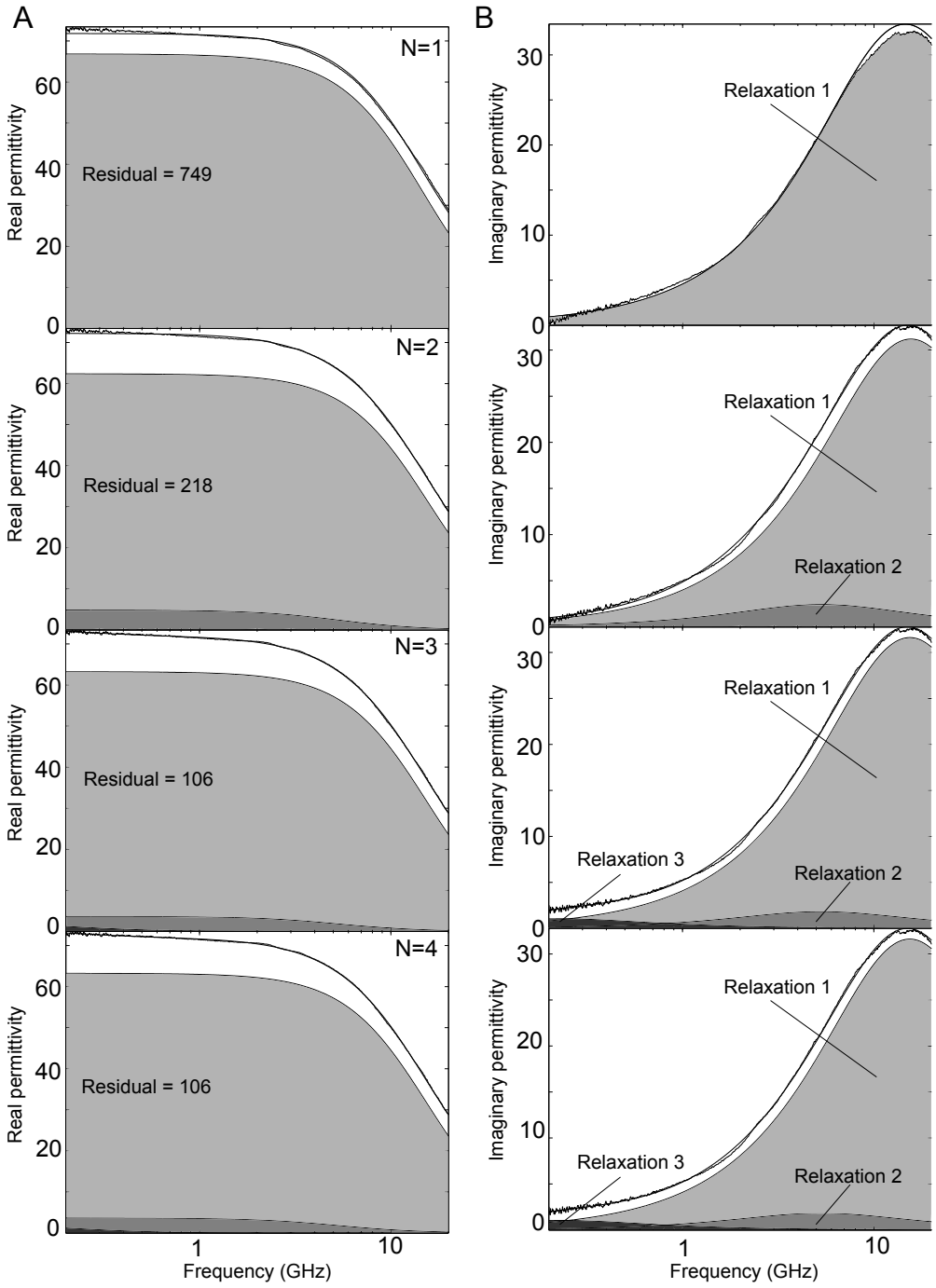


Figure 5.3: Real (A) and imaginary (B) permittivity of a protein solution (BSA - 18 g/dL) with fits of a first order to fourth order Debye equation. The first order Debye fits shows noticeable differences between the measured and theoretical fit. Though a second order model improves the fit there are still significant differences at frequencies from 200 MHz to 3 GHz. The third order model has the lowest residual from the fit and the fourth order model showed no further reduction to the residual of the fit.

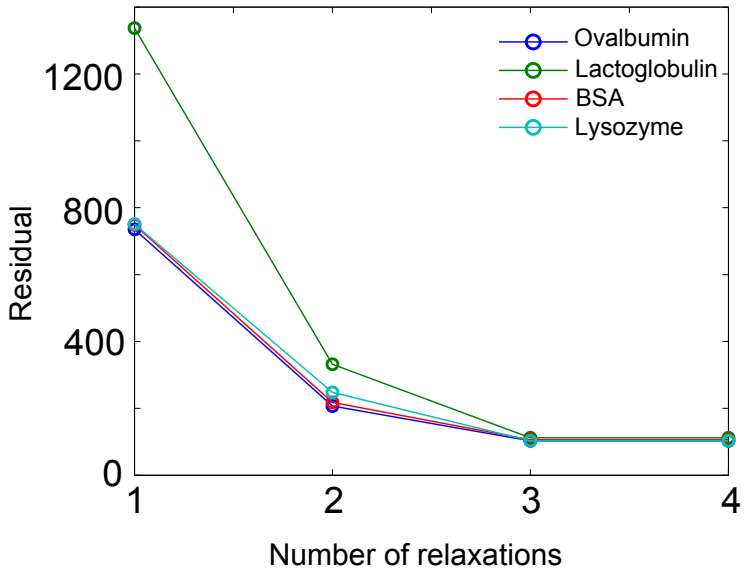


Figure 5.4: The residual according to (4.1) between a fit and data (ovalbumin, lactoglobulin, BSA and lysozyme at 18 g/dL) with respect to the number of relaxation process fitted.

Our preliminary findings concerning the relaxation times and dielectric magnitudes of lysozyme are in general agreement with values given by Cametti et al. [95] with a high frequency relaxation peak observed at 5.05±0.62 GHz (Fig. 5.5, Cametti et al. approx. 4 GHz). No high frequency data with the deconvolution of relaxation spectra is currently available for comparative purposes on ovalbumin, lactoglobulin or BSA at the time of writing. There was no suggestion of a 500 MHz relaxation as indicated by Oleinikova in any of the protein solution spectra [94]. It is observed that at matching concentrations the dielectric contributions from the various proteins is not the same.

5.1.3 Protein solution differentiation by microwave Debye relaxation analysis

By itself, dielectric spectroscopy is a limited tool for the understanding of protein dynamics and hydration water and is able only to yield total molecular hydration numbers. Whilst the ideal model to describe the dielectric spectrum of a protein solution is the subject of much debate, based upon the

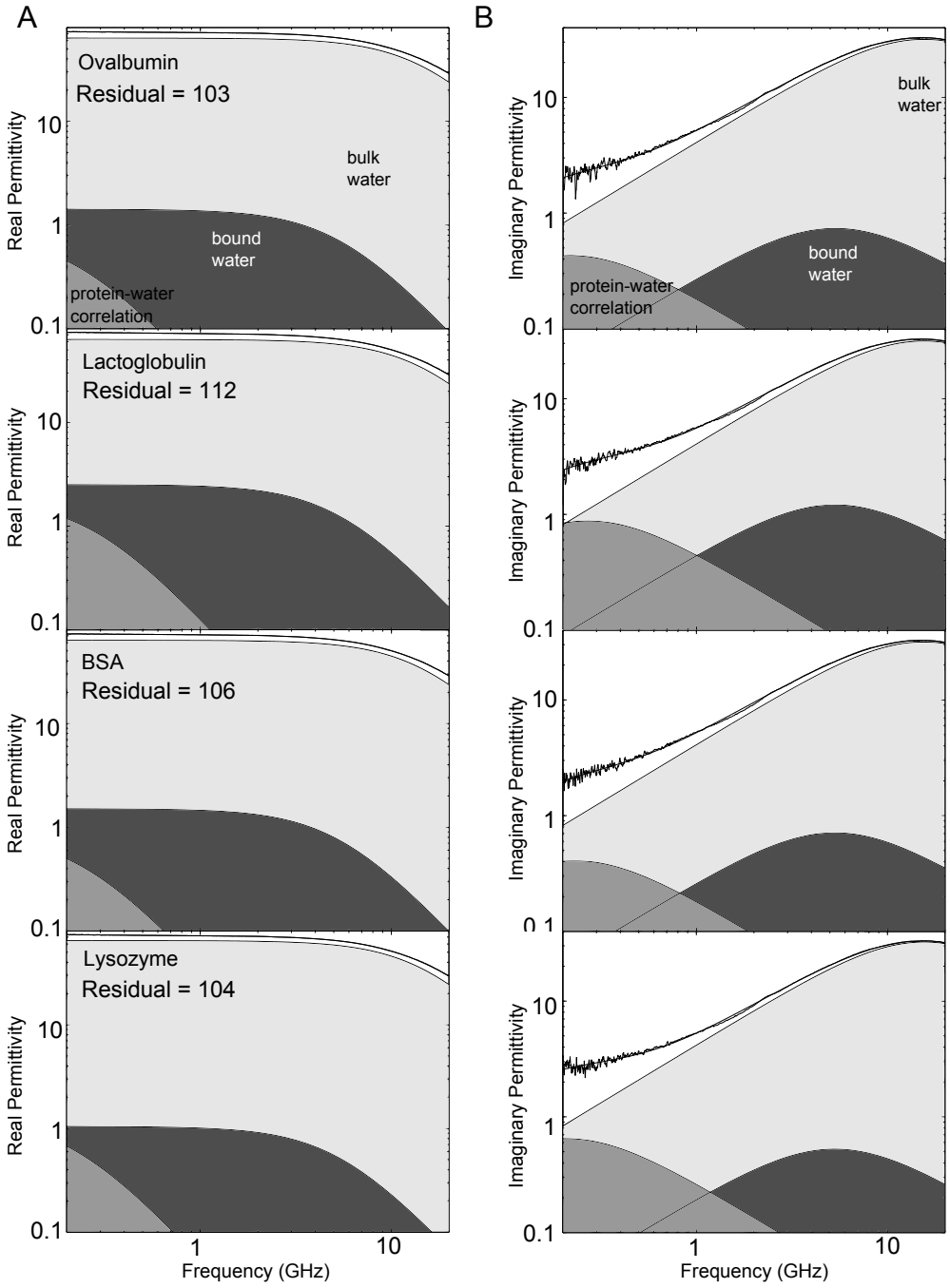


Figure 5.5: Real (A) and imaginary (B) permittivity of ovalbumin, lactoglobulin, BSA and lysozyme aqueous solutions (18 g/dL) fitted with a third order Debye equation. The lowest relaxation feature is attributed to protein relaxation and cross-correlation effects, the second to bound water (hydration shell) and the last to bulk water.

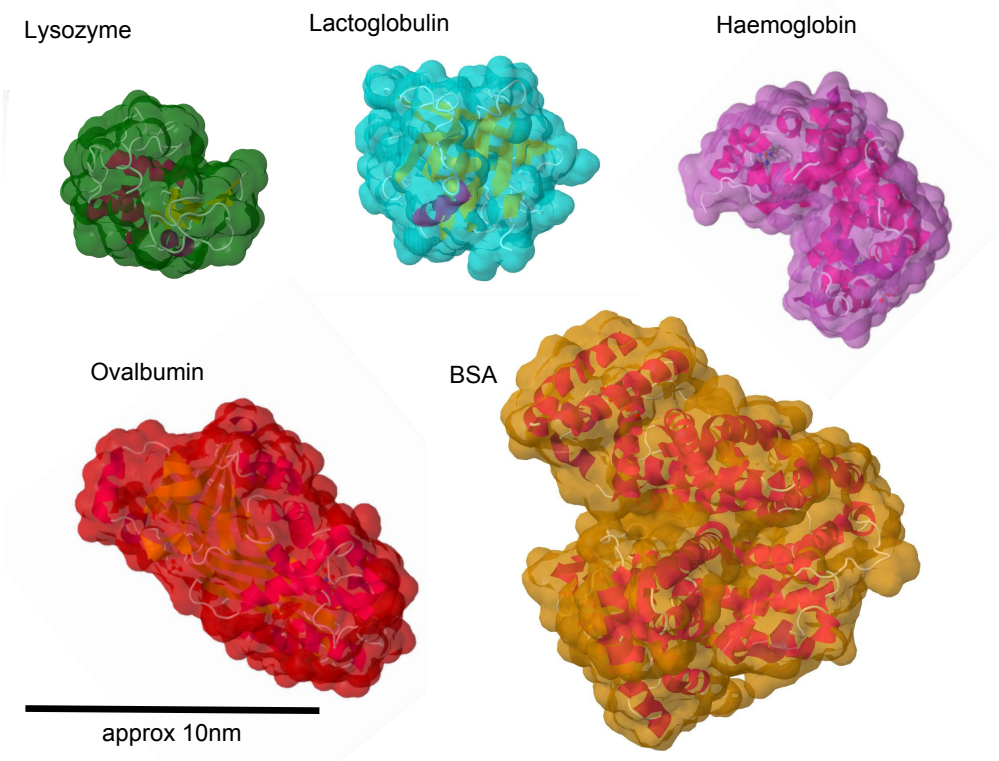


Figure 5.6: Lysozyme, β-lactoglobulin, haemoglobin, ovalbumin and bovine serum albumin (BSA) [100].

reported dielectric response of many globular proteins and their varied spectra a novel approach to protein differentiation using microwave spectroscopy can be established. Variations in the atomic topology and size of the proteins examined (depicted in Fig. 5.6) result in possible differences in relaxations occurring from protein to protein.

Additional measurements were undertaken to confirm the observed differences in the preliminary dielectric findings of the four protein solutions. The four protein solutions at concentrations up to 18 g/dl were analysed between 200 MHz and 20 GHz with a vector network analyser (VNA) using two dielectric probes based on coaxial techniques [41] (Agilent 85070E). Measurements were made in a temperature stable environment of 20 ± 0.5^{o}C with measurements taken within $\pm0.05^{o}$C of each other. The protein powders were dissolved in 5.6 μSm^{-1} water, which, in order to accurately examine and compare all solutions were put through dialysis to match and reduce conductivity.

The dielectric response of the real permittivity of the four proteins at concentrations between 0 g/dl to 18 g/dl is shown in figure 5.7. The deconvolved data (Fig. 5.7) demonstrates the presence of three relaxation processes with a dielectric contribution $\Delta_{1,2,3}$ that is a function of concentration. The highest frequency relaxation process (τ_3 and Δ_3) is attributed to water ($\tau_3 = 9.8\ ps$), the 5 GHz peak (τ_2 and Δ_2) to hydration water ($\tau_2 = 30 - 59\ ps$) and the lowest frequency process (τ_1 and Δ_1) to cross-correlation effects ($\tau_1 = 488 - 708\ ps$) and the tail end of protein reorientational polarisation ($\tau_r = 1\ ns$) (Table 5.1.3).

The difficulty of deconvolving a dielectric spectrum is apparent in figure 5.8 by the scattering of the Debye variables despite constrained limits. The dielectric contribution ($\Delta_{1,2}$) from the relaxation processes of bound water and protein-water cross-correlation is found to be linearly proportional to protein concentration (Fig. 5.8A). Most notably and as observed in the preliminary measurements the dielectric contribution and relaxation time from hydration water is dependent on the protein solution under measurement.

Building upon the observed spectra of the protein solutions, two methods for the differentiation of protein solutions were developed.

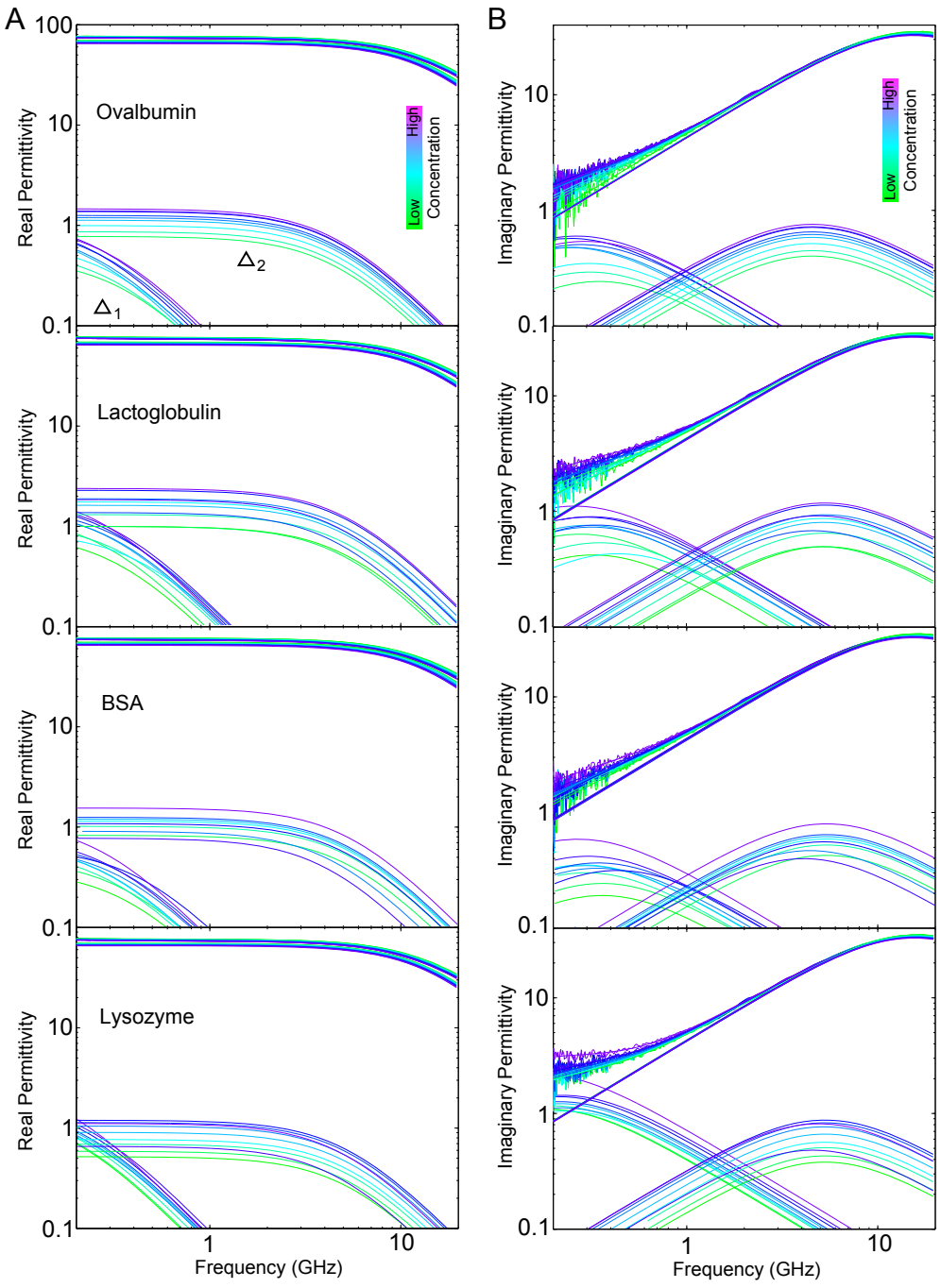


Figure 5.7: The change in the real and imaginary permittivity as a function of protein concentration (0 g/dL to 1.8 g/dL) for ovalbumin, lactoglobulin, BSA and lysozyme (A). Highlighted by the red circle is the apparent shift in the relaxation time with increasing protein concentration (B).

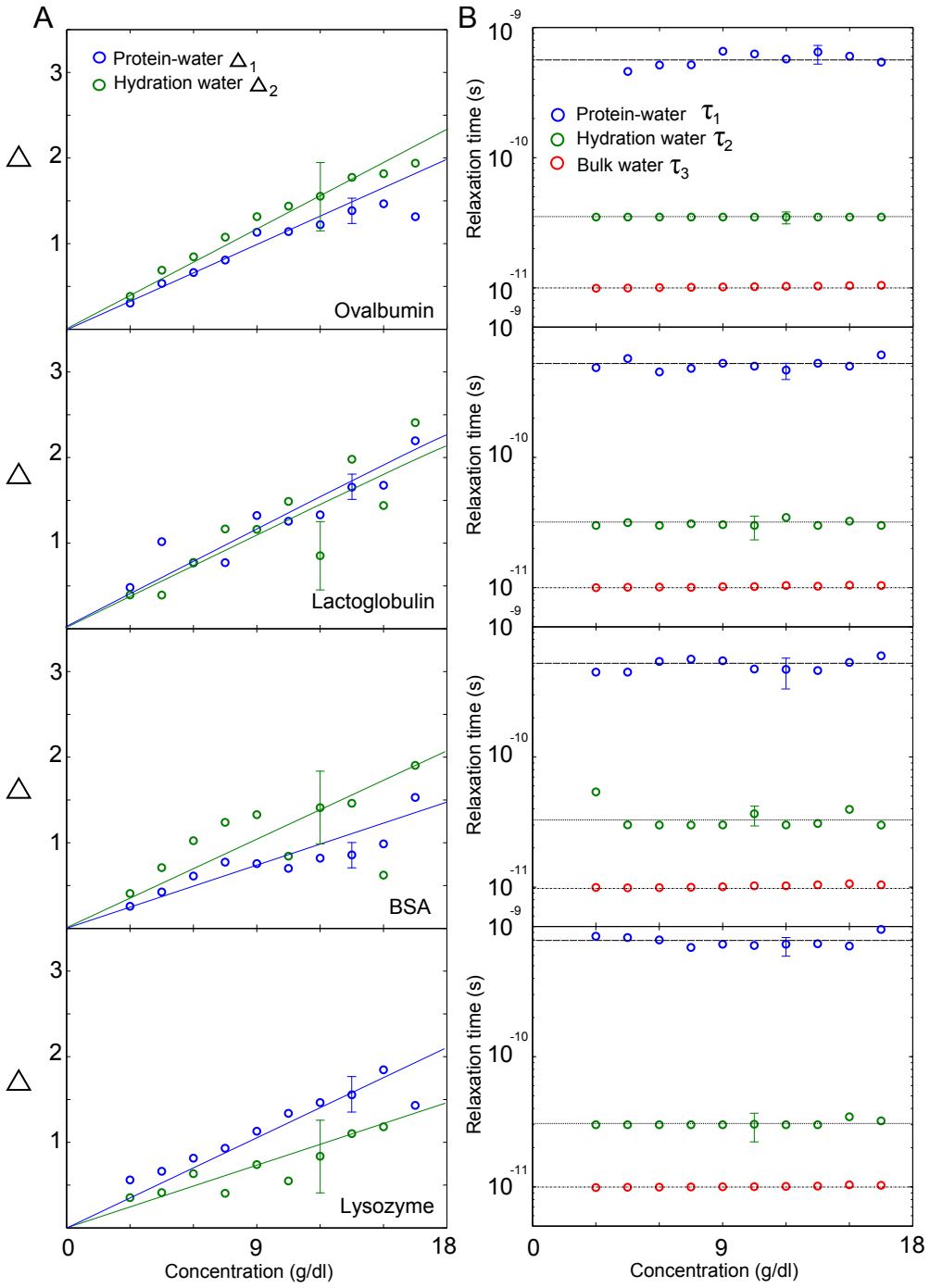


Figure 5.8: The change in the permittivity contributions (A) and relaxation times (B) as a function of protein concentration (0 g/dL to 1.8 g/dL) for ovalbumin, lactoglobulin, BSA and lysozyme. The error values given are calculated using the outlined Jacobian method for parameters in a least-square fitting routine (see Chapter 4 - Data fitting).

Protein	τ_1 (ps)	$\delta\tau_1$ (ps)	τ_2 (ps)	$\delta\tau_2$ (ps)	τ_3 (ps)	$\delta\tau_3$ (ps)
Ovalbumin	532.9	58.9	30.0	4.2	10.1	0.1
Lactoglobulin	550.0	30.2	32.7	4.8	10.1	0.1
BSA	488.3	30.6	30.6	4.2	10.1	0.1
Lysozyme	708.2	56.2	32.2	6.7	10.1	0.1

Table 5.1: The relaxation times and associated uncertainties of the dielectric mechanisms present in proteins solutions in the frequency range of 200 MHz to 20 GHz.

The first technique arose from the measurement and analysis of low concentration solutions ($\phi \leq 2\%$ v/v or 1.6 g/dl). At these low concentration the dielectric effects from hydration water are almost negligible making deconvolution of the data almost impossible. For a solution with solutes present at such low concentrations fitting is achieved using a single Debye relaxation. By analysing the data with a single peak the system under measurement is viewed as a macroscopic system where the properties of the system change as an average of the discrete dielectric mechanisms.

This analysis can be applied as follows; a system comprised of pure water has an inherent viscosity η_0 related to the relaxation time as given in (2.77). With the introduction of a protein to the solution a portion of the bulk water becomes bound thereby altering the mobility and viscosity of that water. The system as a whole can now be said to have an average viscosity η according to the ratio of bound and free water. The relaxation time of the system becomes

$$\tau = \frac{\pi\eta r^3}{k_B T}. \tag{5.8}$$

Einstein's classical analysis of a solution containing solutes gives a system viscosity according to

$$\eta = \eta_0(1 + k\Phi), \tag{5.9}$$

where k is a solute dependent parameter, η_0 the viscosity of water and Φ the volume fraction of the solute. Taking directly from (5.9) and applying it to

our system we can assume that k is related to the mobility (relaxation time) of the hydrated water and hydration number per protein. Consequently the relaxation time becomes

$$\tau = \frac{\pi\eta_0(1 + k\Phi)r^3}{k_B T}. \tag{5.10}$$

Based on fits to the dielectric spectra of the four proteins lactoglobulin, ovalbumin, BSA, lysozyme, sodium chloride and carboxyl terminated nanospheres at concentrations up to 1.5 g/dL reveal that (5.10) is a viable tool to analyse the solution (Fig. 5.9). With increasing concentration the relaxation time is seen to increase as expected from (5.10). In the case of unknown concentrations the static permittivity serves as an accurate value to compare to the relaxation time. At such low concentrations the decrease in the static permittivity is almost entirely effected by the protein concentration according to mixed medium theory (see Mixed media) with bound water playing a negligible role.

The measurement of the change in static permittivity against the change in relaxation time as a ratio can be derived from (5.6) and (5.10) resulting in

$$\frac{\Delta\epsilon}{\Delta\tau} \propto \frac{\epsilon(f)}{k}, \tag{5.11}$$

where $\Delta\epsilon = \epsilon_{meas}/\epsilon_{water} - 1$, $\Delta\tau = \tau_{meas}/\tau_{water} - 1$ and $\epsilon(f) = (\epsilon_{solute} - \epsilon_{water})/(\epsilon_{solute}/2 + \epsilon_{water})$.

From the deconvolution of the data a shift is observed in both the permittivity and relaxation time. Whilst the change in the static permittivity is similar between protein types as a function of concentration (Fig. 5.1 and Fig. 5.10A) the shift in the relaxation time is not (Fig. 5.10A). When compared there are noticeable differences between the ratios of proteins. We can infer from (5.11) that our k parameter must vary from protein to protein. Based upon previous measurements we know that only the high frequency Δ_2 hydration water would contribute to a change in the relaxation time however the given times for the proteins are within a number of picoseconds of each other. This

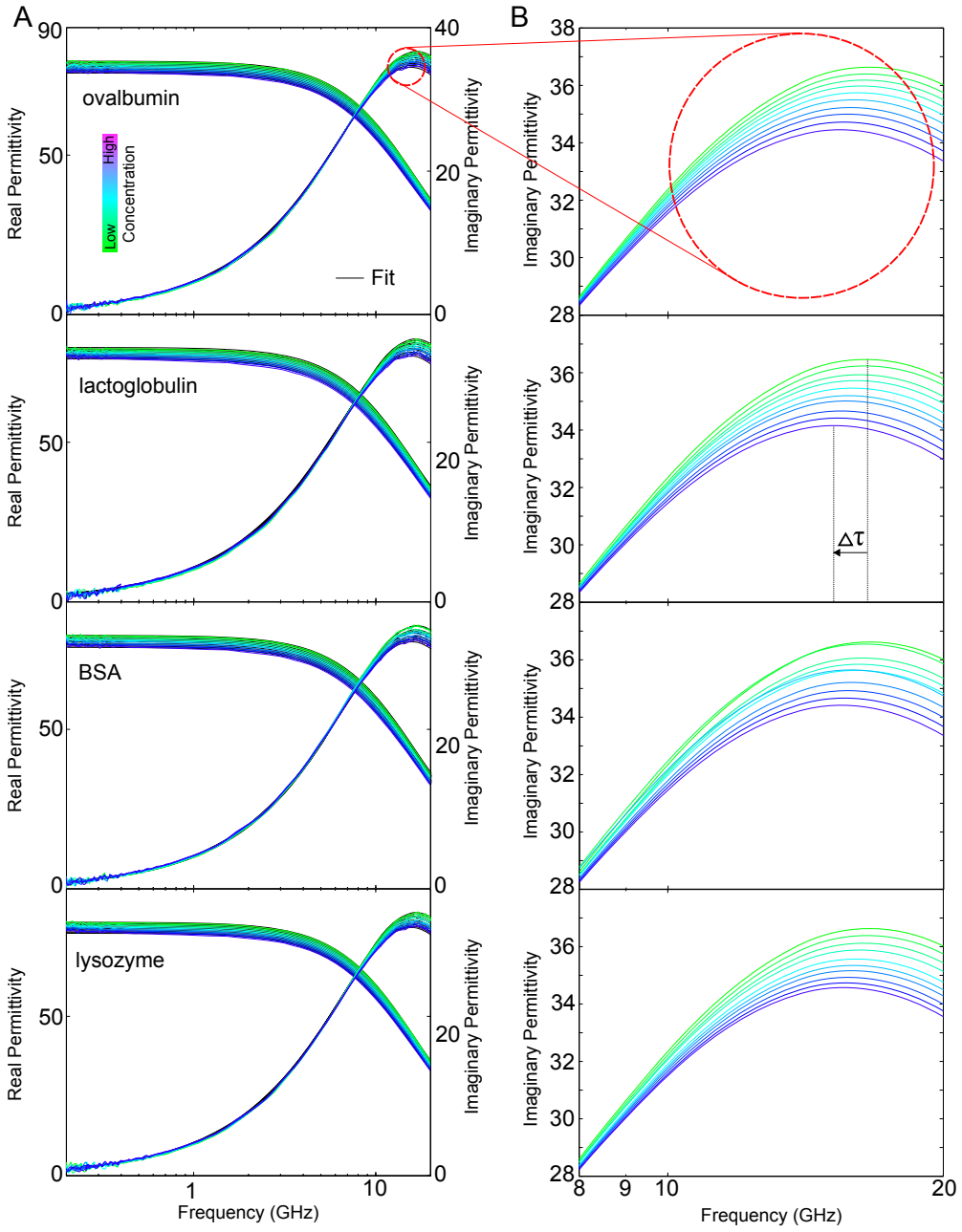


Figure 5.9: The change in complex permittivity as a function of protein concentration ($\leq$ 1.6 g/dL) (A). The ratio of the response as a function of ellipticity (B) [101].

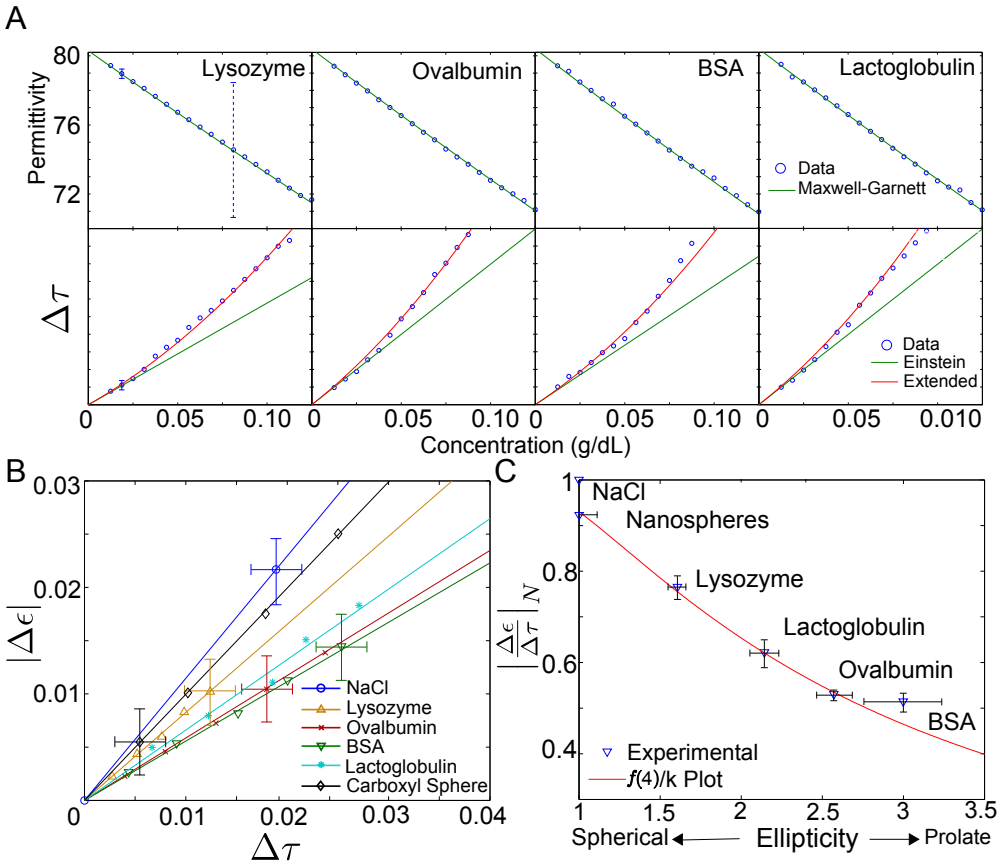


Figure 5.10: The change in the permittivity and relaxation time as a function of protein concentration using a single Debye model fit (A). Two error bars are given, the first solid error bars are given based on the error calculated in the fitted parameters and the second dashed error bar highlights the accuracy given of absolute permittivity value. By normalising all further measurements against the permittivity of water the system no longer relies on the absolute values but on relative change. The change in permittivity as a function of change in relaxation time with respect to protein concentration (B). Errors given are from the calculated error in the fitted parameters. The normalised ratio of the change in permittivity and relaxation time as a function of ellipticity (C) [101]. The errors in the ratio are based on the standard deviation from the best fit and the errors in ellipticity are calculated from the possible radii of the proteins (Fig. 5.6).

leaves the hydration number per protein as the protein-dependent variable.

Protein	Ratio	δ
Ovalbumin	0.17	0.01
Lactoglobulin	0.62	0.03
BSA	0.51	0.02
Lysozyme	0.77	0.02

Table 5.2: The ratio values and uncertainties calculated from the standard deviation of the data as shown in figure 5.10B,C.

By studying the atomic structure of the proteins (Fig. 5.6) our findings suggest that as the proteins become more elliptical there is a greater shift in the relaxation time due to an increased surface area to volume ratio and therefore a greater number of hydrated water molecules per protein [101] (Table 5.1.3). With increasing concentration the quality of the fit is reduced and at concentrations above 1.6 g/dL we have deemed this technique inaccurate primarily due to the determination of the static permittivity. At concentrations below this mark the outlined technique has been outlined as a means to distinguishing proteins based upon their ellipticity. Further tests and measurements across different devices would be required to validate the accuracy of this technique and real-world applicability.

The second method utilises the response of low and high frequency permittivity with respect to an increasing protein concentration. As the concentration of proteins increases the permittivity decreases according to mixed-medium theory. However, as the protein concentration increases so do the number of bound water molecules and cross-correlation events between water and proteins. This further reduces the permittivity at frequencies above the relaxation time of those dielectric mechanisms. The change in low frequency (ω_1) permittivity as a ratio to high frequency (ω_2) permittivity can be approximated to be

$$\frac{\epsilon(\omega_1)}{\epsilon(\omega_2)} = \frac{\Delta_1(\Phi) + \Delta_2(\Phi) + \Delta_3(\Phi)}{\alpha\Delta_3(\Phi)}, \tag{5.12}$$

where $\alpha = [1 + (\omega_2\tau)^2]^{-1}$. The ratio of (5.12) is therefore highly dependent

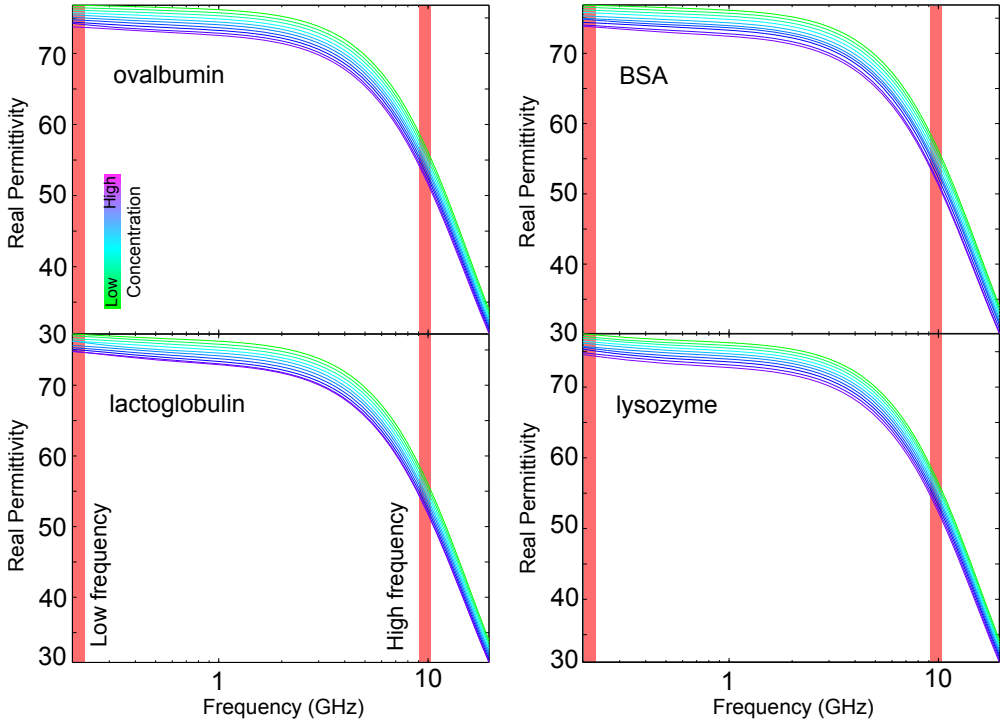


Figure 5.11: The real permittivity as a function of frequency for the four aqueous protein solutions of interest marked with the chosen frequencies for the comparison of permittivities.

on the magnitude of the dielectric contribution from hydration water and correlation effects as a function of concentration.

The low frequency permittivity was chosen at the limit of our frequency range (200 MHz) and the higher frequency permittivity to be around 9 GHz (Fig. 5.11 (red line)) so as to avoid influence from the tail-end of the low frequency relaxations though still low enough so that the change in permittivity is appreciable as a function of protein concentration. Analysis was conducted on the proteins lactoglobulin, ovalbumin, BSA and lysozyme up to concentrations of 18 g/dL.

The values show a larger change in the high frequency permittivity in comparison to the low frequency. This is in accordance with mixed media theory (lower permittivity contrast between proteins and water at higher frequencies) and partially to bound water no longer contributing to the high frequency dielectric response. Further still, we observe variations in the ratio for the

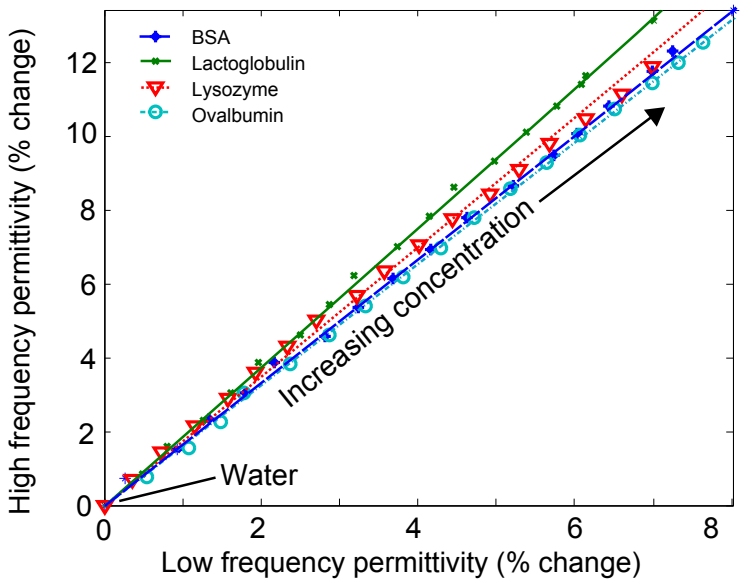


Figure 5.12: The change in high frequency permittivity verses low frequency permittivity of four aqueous protein solutions as a function of concentration [102].

different proteins (Table 5.1.3). The difference in the values predominantly arises from a combination of both bound water and cross-correlation effects ($\Delta_1 + \Delta_2$). This also proves to be detrimental as the addition of the two systems shows less difference between the proteins than a single system (Fig. 5.8). There are also possible effects owing to differences in the rate of change between high and low frequency permittivity with respect to protein permittivity though it is likely to be small compared to the contribution from the dielectric mechanisms.

Protein	Ratio	δ
Ovalbumin	1.70	0.08
Lactoglobulin	1.96	0.05
BSA	1.75	0.11
Lysozyme	1.84	0.21

Table 5.3: The ratio values and uncertainties calculated from the standard deviation of the data as shown in figure 5.12.

The analysis of protein solutions have highlighted that variations in the bound water and relaxation dynamics of various proteins exist. Such difference can

subsequently be used for the differentiation of protein solutions based on the outlined techniques and ratios to produce a finger-printing method for future concentration independent identification [102]. The latter technique is well suited to resonant methods and may find use in applications such as chromatography as an analysis tool for the identification of proteins as they are separated.

5.2 Dielectric response of cell solutions

Having studied the dielectric response of proteins the next intuitive step is to follow nature's evolution and to examine cells. As the smallest object regarded as living, cells serve highly functional purposes and can be composed of a wide range of constituents depending on their function. For almost all cases a cell is enclosed by a bilayer lipid membrane built from phospholipids and often interspersed with protein channels. Their purpose as a protective barrier between the internal constituents and the exterior environment enables selective transport of important molecules and proteins to the interior. The interior environment is often regulated and has markedly different properties to the exterior for which the cell membrane is vital. Mammalian blood cells may vary dramatically depending on their purpose; red blood cells are anucleate but are filled with a large concentration of Hgb (32-36 g/dl), white blood cells such as lymphocyte are composed almost entirely of a nucleus containing negligible levels of cytoplasm and platelets are the product of megakaryocte cells. Interestingly it is the thin membranes of the cells that contributes the most significant portion of the dielectric response of a solution of cells across much of the radio frequency (kHz to MHz).

5.2.1 Looyenga polarisation

The complex dielectric properties of electrolyte solutions containing cells or other thin interfaces from single Hertz to terahertz frequencies are primarily governed by three features: electrolyte concentration (conductivity), mem-

branes or thin interfaces (Maxwell-Wagner/Looyenga polarization) and water molecules (rotational polarisation). The conductivity and polar contributions of liquids are well understood and have been covered in some detail (see Chapter 2) however the effects of thin interfaces have not been discussed. In solutions such as blood this is a prominent dielectric feature that should be addressed.

In the presence of an electric field charge accumulation occurs when an interface prevents the motion of any free ions. The small separation of electrolytes leads to strong capacitive effects across the cell membrane leading to a high polarisation (Fig. 5.13).

For the particular case of erythrocytes (red blood cells) a range of theoretical models have been developed and compared [103, 104, 105, 106]. The findings of Bordi et al. [106] suggest that the most accurate description of the dielectric features of a cell in an electrolyte solution can be given by the Looyenga polarisation [104] where the permittivity is described as

$$\epsilon^*(\omega) = \left[\Phi\left(\epsilon_{cell}^{*1/3}(\omega) - \epsilon_{out}^{*1/3}(\omega)\right) + \epsilon_{out}^{*1/3}(\omega)\right]^3. \tag{5.13}$$

Φ is the fractional volume occupation of the cells. The permittivity constituents are,

$$\epsilon_{out}^* = \epsilon_{out} + \frac{i\sigma_{out}}{\epsilon_0\omega}, \tag{5.14}$$

where ϵ_{out}^* is the permittivity of the medium outside of the cell, σ_{out}^* the conductivity outside the cell and ϵ_{cell}^* the mixed medium (5.5) permittivity of the cell,

$$\epsilon_{cell}^* = \epsilon_{memb}\left[1 + \frac{\Phi(\epsilon_{in}^* - \epsilon_{memb}^*)}{\epsilon_{memb}^* + A(1-\Phi)(\epsilon_{in}^* - \epsilon_{memb}^*)}\right], \tag{5.15}$$

with A the depolarisation factor and Φ the volume fraction occupation of the

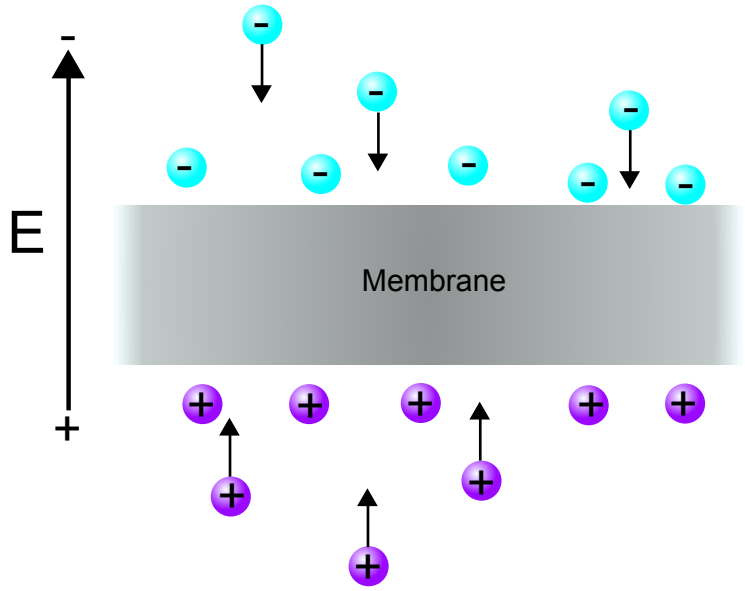


Figure 5.13: The response of ions either side of a thin membrane in solution.

fluid inside the cell,

$$\Phi = \frac{(a_0 - d)(b_0 - d)(c_0 - d)}{a_0 b_0 c_0}, \tag{5.16}$$

where a_0, b_0, c_0 are the ellipsoid dimensions and d the thickness of the membrane. The permittivity terms in (5.15) are given by

$$\epsilon^*_{memb} = \epsilon_{memb}, \tag{5.17}$$

$$\epsilon^*_{in} = \epsilon_{in} + \frac{i\sigma_{in}}{\epsilon_0 \omega}, \tag{5.18}$$

where ϵ^*_{memb} is the membrane permittivity and ϵ^*_{in} the permittivity of the electrolyte fluid inside the cell. A range of solutions to the depolarisation factor A for varying dimensions can be found in ref. [103] though for an oblate spheroid ($a_0 b_0 = c_0$) the solution is

$$A = \frac{1}{2} - \frac{1}{1-u^2} - \frac{u}{1-u^2} \arccos u, \tag{5.19}$$

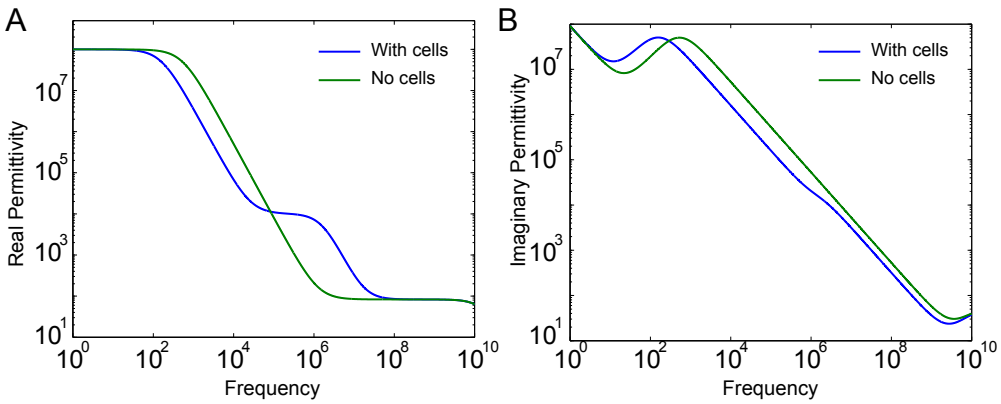


Figure 5.14: A theoretical real (A) and imaginary (B) permittivity plot demonstrating the impact of Looyenga polarisation in a cell solution.

where $u = a_0/b_0$.

At typical electrolyte concentrations (0.9 g/dL) present in solutions such as blood, the Looyenga polarisation effects have a relaxation around single MHz frequencies that becomes negligible around GHz frequencies (Fig. 5.14).

This effect has been proposed for the determination of RBC concentration and singe cell size analysis [107, 108] similar to the low frequency methods currently employed in gold standard techniques [109]. The standard technique involves the measurement of the direct current between two electrodes. In a serum solution electrolytes are unimpeded and migrate freely towards the electrodes. The introduction of cells hinder the migration of electrolytes and lead to charge build up on the cells membranes. The change in the conductivity of the solution has been found to be correlated directly to the total cells count.

5.2.2 High frequency dielectric response of blood

Above frequencies where the Looyenga polarisation plays a dominant role and according to (5.5) the primary contributors to the complex dielectric response at microwave frequencies relate strongly to the solutes and solutions that occupy the greatest volume. Water is well known to make up 75 % of whole blood though Hgb is the most abundant organic component in

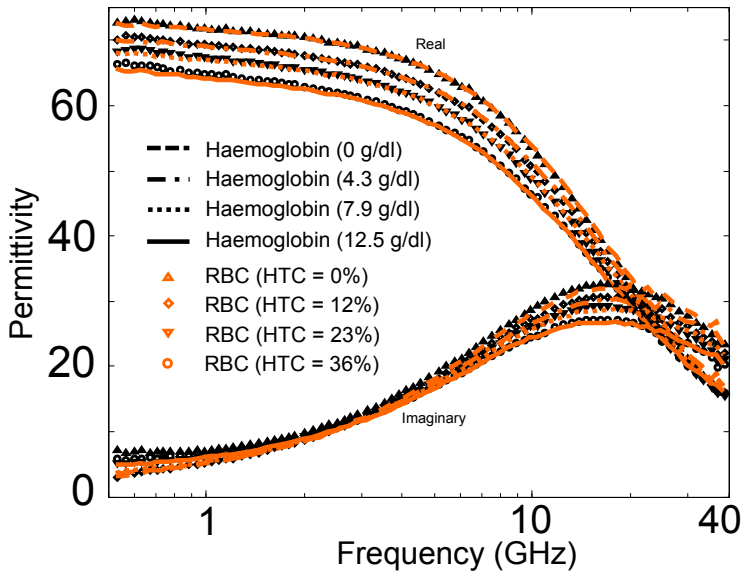


Figure 5.15: The high frequency (500 MHz to 40 GHz) dielectric response of serum with varied Hgb and RBC concentrations.

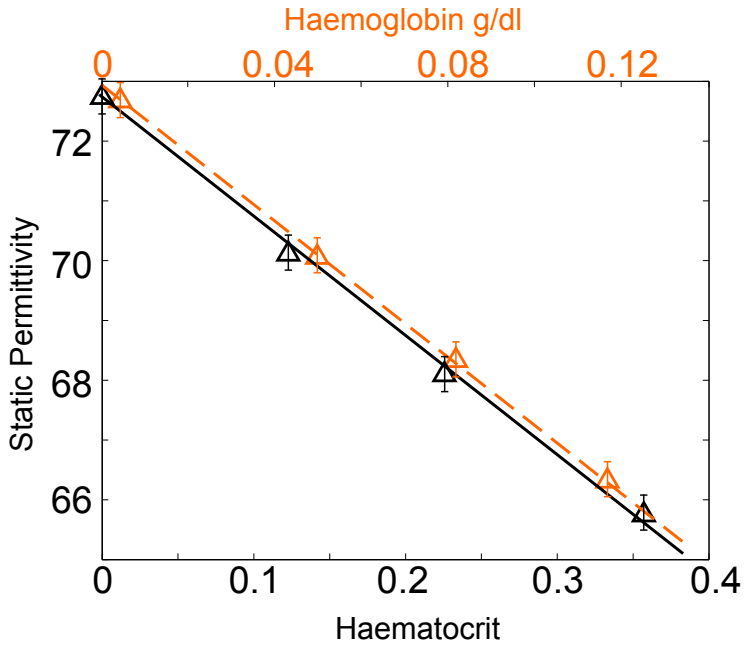


Figure 5.16: The change in real permittivity at 2 GHz as a function of Hgb and RBC concentration.

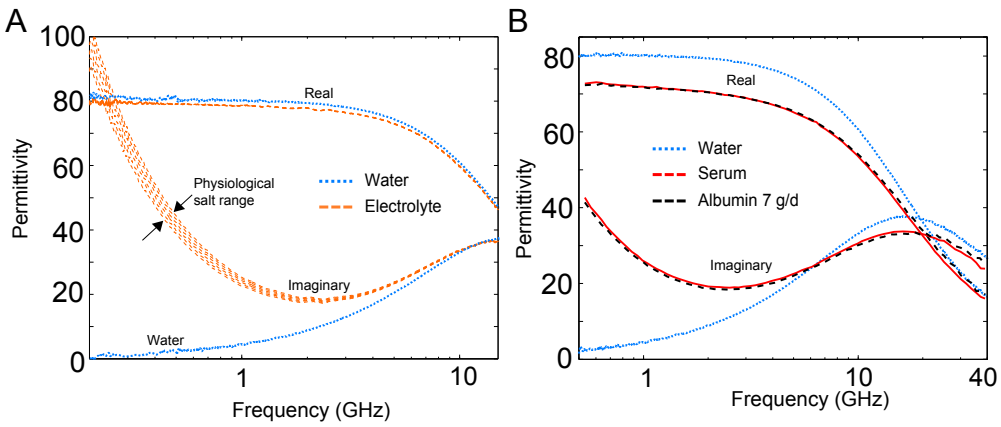


Figure 5.17: The high frequency (200 MHz to 20 GHz) complex permittivity of water compared against water samples containing electrolyte levels equivalent to those found across healthy individuals (A). The complex permittivity (500 MHz to 40 GHz) of water, serum and a water solution with matching electrolyte levels and approximately 7 g/dL of albumin protein (B).

blood (approx. 15 g/dl) followed by serum proteins, of which albumin and immunoglobulin are the most substantial (approx. 7 g/dl). The remaining volume is comprised of electrolytes, white blood cells and platelets. The dielectric response of whole blood is therefore highly sensitive to variations in haemoglobin, serum protein and electrolyte concentration. Electrolyte and Looyenga polarisation dominates the dielectric response up to the MHz regime only becoming negligible around 3 GHz.

To determine the microwave dielectric response of the various constituents of whole blood, measurements were made on a range of concentrations of RBCs, electrolytes, serum proteins, and haemoglobin concentrations in water or serum. Dielectric spectroscopy was carried out using a vector network analyser (VNA [HP 8722ET]) with a commercially available dielectric probe (Agilent probe kit) between the frequencies of 200 MHz and 40 GHz (see Chapter 3). A systematic study was designed to examine the most abundant organic components in whole blood.

The impact of serum proteins dissolved in water was examined by dissolving albumin proteins in water with physiological electrolyte levels and comparing to serum. Lyophised albumin was dissolved in an electrolyte containing 240 mmol/L sodium chloride and compared to a sample of serum centrifuged

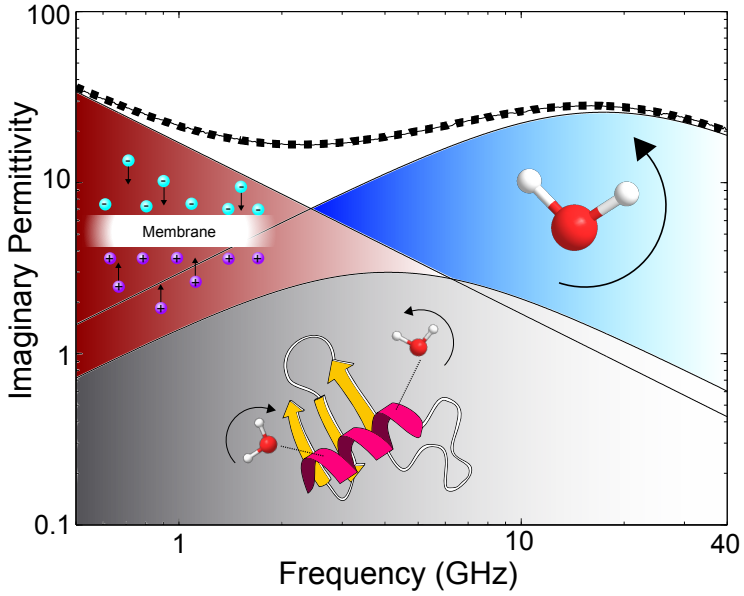


Figure 5.18: The high frequency (500 MHz to 40 GHz) imaginary permittivity of whole blood demonstrating the contributing processes to the dielectric spectrum: conductivity and Looyenga polarisation, hydration water and bulk water.

from whole blood. The dielectric properties were compared and the protein concentration increased until a matched dielectric spectrum was achieved. At a concentration of 6.8 g/dL the spectrum was found to match that of serum (Fig. 5.17B). By centrifuging the serum at 10,000 rpm for 15 minutes the proteins were separated from the serum. By measuring the volume fraction occupation of the serum and assuming a density of 1,350 kg/m^3 the serum concentration was calculated to be approximately 6.5 g/dL. This finding demonstrated that the dielectric response of serum is primarily governed by serum proteins and electrolyte concentration.

The dielectric response of electrolytes in water and at lowered and elevated physiological levels (200 - 280 mmol/L sodium chloride) was explored with six samples. Appreciable change to the conductivity was apparent up to 9 GHz with no change observed in the real permittivity. Compared to deionised water there is a reduction to the static permittivity of approximately two at physiological salt levels.

To confirm that haemoglobin plays an important role in the high frequency

dielectric response of blood, RBCs in serum and haemoglobin proteins suspended in the same serum were compared. As revealed by figure 5.15, a clear correlation was identified, in agreement with trends observed by Wolf et al. [110], between the reduction in permittivity and an increase in RBC concentration. The absolute values states on permittivity differs between our values (HCT 0.4 - $\epsilon = 57 \pm 4.2$) and Wolf et al. (HCT 0.4 - $\epsilon = 55$). The difference in values is likely to arise from the different fitting models used, Wolf et al. implemented a Cole-Cole fit where as the model used for our analysis was a second order Debye model that assumes the presence of bound water. Further to these findings, we observe the same dielectric response for haemoglobin concentrations in serum with concentrations equivalent to a 0.33% volume occupation of RBCs. A small deviation in the real permittivity ($\Delta\epsilon_r = 1.35$ at 200 MHz) is observable between higher concentrations of haemoglobin and RBC samples from 500 MHz to 2 GHz which we attribute to the tail-end of the Maxwell-Wagner/Looyenga relaxation response in RBCs.

Based on the statistical analysis (see Chapter 3) the need to fit a third-order Debye equation to explain the data was discovered. In addition to the expected low frequency polarisation relaxation processes and bulk water relaxation there is also a 40 ps relaxation observed. This is attributed to hydration water, in keeping with previous findings and contrary to findings by Wolf et al. who used only a Cole-Cole fit over the frequency range of interest (Fig. 5.18).

The high permittivity contrast between water and organic molecules makes the frequency range below 15 GHz preferable for haemoglobin and serum protein analysis. Additionally, the effects of Maxwell-Wagner polarization and losses from electrolytes make frequencies below 2 GHz unsuitable for protein measurements. This narrow frequency range presents a unique window to analyse organic solutes in blood that may otherwise be obscured or invisible at other frequency ranges.

5.3 Summary

The complex permittivity of proteins in water were shown for four common globular proteins at concentrations between 0 and 18 g/dL. Based on statistical analysis the results confirmed the presence of three concentration dependent relaxation features that are attributed to complex water-protein interactions (cross-correlation), hydration water and bulk water.

The concentration dependent response is found to be dependent on the proteins examined and was utilised to develop two methodologies for differentiating protein solutions. The first analysis technique was based on broadband spectroscopy and the treatment of the solution as a single dielectric mechanism at low concentrations. The results demonstrated that pure protein solutions may be differentiated by the hydration water surrounding them. The second method used two frequencies at 200 MHz and 9 GHz to differentiate proteins based on the difference in the contribution of hydration water to the permittivity at the respective frequencies. The findings were less conclusive than the previous technique though differences in the ratio of permittivities between the proteins were observed. The use of both hydration water and cross-correlation effects in the analysis proved to be similar between proteins unlike the effect of a single mechanism.

Lastly, the examination of whole blood and the study of the dielectric contributions from its major constituents revealed the importance of Hgb, serum proteins and ionic concentration. A method for the determination of Hgb levels is proposed based on the comparison of whole blood and serum as well the means to calculate the total serum protein levels and electrolyte concentration by comparison of pure water and serum. These methods will be exploited in the next chapter to develop a novel haematological microwave biosensor.

Chapter 6

Blood analysis with a microwave dielectric resonator

The frequency window identified in Chapter 4 in which the dielectric response of whole blood is primarily governed by the haemoglobin (Hgb) concentration offers a unique opportunity to create a device capable of Hgb concentration measurements. In this chapter a device to conduct low volume measurements on blood is developed using a dielectric microwave resonator and a microfluidic system. The result is the first non-optical means to determine Hgb concentration with accuracies equivalent to commercial systems.

6.1 Haemoglobin

Almost every living cell in the human body requires oxygen to support and sustain cell metabolism and it is therefore vital that oxygen is able to reach all of the extremities of the human body. After the initial diffusion from the lungs into red blood cells most oxygen molecules are bound to Hgb thereby liberating hydrogen ions from around the heme component of the protein (Fig. 6.1). The concentration of hydrogen ions plays an important role in the binding and liberation of an oxygen molecule from Hgb described by the Bohr effect [111]. A lower concentration in the blood at the lungs allows

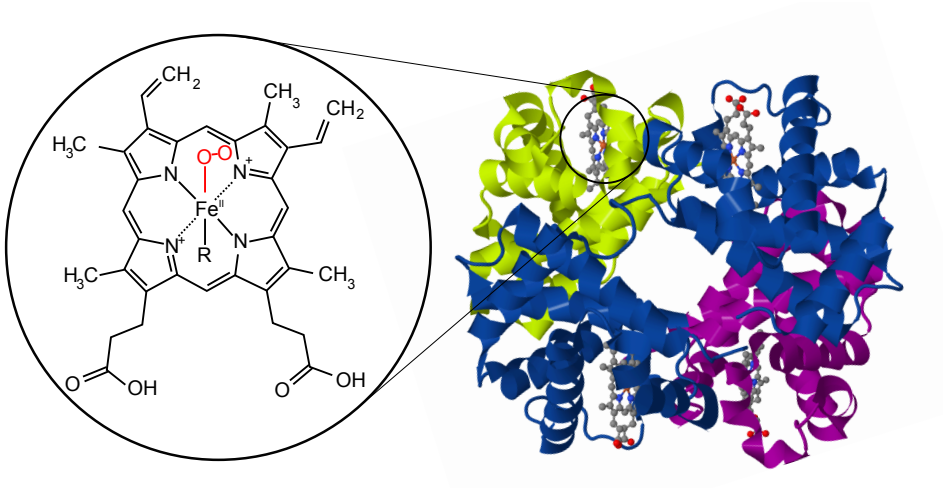


Figure 6.1: A haemoglobin protein containing four heme complexes (inset).

oxygen to bind to Hgb and an elevated concentration of hydrogen ions at the cells liberate the oxygen. Hgb also acts to remove 10% of the carbon dioxide produced as a by-product of metabolism [112].

As mentioned in Chapter 5 a protein can comprise of primary, secondary and tertiary structures. In the case of Hgb four sub-units, each a tertiary structure are bound by electrostatic interactions (hydrogen bonds). Each sub-unit is capable of carrying a single oxygen or carbon dioxide molecule within its heme component therefore allowing Hgb to carry up to four molecules in total.

Owing to the conformational changes induced by bound oxygen, carbon, or no molecule [113] to the iron centre of the heme component the various forms of Hgb such as oxyhaemoglobin, carbaminohaemoglobin, carboxyhaemoglobin and deoxygenated Hgb all exhibit unique spectral features that form the basis of optical Hgb and oxygenation concentration measurements [114, 115, 116]. All modern Hgb measurement techniques use the magnitude of absorption at one or more frequency in the visible or near-infrared spectrum on a sample that has had the RBCs lysed. Owing to the 10 μm size of red blood cells light is unable to penetrate the cell and scatters. Subsequently the destruction of the cell membrane is vital for accurate optical measurements.

The typical lifetime of a Hgb protein is similar to that of a red blood cell; approximately 100 to 120 days. Hgb is broken down alongside red blood cells

resulting in the production of bilirubin which is removed in urine, carbon monoxide and the recycling of the iron atom. Changes to Hgb production, breakdown or function can contribute to a number of haematological diseases and is often a side effect in chronic disorders [117] with many resultant symptoms due to changes in the rate of oxygen transport and supply. Anaemia is the most common blood disorder of which up to a quarter of the worlds population is believed to have [118].

6.1.1 Anaemia

Hgb concentration is typically given in terms of the mass of Hgb (in grams, g) per decilitre (dL) that for healthy individuals is in the range of 13-18 g/dL for men and 12-15 g/dL (11-14 g/dL pregnant) for women. An individual with a concentration lower than this is regarded as being anaemic and above as polycythemic. Severe anaemia is a Hgb concentration lower than 5 g/dL. Anaemia is commonly classified into three main categories: macrocytic anaemia, normocytic anaemia and microcytic anaemia of which there are a many subclasses [119].

The three main classifications of anaemia allow for improved treatment and narrow down the cause of the disorder however anaemia can occur in one of three ways.

Haemolytic anaemia arises in diseases that induce the abnormal breakdown of RBCs known as haemolysis. The causes for increased RBC breakdown are wide and varied from enzyme deficiencies to sickle cell [120]. The breakdown of RBCs releases Hgb into the blood stream resulting in visual symptoms such as jaundice and the break down and production of excess bilirubin. Symptoms of haemolytic anaemia are a shortness of breath, jaundice and fatigue.

Large amounts of blood loss induces anaemia shortly and temporarily after trauma events or gradually increase in severity with certain cancers or ulcers that lead to internal bleeding in the digestive tract [121].

Impairment or dysfunctional production of Hgb or RBCs is a common result

of insufficient nutrition, most commonly iron. Additional causes may arise from conditions such as sickle cell or vitamin deficiency (vitamin B-12 or folate (B-9)). In pregnancy, levels of vitamin B-12 and folate are affected and often result in anaemia in pregnant women [122, 123].

Whilst anaemia occur in only one of three ways from the point of view of medical diagnosis it is advantageous to know additional haematological parameters such as red blood cell size and reticulocyte count (new red blood cells) and to classify anaemia based on their properties.

The impaired production of RBCs often results in macrocytosis, large than average RBCs [124]. Reductions in Hgb production often owing to dietary-induced deficiencies or liver disease results in anaemia. In conjunction with an increased mean-cellular-volume of erythrocytes (RBCs) the anaemic condition is classified as macocytic.

Normocytic anaemia covers all cases of anaemia in which the topology of erythrocytes remain unaffected and only a reduced haematocrit or Hgb level is recorded [125]. This is the most abundant case of anaemia and the causes can range from simple cases such as pregnancy or the abnormal breakdown of RBCs.

Iron deficiency, commonly dietary related or induced by excess bleeding, results in the insufficient production of RBCs and Hgb. Subsequently, the body replenishes blood with microcytic cells that are smaller than average and carry a reduced Hgb concentration. This case of anaemia is known as microcytic or hypochromic anaemia [126].

Some of the most common causes and diseases related to anaemia are:

- Iron deficiency
- Vitamin deficiency
- Chronic diseases
  - Cancers
  - Autoimmune

  - Hepatitis C
  - Heart failure
  - Kidney
  - HIV/AIDS
  - Malaria
- Sickle cell
- Trauma
  - Surgery
  - Injury
- Treatments
  - Hepatitis C - ribavirin and interferon
  - HIV/AIDS - anti-retroviral
  - phenytoin, methotrexate, azathioprine,procainamide, quinidine, aspirin, warfarin, clopidogrel, heparin

6.2 Microwave dielectric resonator

Having outlined in Chapter 4 that the dielectric response of whole blood when compared to serum is proportional to the Hgb concentration a technical approach was designed to advance the finding towards a practical solution for Hgb measurements. The requirements of a practical device that is capable of determining Hgb concentration is one that uses small sample volumes (μL), has a rapid analysis time (order of seconds) and is accurate ($\pm$0.5 g/dl). As discussed in Chapter 3 dielectric resonators are well established scientific research instruments for sensitive dielectric measurements and are capable of meeting the outlined criteria. Resonators have been used for the dielectric study of blood, however, the findings and applications of such devices have not been clinically significant [127, 128]. The ability to measure samples on

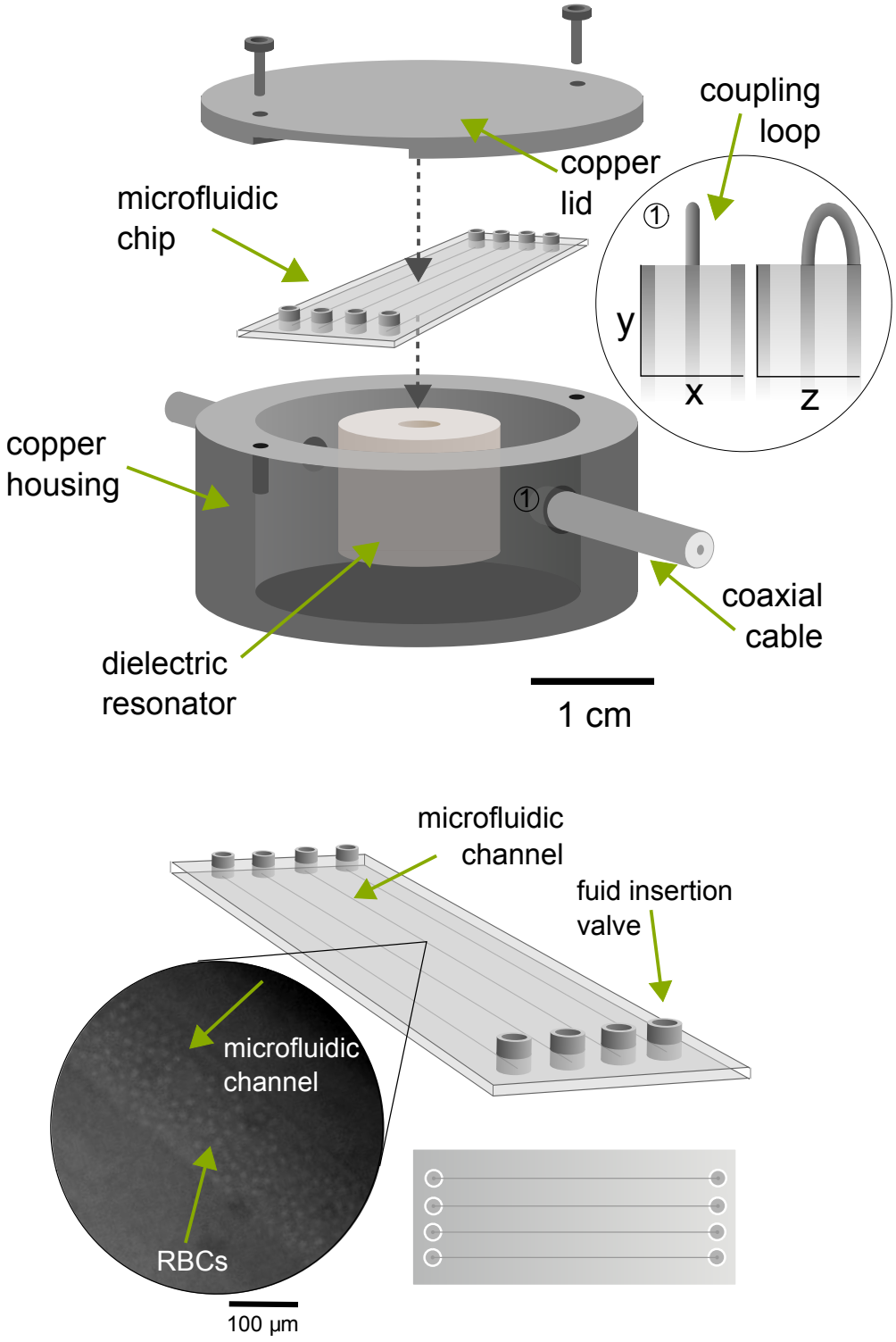


Figure 6.2: The dielectric resonator implemented for low volume liquid measurements. Comprising of a high permittivity BZT puck in a copper housing with integrated microfluidic channel the device is able to conduct dielectric measurements on 500 nL liquid volumes.

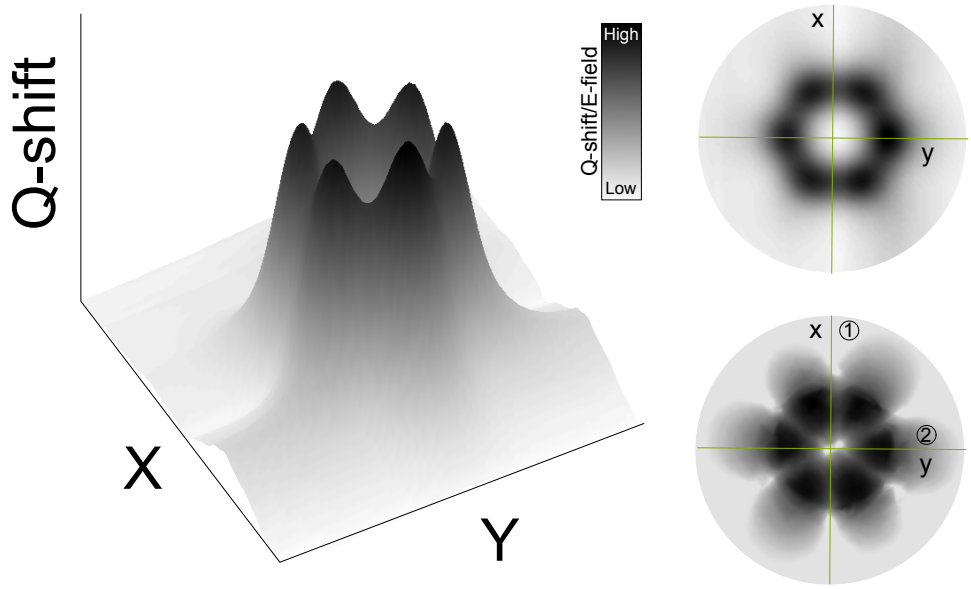


Figure 6.3: Field mapping of the surface of the resonator to confirm correct modal excitation. CST modelled field distributions (inset).

the microlitre level is ideal for utilising finger prick techniques and thereby making measurements minimally invasive.

A modelling approach was adopted using CST Microwave Studio for the design of a resonant system between 2 and 10 GHz based on a dielectric resonator. The resonator design chosen comprises of a high permittivity cylindrical dielectric puck with a diameter of 14 mm and a fundamental TE_{01} mode at approximately 4.4 GHz. Made from barium zirconium titanate (BZT) ($\epsilon = 28$) it is mounted on a teflon support that is contained within a pure copper housing (Fig. 6.2). Coupling is achieved using two coaxial cables with coupling loops providing the means for excitation and measurement of the resonant modes within the dielectric puck (Fig. 6.2). In choosing a mode for the dielectric measurements it is vital to achieve a high concentration of electric fields at the measurement interface of the dielectric puck for which the EH_{603} mode was found to be well suited at 9.4 GHz.

To experimentally locate the resonant mode an experimental field mapping technique was developed by rastering a high permittivity, high loss probe across the surface of the resonator. At high electric field intensities the reso-

nance undergoes a higher perturbation (see Chapter 3) and thus by measuring the Q as a function of probe position we were able to catalogue the resonant mode based on the inferred field distribution (Fig. 6.3).

Coupling optimisation was achieved by manual positioning of the coupling loops to produce a single-peak, symmetric Lorentzian resonant curve. The resonator design allows operation in an open or closed lid configuration with the resonant parameters in an open configuration given to be Q=8000, f=9.4 GHz and in a closed configuration Q=14,000, f=9.41 GHz (simulation Q=15,200, f=9.35 GHz). Fitting to the S_{21} resonant distribution for obtaining Q and f was conducted using a custom made algorithm that implements both phase and amplitude information ([129]).

The accurate measurement and comparison of the dielectric properties of a range of liquids in the immediate vicinity of a resonator requires that the liquids are tightly constrained in volume. The easiest way to achieve this is by a reservoir, capillary or microfluidic channel which prove advantageous in handling small volumes.

6.2.1 Microfluidic integration

Having already revolutionised the world of printing, microfluidic developments have begun to slowly advance analysis and diagnostic techniques in the biomedical world [130]. The advantage of microfluidic systems for the biosensing community lies in the ability to deliver, redistribute and sort low volumes of aqueous solutions and solutes with minimal losses to the sample volume. For the purpose of dielectric measurements a microfluidic systems provides the means to both deliver and remove a sample with no user interaction and within a fixed volume.

For the purpose of the resonant measurements a microfluidic chip made from low-loss plastic (Zeonex ([131])) provided by Microfluidic Chip Shop was integrated above the dielectric puck with four channels of 200 μm diameter. The choice of microfluidic positioning and channel was optimized to obtain the largest reduction in Q with deionized water. Figure 6.4 depicts the electric

field pattern with and without water in a channel, respectively. Resonant measurements are given in terms of the relative change from a normalising sample (f_n, Q_n, i.e. water or serum) such that

$$\Delta f = 1 - \frac{f_m}{f_n}, \tag{6.1}$$

and

$$\Delta\left(\frac{1}{Q}\right) = \frac{Q_n}{Q_m} - 1. \tag{6.2}$$

where f_m and Q_m are the measured sample. An example would be the measurement of serum proteins and electrolytes being calculated from the relative change from pure water so that the effects of temperature or resonator drift are normalised out.

The transportation distance of samples to the measurement system is up to 0.2 m long through microfluidic tubing. Subsequently local variations in Hgb concentration (RBC concentration) may arise owing to turbulence and surface friction. To ensure accurate Hgb values all samples are measured at three points along the sample distribution. The microfluidic system utilises a peristaltic pump, however, the build up of pressure between pump and sample can lead to residual flow when the pump is switched off. Consequently Poiseuille flow effects (see Serum separation) may occur that lead to additional uncertainties in the measurements. This is minimised by using low pump speeds and by conducting two measurements at each of the three measurement points to ensure no change in the resonant frequency or quality factor is observed. Values are given at the average of the six measurements with the error based on the standard deviation.

6.2.2 Serum separation

The accurate determination of Hgb concentration from the dielectric response of blood requires a comparative measurement of serum to remove the influence

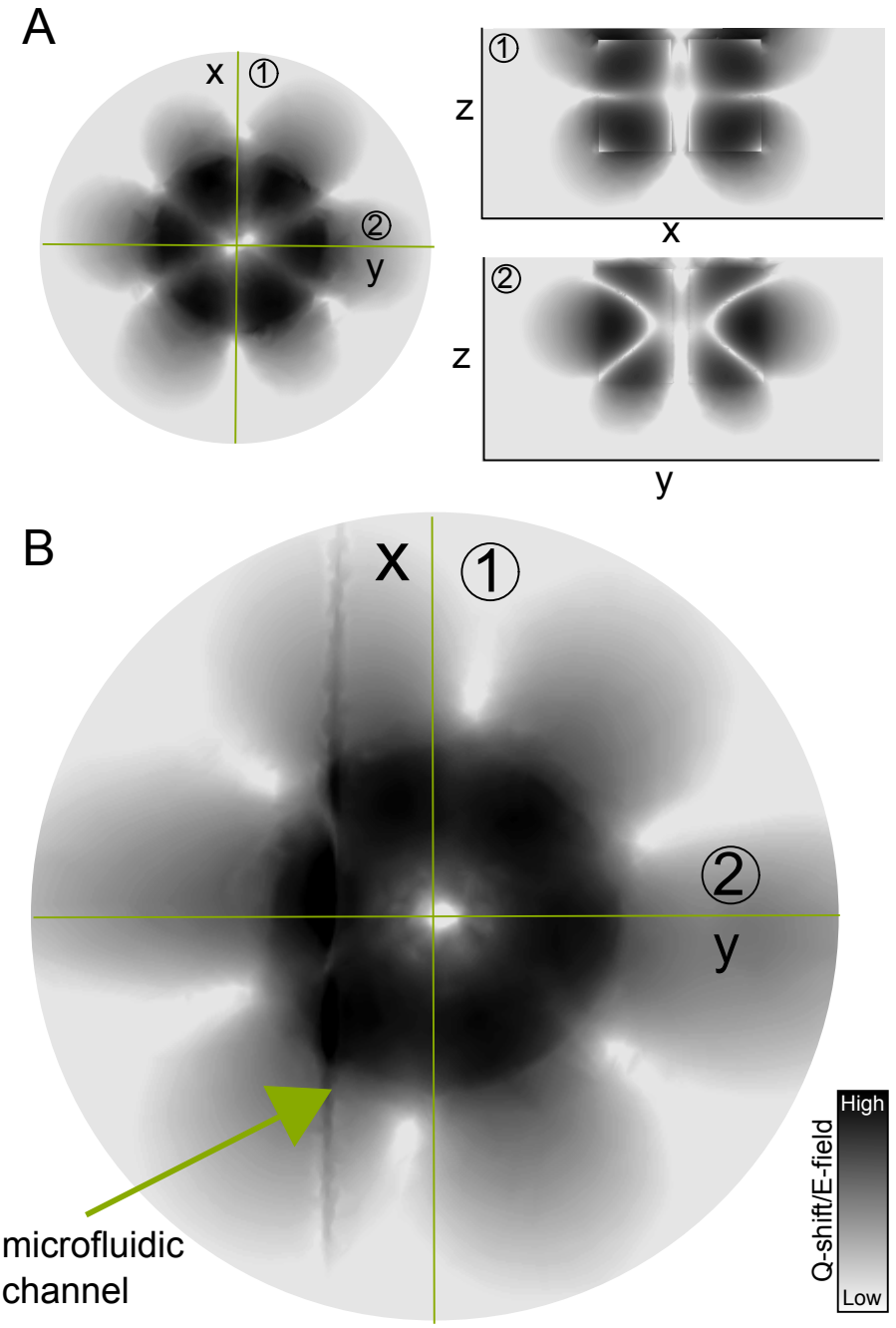


Figure 6.4: Modelled electric field distributions of the mode with (A) and without (B) water present in the microfluidic channel. The green lines labelled 1 and 2 are where the cross-section is taken in the vertical plane seen in (A).

of serum proteins and electrolytes. The comparative difference between whole blood and serum is therefore almost entirely dependent on Hgb concentration. To achieve separation of serum from blood in a fast and effective manner one of three methods can be used: filtering, centrifugation and techniques using hydrodynamic effects. The filtration of RBCs requires a consistent porous filter with dimensions smaller than those of RBCs at approximately 10×2 μm (oblate spheroids) and low levels of protein binding. Such filtration materials are available in abundance however in practice the red blood cells quickly block most of the filter resulting in reduced throughput. High pressures required to achieve serum separation and long separation time make filtration techniques poorly suited for on-chip analysis.

Centrifugation works on the principle of the centrifugal force acting on the RBCs is greater than that of serum. The result is the fractionation of blood into RBCs at the lowest level, platelets and white blood cells and serum at the highest level. Typical centrifugation on a centrifuge with a radius of approximately 0.1 m requires 5 minutes of centrifugation at 3000 rpm which from the point of view of point of care (POC) diagnostics is a long time. Subsequently a method has been demonstrated by Haeberle *et al* with serum separation achieved in 20 seconds [132]. Further centrifugation at high speeds can be utilised for the separation of serum proteins from serum.

Interesting flow dynamics can be established in the confined dimensions used in microfluidics to promote cell separation [133, 134]. The most promising method developed for cell/serum separation is based on Poiseuille flow. Poiseuille flow arises due to capillary or channel induced friction on the fluid nearest the walls thereby slowing the flow rate in the immediate vicinity. A radial distribution of the flow rate from the centre of the channel is observed that leads to solutes within the channel having a lift force away from the walls. The result is a concentrated distribution of inclusions at a radial position approximately 0.6 times the radius and few or no objects being present near the walls and a decrease in concentration at the centre of the channel [135] (Fig. 6.5). It has been found that by integrating sudden changes in channel dimensions Poiseuille flow can be encouraged thereby producing extended regions free of solutes. Used in serum separation from whole blood these regions of

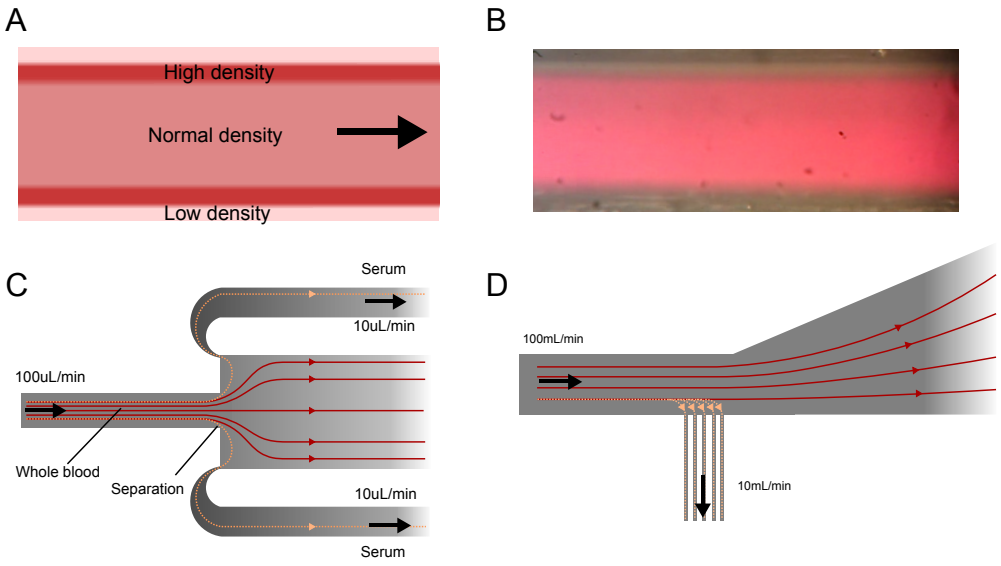


Figure 6.5: A serum-RBC separation technique based on Poiseuille flow in a channel (A,B). Sudden expansion of the channel creates a small volume that is devoid of RBCs (C,D).

low cell concentration can be siphoned off at a reduced flow rate to acquire pure serum. Experiments have shown promising results with almost 100 % serum purity achieved with diluted whole blood samples [134, 136] (Fig.6.5).

Sample separation for resonant measurements was conducted using centrifuging to ensure complete and accurate sample separation.

6.3 Haemoglobin, serum protein and electrolyte measurements

The primary purpose of the study regarding the described resonant technique was to determine the viability of the device in the determination of Hgb concentration of samples on the microlitre scale. The secondary purpose was to confirm the ability to conduct measurements on total electrolyte levels and serum protein concentration on similar sample volumes.

As outlined in Chapter 4 serum proteins are the principle organic contributor to the dielectric spectrum of serum. Measurements on serum protein concen-

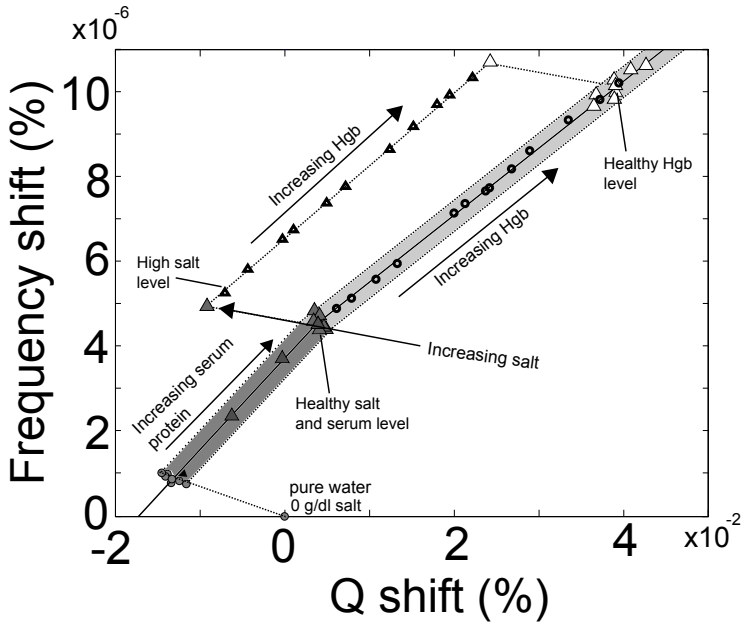


Figure 6.6: The change in resonant parameters Q and f as a function of of serum protein, Hgb and salt levels. The lower left hand part of the figure shows the trend of serum protein concentration in a salt solution as a function Q shift and frequency shift. The difference in the gradient of slope compared to Hgb concentration may arise because of albumin containing traces of salt. The middle to upper right data set is Q and f as a function Hgb concentration. The light grey box and dark grey box highlight the physiological range of salt in humans. The upper left data set is the same blood samples with elevated (x2) physiological salt levels. The gradient is maintained

tration were conducted by the variation of serum albumin protein concentration in a physiological saline solution which were compared to a reference of pure water. The resonant frequency and inverse Q shift demonstrated linear proportionality to serum protein concentration (Fig. 6.6).

A study into the impact of electrolyte levels on the resonant parameters revealed increases in the resonant frequency and decreases in Q-factor as a function of increasing ionic concentration. Further studies suggested that the electrolyte-induced shift in resonant parameters is independent of RBC count, serum protein concentration or existing electrolyte levels (Fig. 6.6). The effect of electrolyte levels can be differentiated from protein concentration variations owing to the opposite effects on the inverse shift of the Q factor with increasing resonant frequency (Fig. 6.7).

As proposed in chapter 4, to acquire an accurate Hgb measurement the measurement of a whole blood sample should be normalised against the values given by serum, thereby removing the influence of serum proteins and electrolytes. Measurements were undertaken on a range of human and murine samples to demonstrate that the outlined resonant technique provides the same trend regarding Hgb measurements for more than one mammalian species.

Initial measurements were conducted on 2 μL murine samples with Hgb values ranging from 0 to 17 g/dl with the purpose of ascertaining the resonant parameter dependence on Hgb concentration (Fig. 6.7). The EH_{603} mode of the dielectric resonator was excited with an operating Q-factor of 14,100 and resonant frequency of 9.4021 GHz with no sample present in the microfluidic channel. The measurement of 17 samples between 0 to 17 g/dl were made by the resonant technique and the resonant parameters found to be linearly dependent on Hgb concentration. Hgb measurements were made using a Sysmex F-820 system that is an optical technique based on the lysing of red blood cells. The resonant response was calibrated to the given Hgb measurements based on a best fit thereby enabling independent Hgb measurements to be made by the resonant method. Hgb measurements given by the resonant method are calculated from an average of the Q and resonant frequency Hgb values:

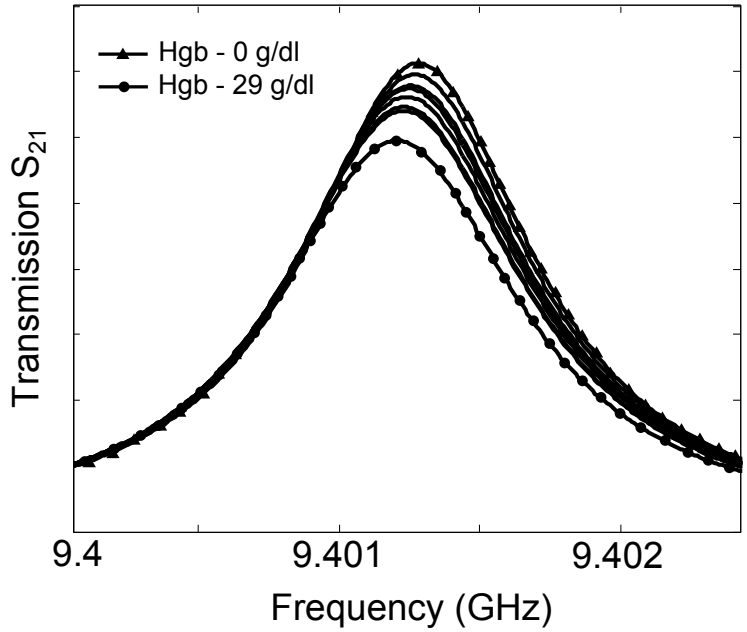


Figure 6.7: The transmission measurement (S_{21}) of the resonator with varied Hgb concentration.

$$\mathrm{Hgb_{res}} = \frac{\mathrm{Hgb}_Q + \mathrm{Hgb}_f}{2}. \tag{6.3}$$

A further 11 samples were obtained from healthy mice and the Hgb values calculated. Owing to the small sample sizes only three comparative measurements were made to the Sysmex system though each showed close agreement ($R^2 = 0.9758$, Fig. 6.8).

To ascertain that a linear dependence on Hgb concentration is still possible with an alternative field distribution (same EH_{603} mode, adjusted coupling) the resonator was changed to operate at an alternative Q-factor of 11,500 and resonant frequency of 9.4033 GHz with no sample present in the microfluidic channel. A greater range of Hgb concentrations were measured up to almost a RBC packing fraction of 1 (0-29 g/dl). A calibration curve was established using 14 samples and the resonant parameters confirmed to have a linear dependence on Hgb concentration (Fig. 6.9). Further to the calibration curve eight healthy donors were examined by the resonator and Sysmex methods to observe and compare resonator Hgb values. In addition to these mea-

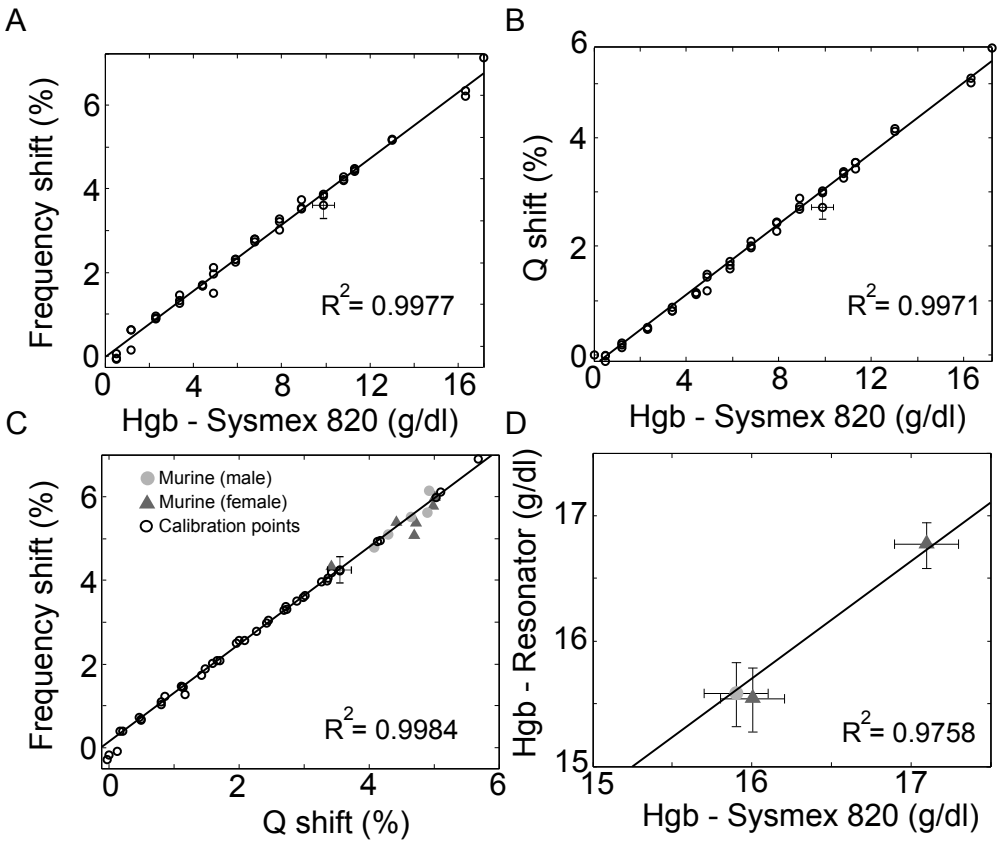


Figure 6.8: The response of the quality factor and resonant frequency as a function of murine Hgb concentration (A, B). Errors in the Sysmex system and in the resonant frequency and quality factor are based on the standard deviation of multiple measurements. Both the quality factor and resonant frequency exhibit linear dependence on Hgb concentration (C). Independent determination of Hgb values by the resonant method compared to Sysmex measured values (D).

surements the permittivity of the samples were compared to the Sysmex and resonator results. The resonator Hgb values were compared to the Sysmex results (Fig 6.9) and found to be in good agreement (R^2 = 0.9931-0.9988).

For comparative purposes calculations on the Hgb values using results normalised against water rather than serum were made. Our findings suggest that in healthy humans the correlation to Hgb concentration is of comparative accuracy to the serum normalised values (Fig 6.9D). As expected broadband spectroscopic measurements on the donor samples at 9.4 GHz showed trending with both the Sysmex system and resonator with samples of lower permittivity equating to higher Hgb values in healthy donors (Fig 6.10).

The high comparative accuracy to the Sysmex system demonstrates that the resonant method described is a viable technique for non-destructive and accurate (R^2 = 0.9931-0.9988, standard deviation 0.85 g/dL, against gold standard technique across 52 samples) determination of Hgb concentration in blood. Though serum separation was conducted outside of the microfluidic chip and the device implemented with a VNA, the discussed microfluidic separation techniques and a portable breadboard VNA would greatly increase the functionality of this technique with expected analysis times of the order of seconds.

6.4 APC murine measurements

Whilst sometimes ethically questionable, animals have long been an important component in monitoring, investigating and treating human diseases with many positive outcomes [137, 138]. Mammals commonly exhibit similar anatomical and physiological attributes that make them well suited to studying and modelling human conditions. Of all the animal models used approximately 95 % of biomedical investigations are conducted on murine models. The 99 % match between human DNA and mice make murine models useful for the determination of the role of genes in the human body [139]. They have also served as a means to develop models with genetic mutations than induce specific diseases similar to those present in humans.

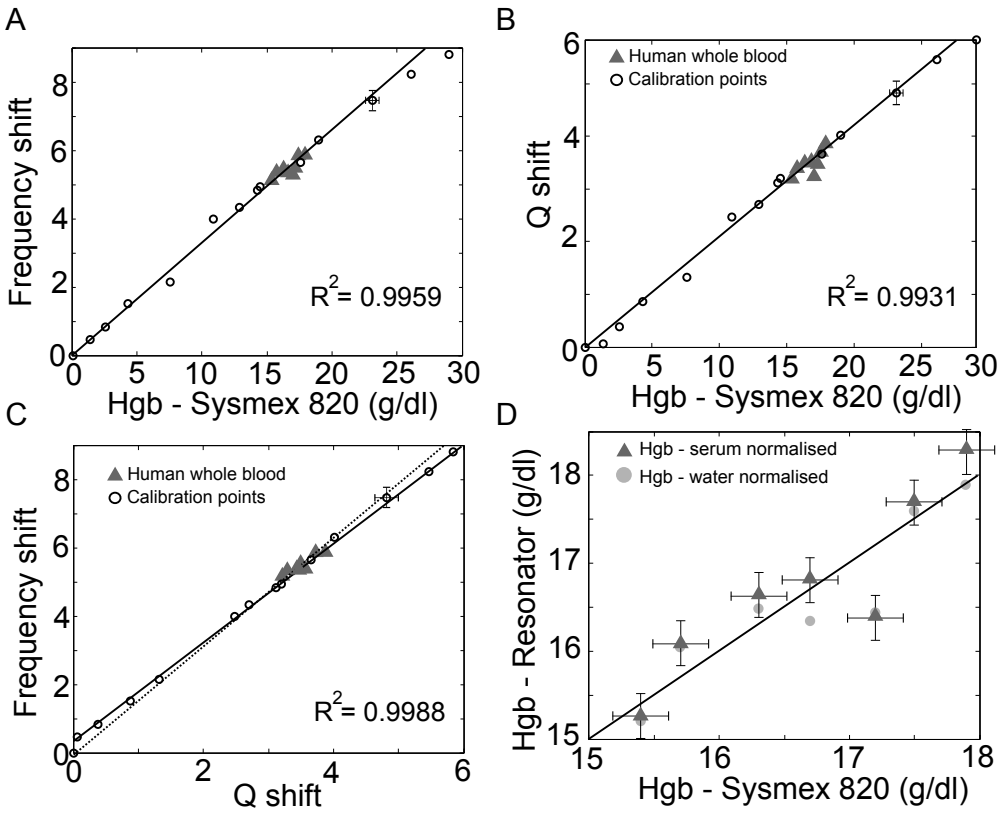


Figure 6.9: The response of the quality factor and resonant frequency as a function of human Hgb concentration (A, B). Errors in the Sysmex system and in the resonant frequency and quality factor are based on the standard deviation of multiple measurements. The quality factor and resonant frequency both show a linear dependence on Hgb concentration (C). Independent determination of Hgb concentration of 7 healthy patients by the resonant method compared to Sysmex measured values (D).

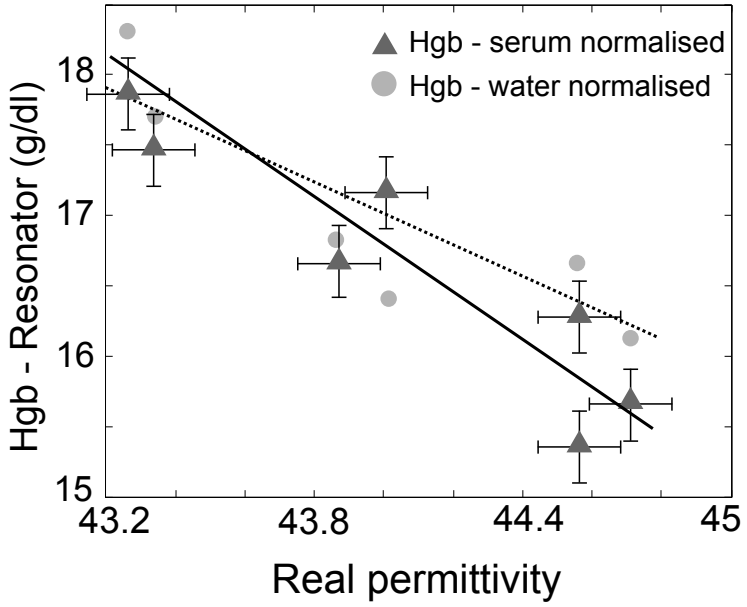


Figure 6.10: A comparison of Hgb concentration as determined by the resonant technique by normalising against both water and serum and compared to the permittivity.

6.4.1 Apc mice

The term Apc comes from the Adenomatous polyposis coli (APC) gene that is truncated or mutated in order to induce multiple intestinal neoplasia in mice [140, 141]. The APC model is a common experimental mouse for studying the progression of the colorectal cancer, the third most common cancer worldwide.

Colorectal cancer is often diagnosed as colon or rectal cancer though their genetic and progressive traits are the same (Fig. 6.11). A possible route to the formation of cancer is from the mutation of the APC gene caused by chromosomal instability that leads to the insufficient production of the APC protein used to prevent the build up of β-catenin. Within the cell lining (epithelial cells) of the colon or rectum an excess of β-catenin binds with the DNA within the nucleus causing uncontrolled activation of the cells replication [142]. The result is the formation of polyps (abnormal tissue growths) and although polyps may not necessarily become cancerous the chance of a mutant gene cell becoming cancerous is significant to the point that classification of a polyp is pre-malignant [142]. The growth of polyps can progress

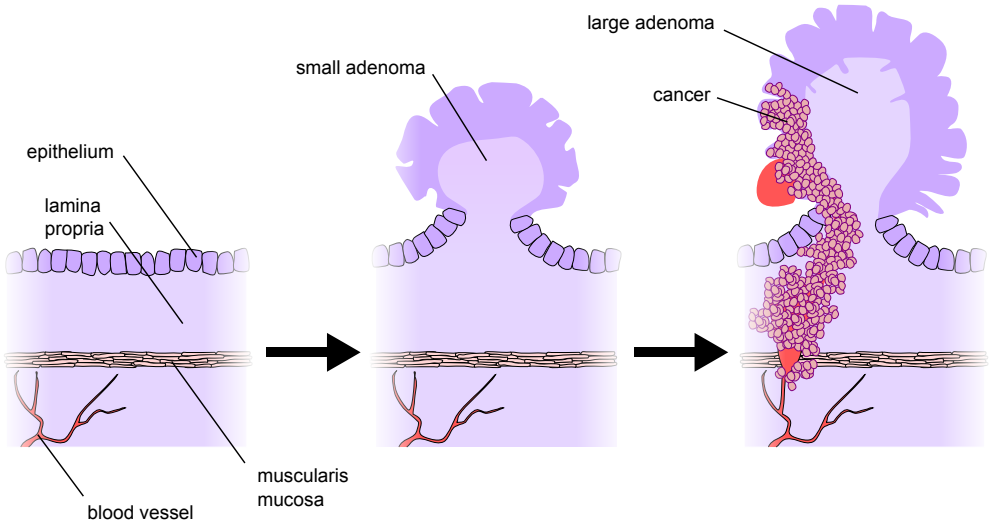


Figure 6.11: The growth of a polyp on the epithelial lining of the rectum or colon. Continual growth of a malignant polyp will likely rupture blood vessels which leads to bleeding into the colon or rectum.

through a number of stages, though the larger a polyp becomes the greater the risk of cancer. An additional and common adverse side effect of advanced polyps are the rupturing of blood vessels near the surface of the rectum or colon. Bleeding may be noticed in an individuals stool however it can often go unnoticed and untreated thereby resulting in continuous loss of blood and iron deficient anaemia [143].

The development of multiple neoplasia (30-100) in Apc mice [141] commonly leads to ruptures in blood vessels and mice with early stages of colorectal cancer will often exhibit signs of anaemia and at later stages severe anaemia [144].

Having demonstrated the viability of the resonant technique for Hgb measurements we undertook a study into the Hgb response of a selection of Apc mice from an $APC^{min/+}$ colony (eight mice) across an age range of 10 to 28 weeks and with an average age of survival of approximately 23 weeks. Hgb levels are indicative of the severity of the cancer due to the associated haemorrhaging in the colon or rectum [145]. Intermittent measurements of Hgb or haematocrit levels are therefore helpful in monitoring the progression of the disease. It is important when studying the response of a model not to induce addi-

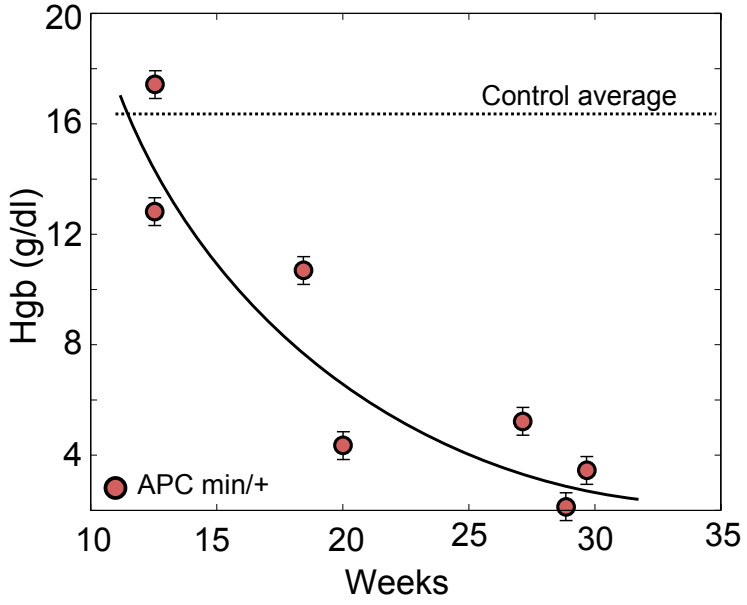


Figure 6.12: The Hgb values of Apc mice with respect to age. On average by 20 weeks a mouse will have acquired severe anaemia.

tional conditions. The excess removal of blood can induce additional stress on the mouse leading to possible outcomes such as anaemia (or exasperation of), change in disease development or an early death. Removal of more than 0.1 mL may be sufficient to induce such stress on a mouse therefore making minimally invasive measurements is advantageous by allowing for unimpeded development of the mouse and cancer.

The Hgb levels were determined for $APC^{min/+}$ mice and control mice ($APC^{+/+}$ - wild) with no mutated gene. Our findings showed significant decreases in $APC^{min/+}$ Hgb count with age when compared to a control (Fig. 6.12). The significance of the decrease was such that the average $APC^{min/+}$ mouse would be suffering from acute anaemia within 20-23 weeks from birth that equates with the average age of survival. The large decrease in Hgb levels is concurrent with expected trends [145].

6.5 Summary

A microwave resonant technique has been demonstrated as an accurate method for the determination of low volume samples. The determination of Hgb concentration in human and murine samples was calculated based on the comparison of the dielectric response of serum and whole blood. Additionally the ability to calculate serum protein levels and electrolyte concentration by resonant technique is outlined. The use of a dielectric resonator allowed for the measurement of sample volumes as low as 500 nL. The device was implemented for minimally invasive Hgb measurements on APC$^{min/+}$ murine models with multiple intestinal neoplasia. The results showed that with increased age the Hgb concentration of the mice was significantly reduced in agreement with previous reported findings [145]. The mice were observed to develop severe anaemia by the age of 20-23 weeks and that the decrease in Hgb levels after 10 weeks was in keeping with the progression of the neoplasia and health of the mice. This is the first non-optical technique developed for Hgb measurements and has advantages in its non-destructive acquisition of the data allowing for potential integration with other haematological measurements devices.

Chapter 7

Conclusion

7.1 Thesis review

The electromagnetic response of polar liquids, electrolytes and biological solutions at microwave frequencies have been investigated by broadband and resonant techniques. The fundamental physics behind the complex permittivity of liquids was explored in Chapter 2 and experimental microwave dielectric measurement techniques examined in Chapter 3. Broadband microwave studies into the dielectric response of polar liquids, in particular water were conducted, discussed and compared with respect to current literature throughout Chapter 4.

The ionic contribution to the imaginary permittivity was calculated by broadband measurements of sodium chloride solutions with respect to ionic concentration. A detailed analysis of the conductivity of group 1a metal chlorides as a function of temperature was reported on to confirm classical theories of conductivity. A product of this research was the development of a new method to determine the hydration radius of lithium and sodium as a function of temperature. As a method of differentiating ionic solutions, temperature dependence studies on conductivity proved ineffective. A study of more complex ionic solutes with high charge density ions in water revealed the presence of relaxation features that were explained in terms of ion association.

The dielectric response of protein solutions in water at frequencies between 500 MHz and 40 GHz was examined. Broadband dielectric analysis of biological liquids, namely water with ovalbumin, lactoglobulin, BSA or lysozyme, confirmed the presence of three protein concentration-dependent relaxation features. Based on current literature these were attributed to complex protein-water interactions (cross-correlation), hydration water and bulk water. Further to this the hydration and cross-correlation contributions to the complex permittivity were found to be dependent on the proteins present in solution. These findings were then utilised in the development of two methodologies for differentiating protein solutions at low and high concentrations. Lastly the dielectric response of blood at similar frequencies was examined and the importance of Hgb, serum proteins and electrolytes determined.

The dielectric haematological findings of Chapter 5 led to the development of a microwave dielectric resonator technique for the determination of Hgb concentration from sample volumes as low as 500 nL. The importance of Hgb levels in oxygen transport is explained in Chapter 6 as well as the adverse effects of a reduced level. The use of a resonant microwave device for Hgb measurements was demonstrated to be as accurate as many commercial techniques (SD = 0.85 g/dL, commercial comparisons to Sysmex devices >1.5 g/dL) and successfully implemented for the measurement of the Hgb response of mice with intestinal cancer over a range of ages. This is the first demonstration of a microwave device with haematological diagnostic value in addition to the first non-optical technique to determine Hgb concentration.

7.2 Main findings

7.2.1 Electrolyte differentiation and hydration shells

The microwave conductivity response was the focus of temperature dependent dielectric measurements on a range of electrolytes, specifically group 1a alkali metal chlorides. It was demonstrated that in addition to ionic radius hydration water at the surface of ions is highly important in the mobility of

the ions. Building upon known ionic radii it was possible to ascertain the temperature dependence of the effective radii of lithium and sodium. Additional studies revealed the spectral complexity of ionic solutes which do not fully dissociate in water. Partial dissociation is found to exhibit three discrete states of separation, visible in the dielectric spectrum. Deconvolution of the spectrum allowed for the calculation of the difference in molecular size of the partially dissociated ions.

7.2.2 Protein solution analysis

The high frequency (200 MHz to 40 GHz) complex permittivity of ovalbumin, lactoglobulin, BSA and lysozyme in water were analysed to examine the relaxation processes related to hydration water. Based on statistical analysis the deconvolution of the data confirmed the presence of three relaxation processes. Further to this finding the data suggested that the dielectric contribution from each of the relaxation processes was highly dependent on the protein solution under measurement.

Two methodologies for differentiating protein solutions have been developed. The former analysis technique based on low concentration protein solutions treated the system under measurement as having a single averaged response that is highly dependent on hydration water. Owing to the protein-dependent hydration number the method was able to differentiate protein solutions based on the dielectric contribution of hydrated water. Protein dependent ratios were established for four proteins; ovalbumin 0.17 ± 0.01, lactoglobulin 0.62 ± 0.03, BSA 0.51 ± 0.02 and lysozyme 0.77 ± 0.02.

The latter method used two frequencies at 200 MHz and 9 GHz to differentiate proteins. By comparing the high and low permittivities the hydration water and cross-correlation effects lead to a greater reduction in high frequency permittivity. The findings were less conclusive than the previous technique though differences in the ratio of permittivities between the proteins were observed. Protein ratios were established for ovalbumin 1.70 ± 0.08, lactoglobulin 1.96 ± 0.05, BSA 1.75 ± 0.11 and lysozyme 1.84 ± 0.21.

The high frequency dielectric spectrum of biological solutions has been shown to give rise to dielectric features relating to hydration water. These features have then been utilised to propose a unique means to differentiate protein solutions.

7.2.3 Hgb measurements

The permittivity of whole blood was examined and the dielectric contribution of individual constituents examined. Findings showed that serum proteins and electrolytes have the greatest organic solute contribution to the dielectric response of serum and Hgb the most substantial dielectric impact on whole blood. For the first time hydration water was seen to contribute to the dielectric spectrum of blood due to the presence of serum proteins and Hgb.

It was explicitly demonstrated for the first time that the dielectric influence of RBCs across microwave frequencies is almost entirely dependent on Hgb within the RBCs.

Building upon these findings a non-destructive and accurate method for the determination of Hgb concentration by comparison of the dielectric response of serum and whole blood was demonstrated. Using a high Q dielectric resonator healthy murine and human blood samples were measured and the resonant parameter response compared to Hgb levels measured on a Sysmex system. The findings demonstrate strong agreement between the resonant parameters and Hgb levels. The resonant device was calibrated and used to make independent minimally-invasive measurements on APC$^{min/+}$ mice with colorectal neoplasia. The results showed an average onset of severe anaemia as early as 20 weeks from birth in the mice measured, concurrent with expected trends. To the author's knowledge this is the first demonstration of a viable haematological technique using a microwave system.

7.3 Outlook

Having successfully proven dielectric measurement methods may be used in the determination of Hgb concentration on blood samples of less than a microlitre technical challenges now lie in the development of on-chip serum-RBC separation and integrating a breadboard VNA. Successful integration of these methods will result in a device with commercial viability.

As discussed in chapter 4 the MHz frequency response of blood is primarily governed by Looyenga polarisation which is a feature of cell membranes. The non-destructive nature of dielectric measurements at microwave frequencies may be complementary to low frequency measurements of RBC concentration demonstrated at MHz frequencies [107, 108, 110]. The ability to measure both HCT and Hgb values provides the means to calculate the mean cellular Hgb concentration, a vital measurement in the determination and differentiation of anaemias.

Further studies will be conducted on murine models with a range of chronic diseases that induce anaemias.

Bibliography

[1] Maxwell, J. C. *Philosophical Transactions of the Royal Society of London* **155**, 459–512 (1865).

[2] Zhu, X., Birringer, R., Herr, U., and Gleiter, H. *Physical Review B* **35**(17), 9085 (1987).

[3] Kinoshita, S. and Yoshioka, S. *ChemPhysChem* **6**(8), 1442–1459 (2005).

[4] Fitzgerald, A. J., Cole, B. E., and Taday, P. F. *Journal of pharmaceutical sciences* **94**(1), 177–183 (2004).

[5] DeGrado, T. R., Turkington, T. G., Williams, J. J., Stearns, C. W., Hoffman, J. M., Coleman, R. E., et al. *Journal of Nuclear Medicine* **35**(8), 1398 (1994).

[6] Crowfoot, D. *Nature* **135**, 591–592 (1935).

[7] Homola, J., Yee, S. S., and Gauglitz, G. *Sensors and Actuators B: Chemical* **54**(1), 3–15 (1999).

[8] Wang, J. *Electroanalysis* **17**(1), 7–14 (2005).

[9] Tesla, N. *Experiments with alternate currents of high potential and high frequency*. Book Tree, (2007).

[10] Marconi, G. *Nobel Lecture, December* **11** (1909).

[11] Skolnik, M. I. *Radar Handbook* (1962).

[12] Spencer, P. L. January 8 (1952). US Patent 2,582,174.

[13] Vrba, J. and Oppl, L. In *Microwave Techniques, 2008. COMITE 2008. 14th Conference on*, 1–4. IEEE, (2008).

[14] Klemm, M., Craddock, I., Leendertz, J., Preece, A., and Benjamin, R. In *Antennas and Propagation Society International Symposium, 2008. AP-S 2008. IEEE*, 1–4. IEEE, (2008).

[15] Roy, I. and Gupta, M. N. *CURRENT SCIENCE-BANGALORE-* **85**(12), 1685–1692 (2003).

[16] Cavaliere, R., Ciocatto, E. C., Giovanella, B. C., Heidelberger, C., Johnson, R. O., Margottini, M., Mondovi, B., Moricca, G., and Rossi-Fanelli, A. *Cancer* **20**(9), 1351–1381 (2006).

[17] Lantis II, J., Carr, K., Grabowy, R., Connolly, R., and Schwaitzberg, S. *Surgical endoscopy* **12**(2), 170–176 (1998).

[18] Korpan, N. N. and Saradeth, T. *The American journal of surgery* **170**(3), 271–276 (1995).

[19] EMISENS. *http://emisens.com/* .

[20] Griffiths, D. J. and College, R. *Introduction to electrodynamics*, volume 3. prentice Hall New Jersey, (1999).

[21] Stratton, J. A. *Electromagnetic theory*, volume 33. Wiley-IEEE Press, (2007).

[22] Clausius, R. *Armtheorie II* **62**.

[23] Mossotti, O. *Mem. Soc. Ital* **14**, 49 (1850).

[24] Debye, P. *Phisik. Zeits* **13**, 97–100 (1912).

[25] Onsager, L. *Journal of the American Chemical Society* **58**(8), 1486–1493 (1936).

[26] Kirkwood, J. G. *The Journal of Chemical Physics* **7**(10), 911–919 (1939).

[27] Litinskii, G. *Journal of structural chemistry* **39**(5), 687–693 (1998).

[28] Ben-Naim, A. *The Journal of Chemical Physics* **67**, 4884 (1977).

[29] Debye, P. J. W. *Polar molecules*, volume 172. Dover New York, (1929).

[30] Cole, K. S. and Cole, R. H. *The Journal of Chemical Physics* **9**, 341 (1941).

[31] Cole, K. S. and Cole, R. H. *The Journal of Chemical Physics* **10**, 98 (1942).

[32] Davidson, D. and Cole, R. *The Journal of Chemical Physics* **19**, 1484 (1951).

[33] Kirkwood, J. G. and Fuoss, R. M. *The Journal of Chemical Physics* **9**, 329 (1941).

[34] Fuoss, R. M. and Kirkwood, J. G. *Journal of the American Chemical Society* **63**(2), 385–394 (1941).

[35] Havriliak, S. and Negami, S. *Polymer* **8**, 161–210 (1967).

[36] Einstein, A. *Annalen der physik* **322**(8), 549–560 (2006).

[37] Edward, J. T. *Journal of Chemical Education* **47**(4), 261 (1970).

[38] Laidler, K. J. *Journal of Chemical Education* **61**(6), 494 (1984).

[39] Vanzura, E. J., Baker-Jarvis, J. R., Grosvenor, J. H., and Janezic, M. D. *Microwave Theory and Techniques, IEEE Transactions on* **42**(11), 2063–2070 (1994).

[40] Marsland, T. and Evans, S. In *Microwaves, Antennas and Propagation, IEE Proceedings H*, volume 134, 341–349. IET, (1987).

[41] Gregory, A. and Clarke, R. *Measurement Science and Technology* **18**(5), 1372 (2007).

[42] Guillon, P. In *Frequency Control Symposium, 1988., Proceedings of the 42nd Annual*, 259–262. IEEE, (1988).

[43] Cohn, S. B. *Microwave Theory and Techniques, IEEE Transactions on* **16**(4), 218–227 (1968).

[44] QWED. *Quick Wave (QWED) - www.qwed.com.pl* .

[45] Moura, F., Simoes, A., Stojanovic, B., Zaghete, M., Longo, E., and Varela, J. *Journal of Alloys and Compounds* **462**(1), 129–134 (2008).

[46] Von Hippel, A., Breckenridge, R. G., Chesley, F., and Tisza, L. *Industrial & Engineering Chemistry* **38**(11), 1097–1109 (1946).

[47] *Computer Simulation Technology (CST) Microwave Studio* .

[48] *Ansoft Corporation, HFSS* .

[49] Pozar, D. M. *Microwave engineering*. John Wiley & Sons, (2009).

[50] Kumar, A. and Singh, G. *Progress In Electromagnetics Research* **69**, 47–54 (2007).

[51] Horner, F., Taylor, T., Dunsmuir, R., Lamb, J., and Jackson, W. *Electrical Engineers-Part III: Radio and Communication Engineering, Journal of the Institution of* **93**(21), 53–68 (1946).

[52] Krupka, J., Geyer, R., Baker-Jarvis, J., and Ceremuga, J. In *Dielectric Materials, Measurements and Applications, Seventh International Conference on (Conf. Publ. No. 430)*, 21–24. IET, (1996).

[53] Baker-Jarvis, J., Geyer, R. G., Grosvenor Jr, J. H., Janezic, M. D., Jones, C. A., Riddle, B., Weil, C. M., and Krupka, J. *Dielectrics and Electrical Insulation, IEEE Transactions on* **5**(4), 571–577 (1998).

[54] Eric, F., Miller, R. C., and Goodwin, A. R. *Journal of Chemical & Engineering Data* **47**(1), 102–105 (2002).

[55] Shaforost, E., Klein, N., Vitusevich, S., Barannik, A., and Cherpak, N. *Applied Physics Letters* **94**(11), 112901–112901 (2009).

[56] Shaforost, E., Klein, N., Vitusevich, S., Offenhausser, A., and Barannik, A. *Journal of Applied Physics* **104**(7), 074111–074111 (2008).

[57] Barannik, A., Cherpak, N., Prokopenko, Y. V., Filipov, Y. F., Shaforost, E., and Shipilova, I. *Measurement Science and Technology* **18**(7), 2231 (2007).

[58] Krupka, J., Derzakowski, K., Riddle, B., and Baker-Jarvis, J. *Measurement Science and Technology* **9**(10), 1751 (1999).

[59] Johnson, S. G., Ibanescu, M., Skorobogatiy, M., Weisberg, O., Joannopoulos, J., and Fink, Y. *Physical Review E* **65**(6), 066611 (2002).

[60] Waldron, R. *Proceedings of the IEE-Part C: Monographs* **107**(12), 272–274 (1960).

[61] Carter, R. G. *Microwave Theory and Techniques, IEEE Transactions on* **49**(5), 918–923 (2001).

[62] Parkash, A., Vaid, J., and Mansingh, A. *Microwave Theory and Techniques, IEEE Transactions on* **27**(9), 791–795 (1979).

[63] Stockhausen, M. and Kessler, M. *Journal of Physics E: Scientific Instruments* **13**(7), 732 (2000).

[64] Auston, D. H. and Cheung, K. *JOSA B* **2**(4), 606–612 (1985).

[65] Ferguson, B. and Zhang, X.-C. *Nature materials* **1**(1), 26–33 (2002).

[66] Keutsch, F. and Saykally, R. *Proceedings of the National Academy of Sciences* **98**(19), 10533–10540 (2001).

[67] Head-Gordon, T. and Johnson, M. *Proceedings of the National Academy of Sciences* **103**(21), 7973–7977 (2006).

[68] Barthel, J., Bachhuber, K., Buchner, R., and Hetzenauer, H. *Chemical physics letters* **165**(4), 369–373 (1990).

[69] Barthel, J. and Buchner, R. *Pure and Applied Chemistry* **63**(10), 1473–1482 (1991).

[70] Burrell, K. *Am. J. Phys* **58**(2), 2 (1990).

[71] Agmon, N. *The Journal of Physical Chemistry* **100**(3), 1072–1080 (1996).

[72] Beneduci, A. *Journal of molecular liquids* **138**(1), 55–60 (2008).

[73] Zasetsky, A. Y. *Physical Review Letters* **107**(11), 117601 (2011).

[74] Gregory, A. and Clarke, R. *Tables of the complex permittivity of dielectric reference liquids at frequencies up to 5 GHz*. National Physical Laboratory, (2009).

[75] Kaatze, U. *Radiation Physics and Chemistry* **45**(4), 549–566 (1995).

[76] Agmon, N. *Chemical Physics Letters* **244**(5), 456–462 (1995).

[77] Buchner, R. *Pure and Applied Chemistry* **80**(6), 1239–1252 (2008).

[78] Kielland, J. *parameters* **4**(4), 4–5 (1937).

[79] Akilan, C., Hefter, G., Rohman, N., and Buchner, R. *The Journal of Physical Chemistry B* **110**(30), 14961–14970 (2006).

[80] Burgess, J. *Metal ions in solution*. Ellis Horwood Chichester, England, (1978).

[81] Lodish, H. F., Baltimore, D., Berk, A., and Darnell, J. E. *Molecular cell biology*. WH Freeman New York, NY:, (1995).

[82] Ruppin, R. *Optics communications* **182**(4), 273–279 (2000).

[83] Polder, D. and Van Santeen, J. *Physica* **12**(5), 257–271 (1946).

[84] Pecharroman, C. and Iglesias, J. *Physical Review B* **49**(11), 7137 (1994).

[85] Puranik, S. M., Kumbharkhane, A. C., and Mehrotra, S. C. *Journal of Molecular Liquids* **59**(2), 173–177 (1994).

[86] Schmeing, T., Huang, K., Kitchen, D., Strobel, S., and Steitz, T. *Molecular cell* **20**(3), 437–448 (2005).

[87] Paciaroni, A., Cinelli, S., Cornicchi, E., Francesco, A., and Onori, G. *Chemical physics letters* **410**(4), 400–403 (2005).

[88] Ebbinghaus, S., Kim, S., Heyden, M., Yu, X., Heugen, U., Gruebele, M., Leitner, D., and Havenith, M. *Proceedings of the National Academy of Sciences* **104**(52), 20749–20752 (2007).

[89] Svergun, D., Richard, S., Koch, M., Sayers, Z., Kuprin, S., and Zaccai, G. *Proceedings of the National Academy of Sciences* **95**(5), 2267–2272 (1998).

[90] Berendsen, H., Postma, J., Van Gunsteren, W., Hermans, J., et al. *Intermolecular forces* **11**(1), 331–342 (1981).

[91] Chakraborty, S., Sinha, S., and Bandyopadhyay, S. *The Journal of Physical Chemistry B* **111**(48), 13626–13631 (2007).

[92] Miura, N., Asaka, N., Shinyashiki, N., and Mashimo, S. *Biopolymers* **34**(3), 357–364 (2004).

[93] Wolf, M., Gulich, R., Lunkenheimer, P., and Loidl, A. *Biochimica et Biophysica Acta (BBA)-Proteins & Proteomics* (2012).

[94] Oleinikova, A., Sasisanker, P., and Weingärtner, H. *The Journal of Physical Chemistry B* **108**(24), 8467–8474 (2004).

[95] Cametti, C., Marchetti, S., Gambi, C., and Onori, G. *The Journal of Physical Chemistry B* **115**(21), 7144–7153 (2011).

[96] Nandi, N. and Bagchi, B. *The Journal of Physical Chemistry B* **101**(50), 10954–10961 (1997).

[97] Van-Quynh, A., Willson, S., and Bryant, R. *Biophysical journal* **84**(1), 558 (2003).

[98] Weingärtner, H., Nadolny, H., Oleinikova, A., and Ludwig, R. *The Journal of chemical physics* **120**, 11692 (2004).

[99] Hünenberger, P., Mark, A., Van Gunsteren, W., et al. *Journal of molecular biology* **252**(4), 492–504 (1995).

[100] Berman, H. M., Westbrook, J., Feng, Z., Gilliland, G., Bhat, T., Weissig, H., Shindyalov, I. N., and Bourne, P. E. *Nucleic acids research* **28**(1), 235–242 (2000).

[101] Basey-Fisher, T., Hanham, S., Andresen, H., Maier, S., Stevens, M., Alford, N., and Klein, N. *Applied Physics Letters* **99**(23), 233703–233703 (2011).

[102] Basey-Fisher, T. H., Hanham, S. M., Merelli, S. B., Maier, S. A., and Norbert, K. *IEEE Radio Wireless* **1** (2013).

[103] Asami, K., Hanai, T., and Koizumi, N. *Jpn. J. Appl. Phys* **19**, 359–365 (1980).

[104] Looyenga, H. *Physica* **31**(3), 401–406 (1965).

[105] Asami, K., Yonezawa, T., Wakamatsu, H., and Koyanagi, N. *Bioelectrochemistry and bioenergetics* **40**(2), 141–145 (1996).

[106] Bordi, F., Cametti, C., and Gili, T. *Journal of non-crystalline solids* **305**(1), 278–284 (2002).

[107] Beving, H., Eriksson, L., Davey, C., and Kell, D. *European biophysics journal* **23**(3), 207–215 (1994).

[108] Cha, K., Faris, R., Brown, E., and Wilmore, D. *Physiological measurement* **15**(2), 129 (1999).

[109] England, J., Walford, D., and Waters, D. *British journal of haematology* **23**(2), 247–256 (2008).

[110] Wolf, M., Gulich, R., Lunkenheimer, P., and Loidl, A. *Biochimica et Biophysica Acta (BBA)-General Subjects* **1810**(8), 727–740 (2011).

[111] Riggs, A. F. *Annual review of physiology* **50**(1), 181–204 (1988).

[112] Frank, B. *Physiological strategies for gas exchange and metabolism* **41**, 55 (1991).

[113] Perutz, M. *Science Is Not a Quiet Life: Unravelling the Atomic Mechanism of Haemoglobin* **4**, 287 (1997).

[114] Tremper, K. K. *CHEST Journal* **95**(4), 713–715 (1989).

[115] Cordone, L., Cupane, A., Leone, M., and Vitrano, E. *Biophysical chemistry* **24**(3), 259–275 (1986).

[116] Zijlstra, W., Buursma, A., and Meeuwsen-Van der Roest, W. *Clinical chemistry* **37**(9), 1633–1638 (1991).

[117] Cartwright, G. and Lee, G. *British journal of haematology* **21**(2), 147–152 (2008).

[118] McLean, E., Cogswell, M., Egli, I., Wojdyla, D., de Benoist, B., et al. *Public health nutrition* **12**(4), 444 (2009).

[119] Tyler, R. and Cowell, R. *Comparative Haematology International* **6**(1), 1–16 (1996).

[120] Pauling, L., Itano, H. A., Singer, S., and Wells, I. C. *Landmarks in Medical Genetics: Classic Papers with Commentaries* (51), 200 (2004).

[121] Dunne, J. R., Gannon, C. J., Osborn, T. M., Taylor, M. D., Malone, D. L., Napolitano, L. M., et al. *The American surgeon* **68**(6), 582 (2002).

[122] Stoltzfus, R. J., Mullany, L., and Black, R. E. *Comparative quantification of health risks: global and regional burden of disease attributable to selected major risk factors* **1**, 163–209 (2004).

[123] Stabler, S. P. and Allen, R. H. *Annu. Rev. Nutr.* **24**, 299–326 (2004).

[124] Herbert, V., ZALUSKY, R., DAVIDSON, C. S., et al. *Annals of internal medicine* **58**, 977 (1963).

[125] Brill, J. R., Baumgardner, D. J., et al. *American family physician* **62**(10), 2255 (2000).

[126] Fleming, M. D., Trenor, C. C., Su, M. A., Foernzler, D., Beier, D. R., Dietrich, W. F., and Andrews, N. C. *Nature genetics* **16**(4), 383–386 (1997).

[127] Lonappan, A. *Microwave and Optical Technology Letters* **54**(5), 1212–1215 (2012).

[128] Lonappan, A., Thomas, V., Bindu, G., Rajasekaran, C., and Mathew, K. *Journal of Electromagnetic Waves and Applications* **21**(8), 1131–1139 (2007).

[129] Gregory, A. P. *NPL Report MAT 58* (2013).

[130] Whitesides, G. M. *Nature* **442**(7101), 368–373 (2006).

[131] Anthony, J., Leonhardt, R., Argyros, A., and Large, M. C. *JOSA B* **28**(5), 1013–1018 (2011).

[132] Haeberle, S., Brenner, T., Zengerle, R., and Ducrée, J. *Lab on a Chip* **6**(6), 776–781 (2006).

[133] Hou, H. W., Bhagat, A. A. S., Lee, W. C., Huang, S., Han, J., and Lim, C. T. *Micromachines* **2**(3), 319–343 (2011).

[134] Sollier, E., Rostaing, H., Pouteau, P., Fouillet, Y., and Achard, J.-L. *Sensors and Actuators B: Chemical* **141**(2), 617–624 (2009).

[135] Schonberg, J. A. and Hinch, E. *J. Fluid mech* **203**, 517–524 (1989).

[136] Sollier, E., Cubizolles, M., Fouillet, Y., and Achard, J.-L. *Biomedical microdevices* **12**(3), 485–497 (2010).

[137] Le Bars, D., Gozariu, M., and Cadden, S. W. *Pharmacological Reviews* **53**(4), 597–652 (2001).

[138] Willner, P. *Psychopharmacology* **83**(1), 1–16 (1984).

[139] Bockamp, E., Maringer, M., Spangenberg, C., Fees, S., Fraser, S., Eshkind, L., Oesch, F., and Zabel, B. *Physiological Genomics* **11**(3), 115–132 (2002).

[140] McCart, A. E., Vickaryous, N. K., and Silver, A. *Pathology-Research and Practice* **204**(7), 479–490 (2008).

[141] Rakoff-Nahoum, S. and Medzhitov, R. *Science Signalling* **317**(5834), 124 (2007).

[142] Markowitz, S. D. and Bertagnolli, M. M. *New England Journal of Medicine* **361**(25), 2449–2460 (2009).

[143] Nalesnik, J. G., Mysliwiec, A. G., and Canby-Hagino, E. *Reviews in Urology* **6**(1), 1 (2004).

[144] Wang, J., Fernald, A. A., Anastasi, J., Le Beau, M. M., and Qian, Z. *Blood* **115**(17), 3481–3488 (2010).

[145] Lee, S. H., Hu, L.-L., Gonzalez-Navajas, J., Seo, G. S., Shen, C., Brick, J., Herdman, S., Varki, N., Corr, M., Lee, J., et al. *Nature medicine* **16**(6), 665–670 (2010).